Experimental Investigation of Cavity Flows

Tore Løland

August 25, 1998

Abstract

LDV, PIV and Laser Sheet flow Visualisation have been used to study flow inside three different cavity configurations. The results show that for sloping cavities the vortex structure inside the cavities depends upon the flow direction past the cavity. The shape of the downstream corner is a key factor in destroying the boundary layer flow entering the cavity. The present results show good agreement with numerical simulations of the same geometrical configurations.

The present investigation has been used to find the influence of the cavity flow on the accuracy of the ultrasonic flowmeter. A method to compensate for the cavity velocities has been suggested. The results show that the relative deviation caused by the cavity velocities has a linear dependency with the pipe flow.

It is clear from this investigation that the flow inside the cavities should not be neglected as done in the draft for the ISO technical report on ultrasonic flowmeters.

Acknowledgment

This study has been performed at the Department of Applied Mechanics, Thermo- and Fluid Dynamics at the Norwegian University of Science and Technology.

First I would like to thank my supervisor Associated Professor Dr.Ing. Lars R. Sætran for his guidance through this work.

Special thanks to Dr.Ing. Inge R. Gran and Robert Olsen for providing calculations for comparison.

I would also like to thank the laboratory staff John Krogstad, Arnt E. Kolstad and Øyvind Andersen, as well as my fellow colleagues Lars E. Torbergsen, Jan Dahlsveen, Bård Venås, Stein Rimestad, Ernst A. Meese and Dr.Ing. Jon H. Kaspersen for their help during this work and for helpful discussions.

I would like to thank Reidar Sakariassen at Statoil for initiating this project and for support and discussions about Ultrasonic Flow meters.

This work was financed through the co-operation project VNG-TUBAF-STATOIL-NTNU.

Finally, and most important I would like to thank my fiancée Astrid for her understanding and support through the hard times of this work. Without her help it would have been impossible to finish this thesis.

This thesis will be submitted for the degree:

Doktor Ingeniør (Dr.Ing.)

at the Norwegian University of Science and Technology.

Trondheim, August 25, 1998
Tore Løland

Contents

List of Figures

List of Tables

List of Symbols

Latin Letters

A^+	The constant used by van Driest
B	The constant in the log-law
C_0	Velocity of sound
C_f	Friction coefficient
C_P	Pressure coefficient
d,	Distance between the cavity openings
d_1,d_2	Intensity patterns
d_e	Diameter on the source density volume
D	Pipe diameter; Depth of cavity; Diameter of lenses
D_1,D_2	Fourier transform of the intensity patterns
Δt	Time between PIV pulses
$\Delta \vec{s}$	Distance traveled
ΔU^+	The wake strength
Δx	Distance traveled in x-direction
Δy	Distance traveled in y-direction
δt	Pulse length for PIV-systems
f	Focal length, Frequency of cavity oscillations
$f(x)$	Arbitrary continuous function
$F(u)$	Fourier transform of the arbitrary continuous function
G	Clauser shape parameter
H	von Karman shape parameter
i, j, k	Counter variables
i_1,i_2	Intensity functions
k	Turbulent kinetic energy
L_{def}	The deflection of the ultrapath
L_p	Ultrapath length
N	Number of exposures
N_l	Image density
N_s	Source density
P	Static pressure
Q	Volume flow in the water tunnel
$r(x, y)$	Correlation peak

Re_W	Reynolds number based on the cavity width
Re_x	Reynolds number from the plate start
Re_δ	Reynolds number based on the boundary layer thickness
RER	Relative error
$S(u)$	Fourier transform of the sampling function
SNR	Signal to noise ratio
$t_1.t_2$	Transit time for ultra pulse; Time for PIV pulses
T	Time for one ultra pulse
u'	Root mean square (rms) velocity on the x-direction
$uu.\ vv$	Normal stresses
$\overline{uv}$	Shear stress
u_τ	Friction velocity
U	Mean velocity on the x-direction
$\vec{U}$	Velocity vector
$U+$	Inner variable
$U_\infty.U_e$	Velocity outside the boundary layer
U_{ref}	The reference velocity over the contraction
U_s	The freestream velocity at the cavity front
U_δ	Velocity at the boundary layer end
v	Root mean square (rms) velocity on the y-direction
V	Mean velocity on the y-direction
$\overline{V}_{\text{AV}}$	Mean velocity found from the ultrasound flowmeter
$\overline{V}_A$	Correction velocity
$\overline{V}_{\text{bulk}}$	Bulk velocity in the pipe
$\overline{V}_B$	Correction velocity
w	Root mean square (rms) velocity on the z-direction
W	Width of a cavity; Mean velocity on the z-direction
W_i	Weighing factor for acoustic path no. i
x	Distance between the transducers in the x-direction
$x.y.z$	Cartesian co-oridantes
$\vec{x}_t$	Position at time t
$\vec{x}_{t+\Delta t}$	Position at time $t + \Delta t$
y^+	Inner variable
Y	Distance between the transducers in the Y-direction
z_0'	Focal distance
Z_0	Focal distance

Greek letters

β	Clauser equilibrium parameter, Angle between pipe flow and ultrapulse
Γ_t	Transport coefficient
δ	Boundary layer thickness
δ^*	Displacement thickness

∂	Partial derivative
ε	Dissipation
θ	Momentum thickness
θ_{start}	Start value for the theoretical momentum growth
θ_{ref}	The momentum thickness at the start of the cavity
κ	von K arman constant
λ	Wave length
μ_t	Turbulent dymanic viscosity
μ	Kinematic viscosity
ν	Viscosity
Π	Coles wake parameter
ρ	Density
$\overline{\rho}$	Mean density
τ_w	Wall shear stress

Superscript

$+$	Non-dimmensionalised with u_τ and μ
$-$	Time average

Subscript

i, j, k	General index
$1, 2, 3$	Cartesian coordinates
A	Cavity A
B	Cavity B
ref	Reference
start	Start value
∞,e	Outside the boundary layer

Chapter 1

Introduction

Norway has over the past decades become an important supplier of natural gas in the European market. Within year 2000 Norway will supply 20% of the European needs of natural gas. The Norwegian transport system for natural gas to the continental Europe is shown in Fig. 1.1. In 1995 Norway exported 30 billion standard cubic meters through these pipelines, and within year 2000 we will export export 60 billion standard cubic meters through our pipeline system. Close control with the gas volumes delivered is very important both for the buyer and the supplier of natural gas. An uncertainty of 0.5 - - 1 % in the measured volume passing through one of the metering stations represents an annual value of about USD 35 - - 70 million from year 2000, (see Bosio and Erdal 1996). It is to the benefit of the buyer and the seller of natural gas to control the uncertainty.

Focus has been set on gas metering as the requirements for high performance and reliability has increased. Different approaches have been used. Some of these include

- Improvement of the traditional technologies.
- The use of flow conditioners, FC (to make the system more compact and accurate, see e.g. Erdal 1997)
- Development of completely new technologies.

The traditional method for measuring large gas flow rates has up to date and will in the nearest future be the orifice plate. In an orifice plate the flow rate is a function of the pressure difference across the plate, the thermodynamic characteristics of the gas and the geometry of the orifice plate, see Fig. 1.2 for a description.

This method is described by an international standard, ISO-5167-1. Therefore it has been accepted as the basis for sales and allocation metering by the gas companies and the various national authorities, but the method has a few shortcomings: To cover a large flow rate range, more than one orifice plate is needed. A certain length of straight pipe is also needed

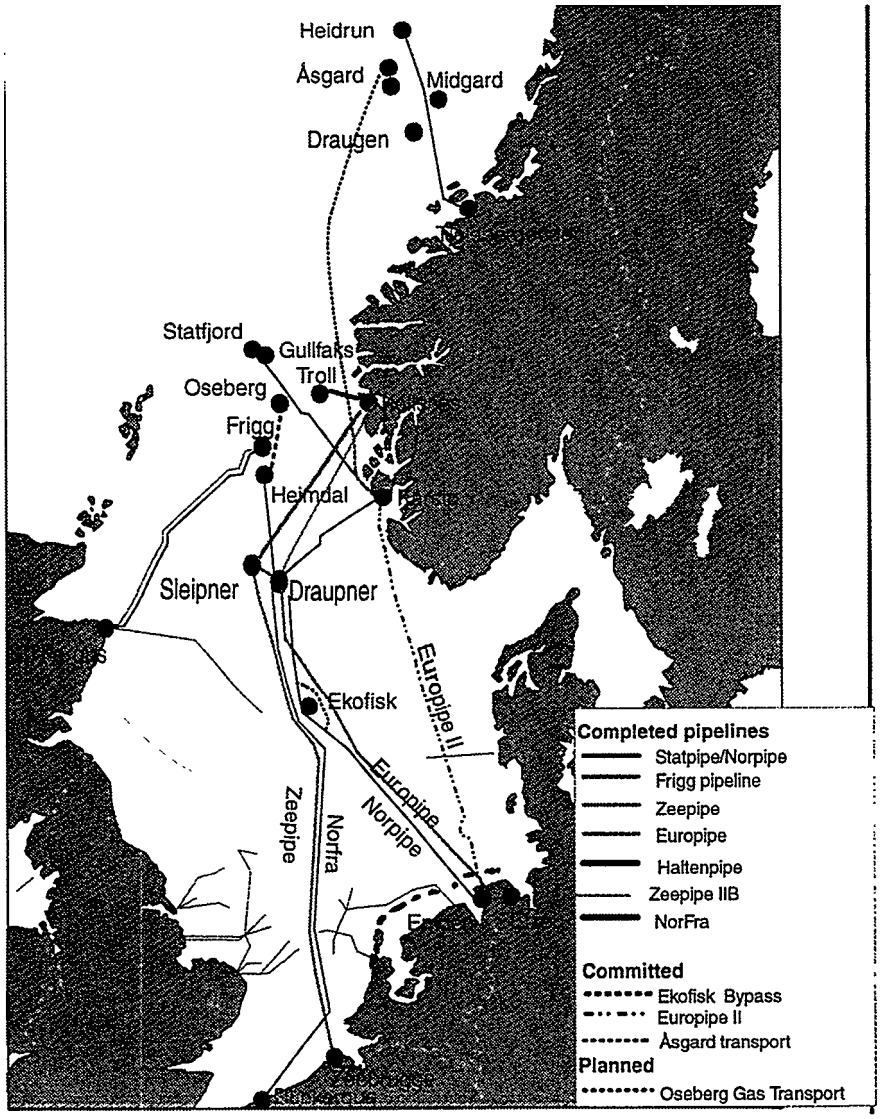

Figure 1.1: The STATOIL gas pipeline system

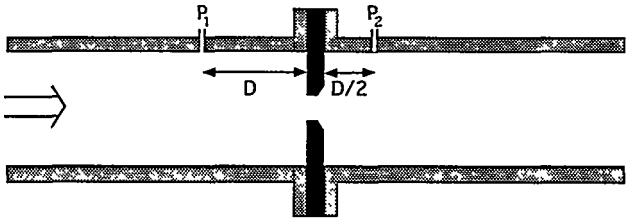

Figure 1.2: An orifice plate

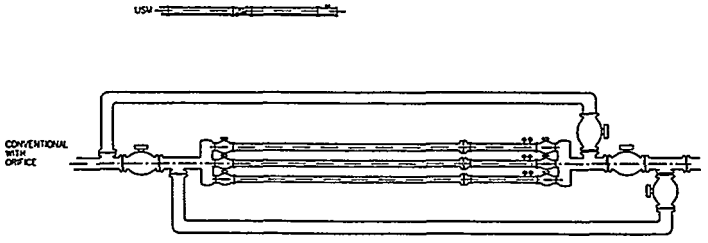

Figure 1.3: The benefits of the Ultrasonic flowmeter, adapted from Bosio and Erdal (1996)

to be certain that a fully developed pipe flow enters the orifice, as illustrated in Fig. 1.3. This means that a lot of space is needed and there will be limited flexibility with respect to capacity.

To overcome some of these disadvantages, new types of meters are now being used. The device attracting most interest today is the multi-path ultrasonic flowmeter. It has the advantage of having no moving parts, be less sensitive to flow disturbances, large range compared to a single orifice and it is also bidirectional. The main advantage seen from an offshore point of view is that the meter allow construction of compact metering stations.

Figure 1.3 illustrates one of the benefits of the ultrasonic flowmeter. It shows the size ratio between a bidirectional orifice meter station and the ultrasonic flowmeter with the same capacity and range. Statoil has 15 ultrasonic flowmeters installed offshore (1997), and within year 2000 the number of ultrasonic flowmeters will have increased to approximately 30 units. The size of the meters range from 6" to 30" in pipe diameter. They are used both in gas production and in monitoring of the gas transport in the different pipelines. It should be noticed that 12 ultrasonic flowmeters (1997) are installed on the Draupner platform, see Fig. 1.1.

In short terms, the working principle of an ultrasonic flowmeter is: A piezoelectric element is placed at the bottom of cavities as shown in Fig. 1.4. Each element can transmit and

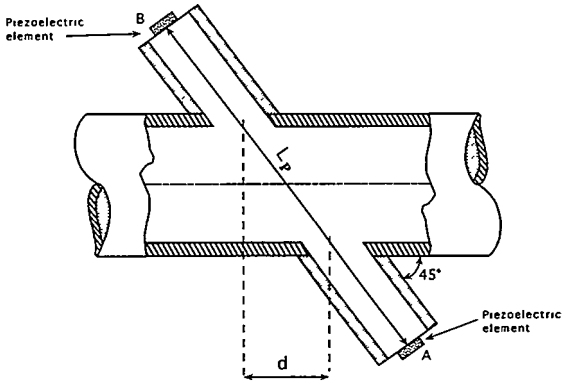

Figure 1.4: An ultrasonic flowmeter

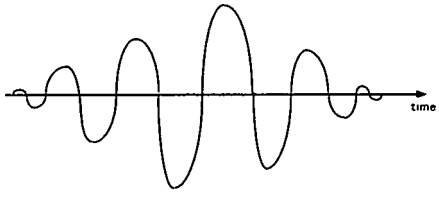

Figure 1.5: The ultrasound pulse

receive, giving ultrasonic paths as shown in Fig. 1.4. A multi-path ultrasonic flowmeter normally has four or five of these paths. Each pulse is an ultrasonic sound wave of normally 100 - 150 kHz with an increasing amplitude in the first part and a decreasing amplitude at the end. see Fig. 1.5.

Usually one pulse consists of 20 - 200 periods which gives a total time for one pulse of $T = 140$ - $2000\,\mu$s. When a pulse is received at B, the sensor switches and sends back the same pulse type to A, see Fig. 1.4. The time to find the mean flow rate is 1 - - 2 seconds. For each of the paths two transit times are found t_1 and t_2, were t_1 is the time from A to B and t_2 is the time from B to A. By using these times the velocity, $\overline{V}$, based on the measurements is given as

$$\overline{V} = \frac{L_p^2}{2d}\frac{t_1 - t_2}{t_2 t_1} \tag{1.1}$$

L_p and d are given in Fig. 1.4.

In a multi path ultrasonic flowmeter, the velocity is measured along four or five acoustic paths. An estimate of the mean axial fluid velocity in the pipe cross-section, $\overline{V}_{\mathrm{AV}}$, is calculated as

$$\overline{V}_{AV} = W_i \overline{V}_i \tag{1.2}$$

where W_i is the weighting factor for acoustic path number i and $\overline{V}_i$ is the average velocity measured along acoustic path i. The different W_i are set by the manufacturers of ultrasonic flowmeters. The weighting factor may be a fixed number different for each of the acoustic paths, or a more complex expression that depend on the ratio between the pipe flow from each of the acoustic paths. The ultrasonic flowmeter is a bidirectional flowmeter, and the direction of the flow is indicated by the sign of $(t_1 - t_2)$. If the flow direction is changed, $(t_1 - t_2)$ changes sign.

van Bloemendaal and van der Kam (1995) have shown that the ultrasonic flowmeter may be used after 90° and 180° bends if certain precautions are taken. They also showed that small step changes in the pipe diameter do not affect the ultrasonic flowmeter. Both Sakariassen (1996) and van Bloemendaal and van der Kam (1995) have reported misfunction in the ultrasonic flowmeter if it is placed near a pressure reduction valve that produce noise in the same frequency range as the ultrasonic pulse.

Another problem found, is that small meters (e.g. 6") have larger uncertainty in the pipe flow measurements than larger meters, like e.g. 20" meters. Sakariassen (1996) has shown that in some cases the relative error depends on the pipe flow, especially for small meters. This effect is illustrated in Fig. 1.6.

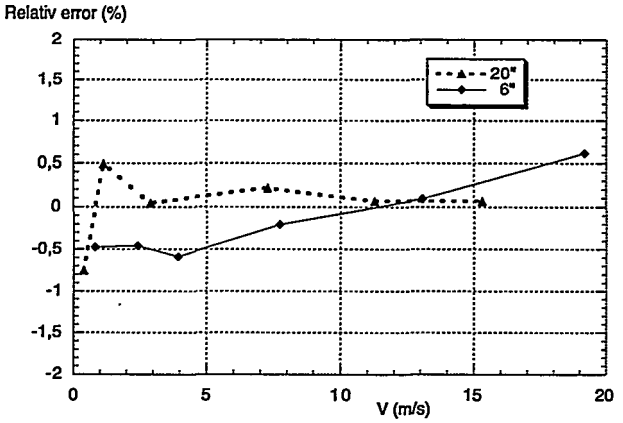

Figure 1.6: The calibration curves for a 6" and a 20" meter (Sakariassen 1996).

The difference in accuracy between the larger and the smaller size meter is the background for the present investigation. The cavity that is used to house the piezoelectric element is of the same size for both the 6" meter and the 20" meter. This means that the length

difference ,ΔL, for the two meter types is due to the difference in pipe diameter alone. The flow structure inside the cavity will influence more on the transit time for the 6" meter than for the 20" meter. The main purpose of this work is to investigate the flow structure inside cavities and use the results to calculate the cavity velocity influence on a thin ultra pulse traveling between the two ultrasonic sensors. The experimental work is done using Particle Image Velocimetry, PIV, Laser Doppler Velocimetry, LDV, and also Laser Sheet Flow Visualisation. The findings are compared to numerical simulations done by an inhouse CFD code called SPIDER (see Melaaen 1990) of the cavity flow.

This thesis includes a summary of some of the previous work reported on cavity flow. Also some theory for PIV is presented. Chapter 4 describes the experimental facilities used in this investigation. Chapter 5 and 6 deals with the results found. Chapter 7 is devoted to compare the results with numerical simulations, and also to estimate the influence of the cavity velocities on the pipe flow measurements. Finally a summary and conclusions are given.

Chapter 2

The physics of cavity flow

A cavity will change the drag and heat transfer, and may also cause intense periodic oscillations in the flow past the cavity. These intense periodic oscillations may lead to severe oscillations of the aero-dynamic structure, and may also cause noise. Typical areas where a cavity is present are in and around aircraft components and in slotted wall water and wind tunnels. The cavity flow effects are believed to have a significant influence on the fatigue life of nearby structures. Periodic oscillations in cavities have been observed over a wide range of Mach numbers, with both laminar and turbulent boundary layers entering the cavity and over a large range of width-to-depth ratios.

In general, cavity flow can be divided into two groups, open and closed or lid-driven cavities. In open cavities the flow separates at the upstream corner and reattaches near the downstream corner. In this type of flow there is the possibility of mass, momentum and heat transfer between the main flow and the flow inside the cavity, see Fig. 2.1 for a schematical description of an open cavity.

A lid driven cavity on the other hand has a closed area, with no exchange of mass with the "main flow". The vortices inside the cavity are driven by the fact that one of the walls

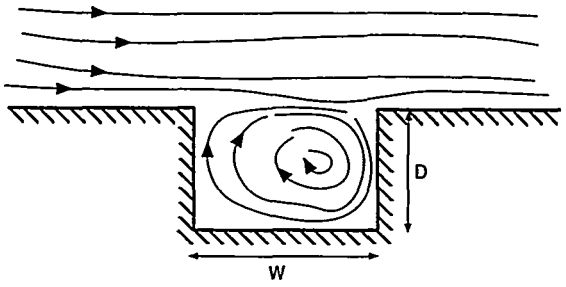

Figure 2.1: An open cavity

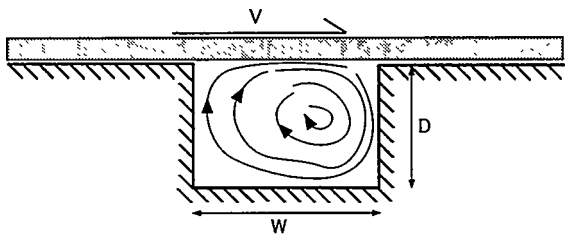

Figure 2.2: A closed or lid-driven cavity

are moving. see Fig. 2.2

Further. both open and closed cavities can be divided into deep and shallow cavities. For deep cavities $W/D < 1$ and for shallow cavities $W/D > 1$.

Rockwell and Naudascher (1978) characterized cavity oscillation flow into three groups.

- Fluid-dynamic oscillations, inherent instabilities in the flow causes these oscillations.
- Fluid resonant oscillations are oscillations influenced by resonant wave effects. standing waves.
- Fluid elastic effects, motions of a solid boundary are coupled with these oscillations.

All types can occur at the same time, but even then the oscillations can be separated from each other and categorized into the three different groups.

Many investigators have tried to reduce the oscillations by modifying the cavity geometry. The most important thing is the presence of the downstream corner. A common feature of many investigators is successful use of trailing edge ramps. Mass addition and removal process at the downstream corner of the cavity is an important factor of the feedback mechanism and thereby the oscillations. Any geometrical changes of the downstream corner which slows down this process, should decrease the oscillations. Franke and Carr (1975) among others have shown that for shallow cavities the amplitude of the oscillations is reduced by changing the cavity edges.

From a fundamental point of view the problem of the vortex mechanism itself is of even more interest. In most flow problems where separation is present, the vortex structure is unsteady, which make an experimental study difficult.

Koseff and Street (1984) did an experimental study of a lid-driven cavity. They found that the flow inside the cavity becomes turbulent at $Re_W = 6000$ to 8000. Visualisations showed that the downstream end wall appeared to cause significant motions in the perpendicular direction to the plane of main circulation. This seemed to influence the strength of the flow

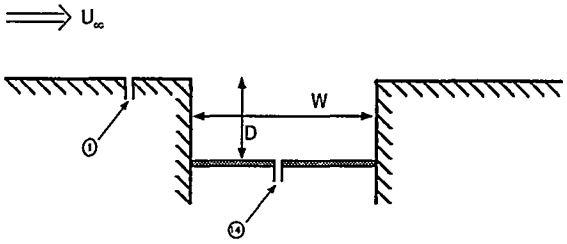

Figure 2.3: The cavity that Roshko measured on

in the plane of the main circulating flow. From their setup, they were able to observe Taylor-Görtler-like vortices inside the cavity. This indicated that there was a three-dimensional motion inside the cavity.

Roshko (1955) measured the wall pressure and did pitot measurements in a two-dimensional cavity placed in a wind tunnel. The depth of the cavity was varied. He found that there is a strong tendency to form a single vortex in a square cavity. He did point out that the pressure and forces due to the flow may be expected to depend on the state of the boundary layer. This means that the velocities in the cavity may depend on the shape of the boundary layer ahead of the cavity.

He also found that the friction forces on the cavity walls were small compared to the pressure forces. Even the friction forces on the free side of the vortex, were an order of magnitude smaller than the pressures. He was not able to measure it, but he concluded that there is a transport of fluid in and out of the cavity, because the friction force on the free side is too small to balance the pressure drag. This means that there must be a transport of momentum into the cavity, and that there is fluid flowing in and out of the cavity.

Roshko (1955) measured the static pressure at the bottom for different depths of the cavity, see Fig. 2.3 for description of the cavity.

A description of his results are shown in Fig. 2.4 where

$$C_p = \frac{P_{14} - P_1}{\frac{1}{2}\rho U_\infty^2} \tag{2.1}$$

He found that the pressure at the bottom did have an intermittent nature for two regions of D/W-relations, the first from 0.5 to 0.87 and a second one above 2. One of his most interesting findings is that the changes from intermittent to steady pressure happens at a distinct point $D/W = 0.87$.

His results indicated that a single steady vortex was first formed at $D/W = 0.87$. Other researchers have found for shallow cavities, i.e. Ethembabaoglu (1973), that the vortex has moved down to the downstream edge, leaving the place at the front more like a backward

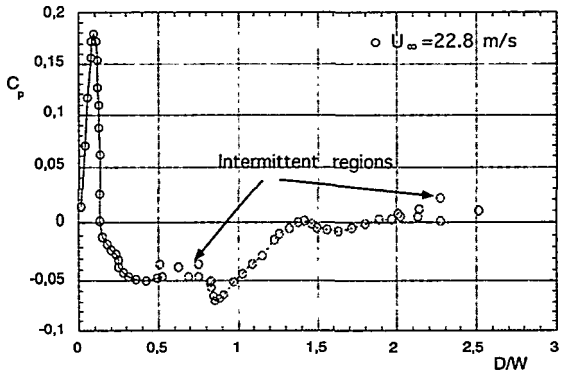

Figure 2.4: Results from Roshkos measurements

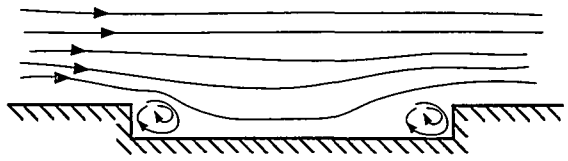

Figure 2.5: The flow structure for very small depths

facing step flow (see Fig. 2.5).

For shallow cavities Roshko found that there is a steep rise in pressure at the downstream end. His results indicated that the boundary layer separating at the front, diffused into the cavity. This means that the streamlines approaching the downstream edge are not the ones at the wall, but comes from further out in the main flow boundary layer. The pressure increases at first, as the depth is increased and consequently the stagnation pressure near the downstream edge increases at first. When the cavity depth exceeded a certain value, $D/W = 0.1$. the separated boundary layer no longer reattached at the bottom surface. He concluded that it was at $D/W = 0.1$ that a general vortex could be formed.

Roshko (1955) found from pressure measurements that for $D/W = 1.5$ the pressure distribution on the wall indicated a stationary vortex in the upper part of the cavity. The pressure distribution on the bottom of the cavity were different than for $D/W = 1.0$. By this he concluded that there has to be a small-scale structure in the lower part of the cavity with a single vortex in the upper part. Roshkos results for the shallowest cavities indicated that the flow structure were as illustrated on Fig. 2.5.

East (1966) did study oscillating flow in a deep rectangular cavity. The cavity was constructed to avoid mechanical resonance, and the depth of the cavity could be varied. It was placed in a 1.68 m×1.22 m closed return wind tunnel, with a maximum freestream velocity of 61 m/s. The cavity was mounted on a false floor in the wind tunnel. The flow entering

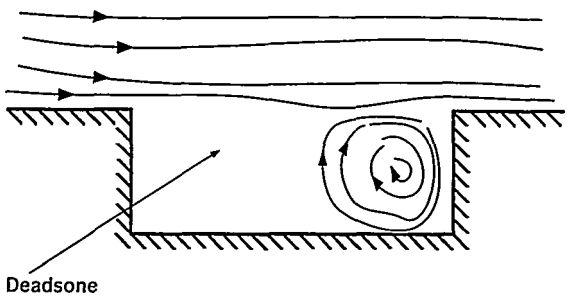

Figure 2.6: The deadsone in shallow cavities

the cavity was a low Mach number turbulent boundary layer flow. He stated that the overall features of the cavity oscillations can be characterized by W/δ, D/δ, the Reynolds number $Re = U_\infty \cdot \delta/\nu$ and the nondimesional frequency or Strouhal number $f \cdot W/U_\infty$.

By varying the depth he observed that the Strouhal number took values limited to two distinct intervals, one from 0.3 to 0.4 and the other from 0.6 to 0.9. Sarohia (1977) observed a similar behavior of the Strouhal number in his measurements of cavity flow.

Ethembabaoglu (1973) found that for $D/W \geq 0.667$ the vortex completely filled the cavity. But for smaller D/W-ratios, the vortex moved towards the downstream corner, forming what he did call a "dead flow region" at the upstream end of the cavity, see Fig. 2.6.

He found that the shape of the downstream vortex changed for ratios of D/W down to about 0.3. After this the shape of the vortex was unchanged.

He also discovered that the minimum pressure in the cavity is found at the cavity wall near the center of the vortex, independent of the depth. This agrees with the findings of Roshko (1955).

Wolley and Karamcheti (1973) assumed that the mechanism in cavities had to be the same as for two-dimensional parallel jets , and extended their theory for jets to cavities. Sarohia (1977) found that their theory did not work because it did not take into account the downstream corner. He found that this corner is the key factor to induce self-sustaining oscillations in the cavity shear layer. He also found from his measurements that the presence of a "backface" resulted in an integral relation between the wavelength of the propagating disturbance and cavity width.

From his work Sarohia (1977) concluded that one can divide cavity shear flow into the following main regions.

1. Close to the upstream corner, the flow is transformed from a boundary layer flow to a shear layer flow type. He found this to occur on a distance downstream from the upstream corner up to $10 - 15\ \theta$.

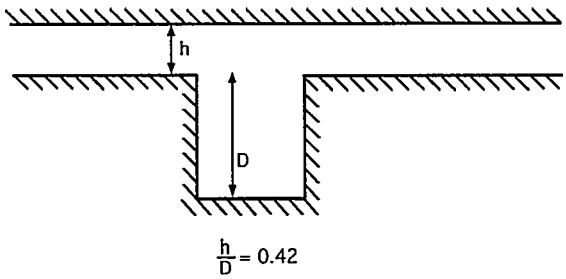

Figure 2.7: The dimensions of the cavity

2. The second region occupies the larger part of the cavity flow. In this region he found pure sinusoidal velocity oscillations

3. This region is very close to the downstream corner. Here the shear layer deflects in and out of the cavity at a constant frequency.

Rockwell and Knisely (1979) suggested, based on their results, that the oscillations are driven by a feedback mechanism. This feedback mechanism is an instantaneous propagation of pressure disturbances from the downstream corner towards the upstream corner. They investigated the oscillation feedback mechanism by examining the interaction of the shedding vortices with the downstream corner. Their results showed that the spectral content in the cavity flow could not be predicted using results from a backward facing step flow. The spectral organisation of the flow is increased by the downstream corner, and the turbulence intensity in the shear layer is decreased. They did use visualisations to show the time dependent interaction between vortices and the downstream corner. The visualisations did show how a vortex was formed in the shear layer, and how it proceeded towards the downstream corner. They did see three different types of interactions between a vortex and the downstream corner.

1. The vortex could escape, and continue downstream unaffected by the downstream corner.

2. The vortex was swept down into the cavity, known as "complete clipping".

3. The downstream corner did cut the vortex into two halves, one part continuing downstream. and the other part being swept into the cavity, known as "partial clipping"

By using simultaneous visualisations and pressure measurements, they did show that maximum fluctuating pressure was correlated with the most severe partial clipping.

O-Hern et al. (1994) studied a laminar cavity flow. The cavity geometry is shown in Fig. 2.7. The channel flow that drives the cavity circulation has small dimensions compared to the depth of the cavity. They used PIV, LDV and CFD in their study. The

center-plane velocity map from the CFD-results was in qualitative agreement with the experimental data, but there were differences in the position of the vortex center and the velocity magnitude.

Chapter 3

Theory of Particle Image Velocimetry

Particle Image Velocimetry, PIV, is a member of a broader class of velocity-measuring techniques. This technique measures the motion of small regions of fluid by observing the change in locations for the images of the particles at two or more times. These methods estimate the local velocity, $\vec{u}$, from

$$\vec{u} = \frac{\Delta\vec{s}(\vec{x}, t)}{\Delta t} \tag{3.1}$$

where $\Delta\vec{s}$ is the displacement of a particle, located at $\vec{x}$ at time t, over a short time interval, Δt, separating observation of particles images. Constant velocity is assumed over the displacement distance, $\Delta\vec{s}$, within the short time interval, Δt. The particles are usually solid particles in gases or liquids, but can also be gas bubbles in liquids or liquid droplets in gases.

3.1 Flow Illumination and Image recording

The PIV concept is to illuminate a field of small particles in a flow at different positions. The velocity is then found by calculating

$$\vec{U} \approx \frac{\vec{x}_{t+\Delta t} - \vec{x}_t}{\Delta t} \tag{3.2}$$

where $\vec{x}$ is the position vector of a particle, t is time in space, Δt is the time between the two light pulses and $\vec{U}$ is approximated local velocity.

Figure 3.1 gives the principle of how image storing is done.

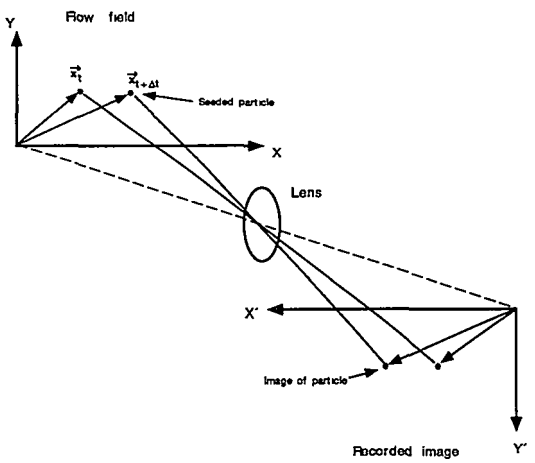

Figure 3.1: The principle of operation

3.1.1 Pulse coding

In practise the illumination of the flow and the recording of the image can be done in several ways. The one chosen depends on the different components in the designed system. There are several types of pulscodes that can be used.

- Single frame and double pulse, see Fig. 3.2. A single frame is illuminated with two light pulses separated by Δt in time.
- Single frame and multiple pulse, see Fig. 3.3. A single frame is illuminated with more that two light pulses separated by Δt in time. This will increase the signal to noise ratio, see Section 3.5.3.
- Multiple frame and single pulse, see Fig. 3.4. In this mode two frames with a single exposure on each is used to produce the velocity field.

In the single frame double/multiple exposure mode, several pulses are superimposed on the same frame (film or the charge coupled device, CCD). The total exposure of an image is the integral of all the exposures during the frame opening. Once the frame is exposed, the different component exposures can not be separated from each other. For processing of recorded images see Section 3.4.

The separation time, Δt, between the light pulses, is the single most important adjustable variable in a PIV system. The time δt, used to freeze the image is another time parameter,

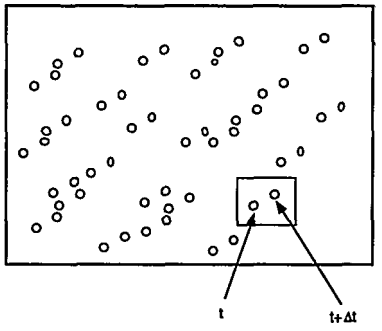

Figure 3.2: The pulse coding in single frame and double exposure

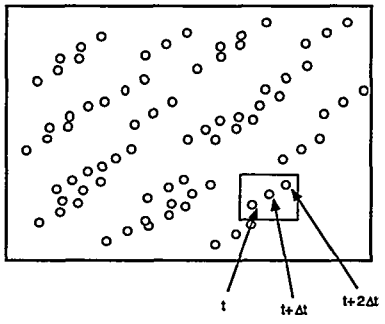

Figure 3.3: The pulse coding in single frame and multiple exposure

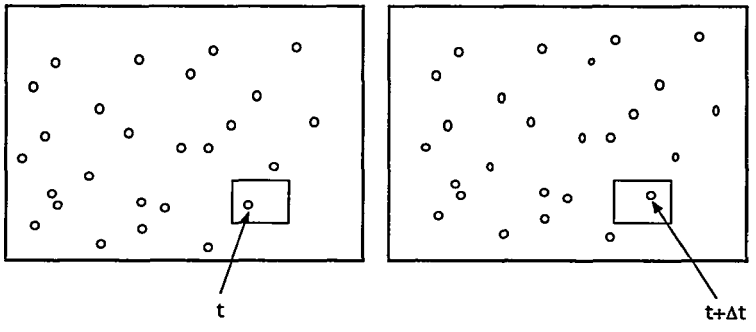

Figure 3.4: The pulse coding in multiple frame and single exposure

but not as important as Δt. An uncertainty in Δt will influence on the accuracy of the measured velocity. It becomes more and more important to keep δt small as the velocity increase. to ensure that the image is a genuine freeze of the particle position and not an integral in space.

There are several sources of light that can be used for pulsing.

- Ordinary light. chopped
- Xenon flash lamp
- Continuous lasers
- Ruby lasers
- Nd:Yag lasers. two single or one double

The recording media for storing the image is usually a photographic film or an array of photosensitive devices. CCD arrays. See Appendix A for a description of CCD arrays. Other recording media can be photorefractive crystals (Collicott and Hesselinh 1987), thermoplastic films or holographical plates (holograms) (Adrian 1991).

3.1.2 Optical parameters

Figure 3.5 describes two important parameters in the optical system, Z_0 and z_0'. In the figure the sheet of light in the flow field, the optical system and the image plane are shown. If we assume that the optical lens in Fig. 3.5 is an aberration-free thin circular lens with focal length f and diameter D, the geometrical lens law can be written as

$$\frac{1}{Z_0} + \frac{1}{z_0'} + \frac{1}{f} = 0 \tag{3.3}$$

and the image magnification is then defined as

$$M = \frac{z_0'}{Z_0} \tag{3.4}$$

The light sheet that illuminates the particles in the flow has a thickness ΔZ_0 and it comes from a coherent light source, usually a laser, with wavelength λ. The particles in the light sheet are in focus if the thickness of the sheet, ΔZ_0, is smaller than the object focal depth δZ (Adrian 1991). The object focal depth is given by

$$\delta Z = 4(1 + M^{-1})^2 \frac{f^2}{D^2} \lambda \tag{3.5}$$

where D is the diameter of the lens. Outside this range, δZ, the image is blurred by an amount. exceeding 20% of the infocus distance (Adrian 1991).

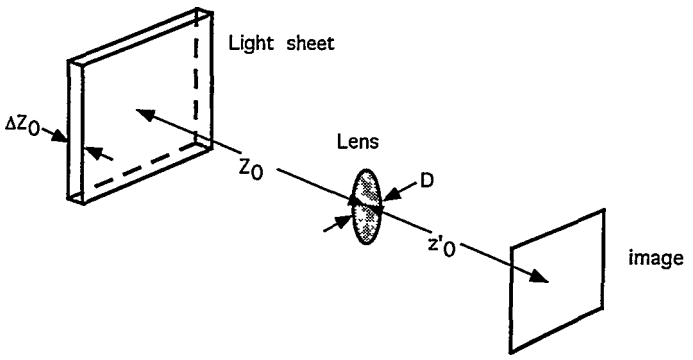

Figure 3.5: Schematic representation of the imaging set-up

3.1.3 Particle Image parameters

The diameter of the image of a particle in the flow field is given by

$$d_e = \sqrt{M^2 d_p^2 + d_s^2} \tag{3.6}$$

where d_p is the particle diameter and d_s is the point response function of the lens (Adrian 1991). If it is assumed that the lens is diffraction limited, the point response function can be written as

$$d_s = 2,44(M+1)\frac{f}{D}\lambda \tag{3.7}$$

(Adrian 1991).

When a lens is used to observe an area, it is important that the area can be brought close to the lens without changing the pattern. However the image of a distance point source, e.g. the image of a small particle, never forms a point. It is a Fraunhofer diffraction pattern even if a aberration-free lens is used (Hecht and Zajac 1974). For low exposures a circular pattern will be obtained, known as the Airy disk, shown in Fig. 3.6.

The figure from Hecht and Zajac (1974) (Fig. 3.6) shows an Airy pattern. The dark ring around the central disk is called the Airy disk. This dark ring corresponds to the first zero of the first order Bessel function, see Fig. 3.7. This Bessel function represents the impulse response of an aberration free lens, called the point spread function. x is the distance from centre. x_0 is defined as

$$x_0 = \frac{\lambda f(M+1)}{D} \tag{3.8}$$

(see Hecht and Zajac (1974) for more details).

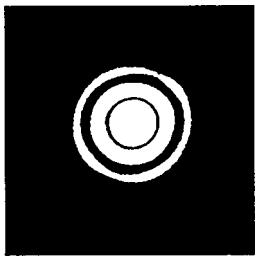

Figure 3.6: Airy pattern (Hecht and Zajac 1974).

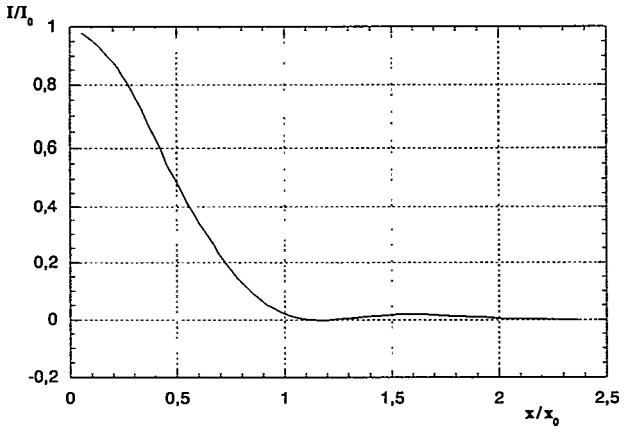

Figure 3.7: Intensity distribution of an Airy pattern

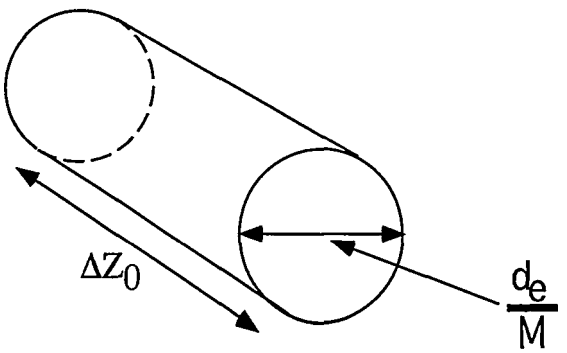

Figure 3.8: The volume that defines N_s

3.2 Number of tracer particles and image modes

There are two dimensionless numbers that describe the information in an image.

The *Source Density*, N_s, defined as the mean number of particles in a cylindrical volume formed by the intersection of the illumination sheet with a circle whose diameter d_e/M is that of the particle image projected back into the flow (Adrian 1991) (see Eq. 3.4 for definition of M). The number is given as

$$N_s = C\Delta Z_0 \frac{\pi d_e^2}{4M^2} \tag{3.9}$$

where C is the number of particles in an unit volume and ΔZ_0 is given in Fig. 3.5. The volume that describes N_s is given in Fig. 3.8. This number indicates if the image consists of individual particles, $N_s \ll 1$, or particle images overlap, $N_s \gg 1$.

In the same way as for the source density, it is possible to define a dimensionless number for the area that gives one velocity vector, the interrogation area. The *Image Density*, N_I is defined as the intersection of the light sheet with an area equal to the diameter of an interrogation spot projected back into the fluid (given for an $N \times N$-pixel interrogation area).

$$N_I = C\Delta Z_0 \frac{\Delta N^2}{M^2} \tag{3.10}$$

where ΔN is the number of pixels in an interrogation area, C is the number of particles in an unit volume and ΔZ_0 is given in Fig. 3.5. Figure 3.9 shows the volume that defines N_I.

These two numbers describe three different image modes

- Particle Tracking Velocimetry, $N_s \ll 1$, $N_I \ll 1$

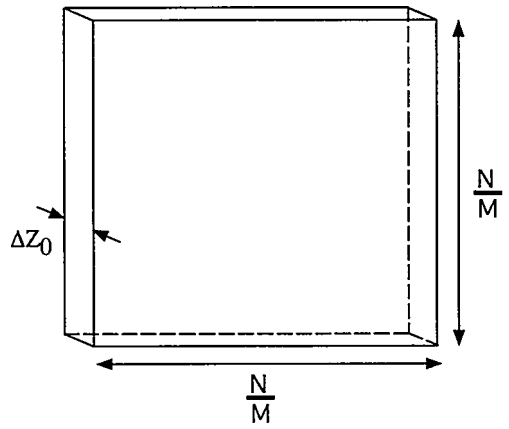

Figure 3.9: The volume that defines N_l

- Particle Image Velocimetry. $N_s \ll 1$, $N_l \gg 1$
- Laser Speckle Velocimetry, $N_s \gg 1$, $N_l \gg 1$

3.2.1 Particle Tracking Velocimetry, PTV

In this mode the concentration of particles is low, and we observe individual particles. The average distance between particles is much larger than the displacement between two exposures of the same particle. This means that it is fairly easy to identify particle image pairs. The problem with this method is that since the image density is low, it is not possible to determine the velocity in any arbitrary position. Only in positions where particle image pairs are present. In Fig. 3.10 a normal image for the PTV mode is given. As shown in the figure it is easy to distinguish between particle pairs.

3.2.2 Particle Image Velocimetry, PIV

PIV is the mode where the concentration of particle is increased enough such that $N_l \gg 1$, but still $N_s \ll 1$. This means that the number of particles in an interrogation area is increased to a level which makes it difficult to distinguish between image pairs, but isolated particles are still presented. Therefore statistical methods are used to measure the displacement of particle groups. In the PIV mode the image contains enough information to ensure that the velocity can be measured in any arbitrary position. This is shown in Fig. 3.11. As shown in the figure it is difficult to distinguish between the different particle pairs, but the average displacement in a small area of the image can easily be found.

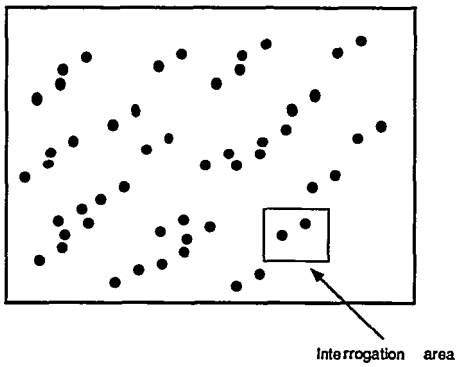

Figure 3.10: An example of what an image in PTV mode looks like

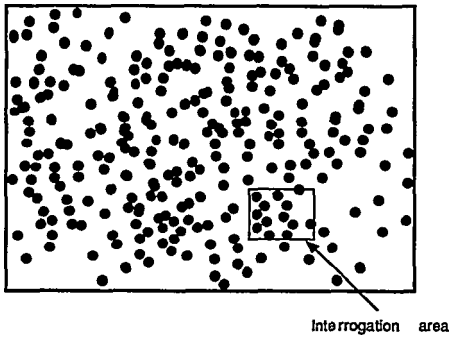

Figure 3.11: An example of what an image in PIV mode looks like

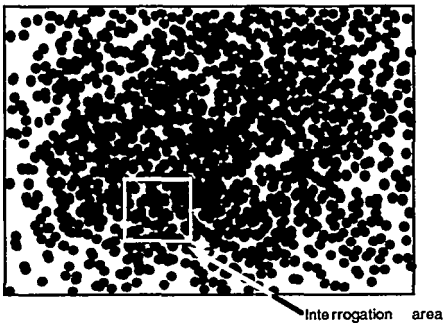

Figure 3.12: An example of what an image in LSV mode looks like

3.2.3 Laser Speckle Velocimetry, LSV

If the concentration of particles is further increased, it is no longer possible to distinguish between particles, see Fig. 3.12. Illumination of a flow with this concentration will give a random interference pattern. a speckle. By measuring the displacement of the speckle pattern the velocity in the flow can be determined. The problem with this method is that the high particle concentrations can give two-phase flow effects (Adrian 1984).

3.3 Digitizing Images and Bandwidth

To process a PIV image in a computer, it will have to be digitized. If a film camera is used. the digitalisation can be done by using a negative scanner. The resolution of a film negative is e.g. $320\,\mathrm{mm}^{-1}$.

When using a CCD camera, the digitalisation is done inside the camera. This means that the number of pixels in the camera gives the limitation of the resolution. The number of pixels for CCD cameras is normally 1000×1000 pixels. Capturing images is therefore a sampling process in two dimensions. It is best to look at the sampling process in one dimension first. Given a continuous function $f(x)$ (see Fig. 3.13) with its corresponding Fourier transform shown in Fig. 3.14.

This is a bandlimited function because the Fourier transform, $F(u)$, vanishes outside the frequency interval $[-W, W]$. This function $f(x)$ can be sampled with a sampling function $s(x)$. see Fig. 3.15 and Fig. 3.16. The sampled function $k(x) = s(x)\cdot f(x)$ is then given in Fig. 3.17.

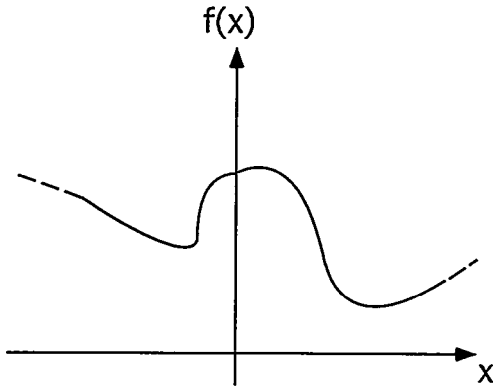

Figure 3.13: An arbitrary continuous function in space

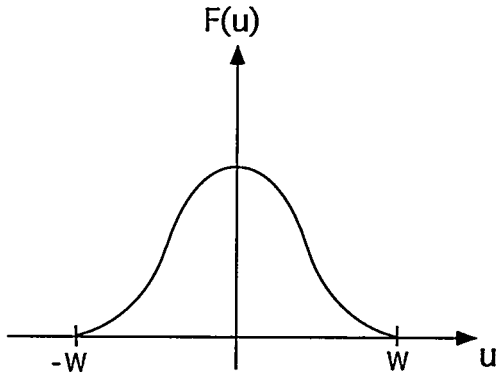

Figure 3.14: The Fourier transform of Fig. 3.13

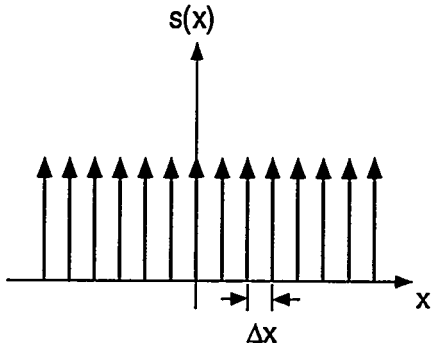

Figure 3.15: The sampling function

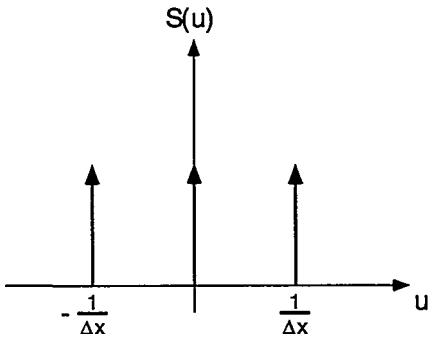

Figure 3.16: The Fourier transform of the sampling function

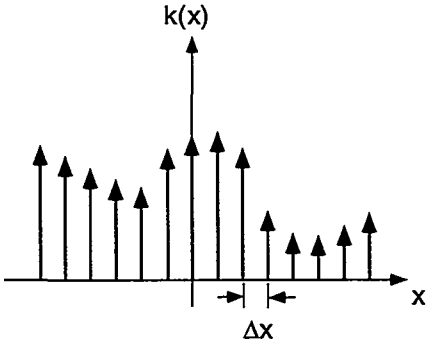

Figure 3.17: The sampled function $k(x) = s(x) \cdot f(x)$

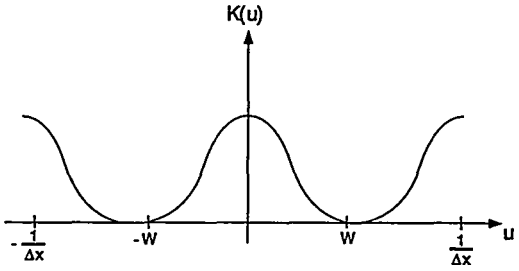

Figure 3.18: The Fourier transform of the sampled continuous function

The important point is to adjust the sampling function $s(x)$ sufficiently high, or Δx small enough. The sampled function $k(x)$ will then hold all the frequencies in the interval $[-W, W]$. To be able to fully recover the signal, the Nyquist criterium gives that a function $f(x)$ has to be sampled with at least two times the highest frequency in the signal.

$$\Delta x \leq \frac{1}{2W} \tag{3.11}$$

In this case the Fourier transform for $k(x)$ will be

$$K(U) = F(U) \otimes S(U) \quad \text{(convolution)} \tag{3.12}$$

and given in Fig. 3.18.

To fully recover the given band limited function $f(x)$, a window function $G(u)$ is introduced in the Fourier plane, see Fig. 3.19.

$$G(u) = \begin{cases} 1 & -W < u < W \\ 0 & \text{elsewhere} \end{cases} \tag{3.13}$$

This window function is used for full recovering of the function $f(x)$. In the Fourier plane $G(u)$ is multiplied with $K(u)$, which gives

$$G(u) \cdot K(u) = G(u) \cdot [F(u) \otimes S(u)] = F(u) \tag{3.14}$$

This is the same as the Fourier transform of $f(x)$, which means that the signal is fully recovered. Complete recovery of a bandlimited function from samples whose spacing satisfies the Nyquist criteria is known as the Whitaker-Shannon sampling theorem (Gonzalez and Woods 1992).

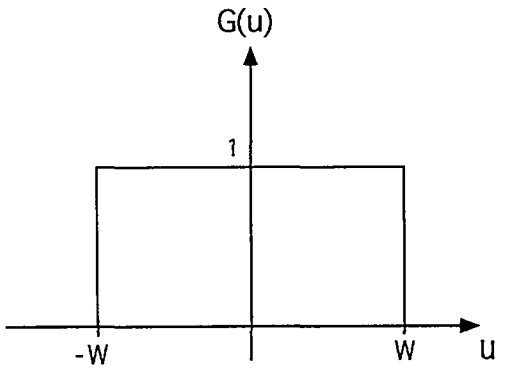

Figure 3.19: The Fourier window function

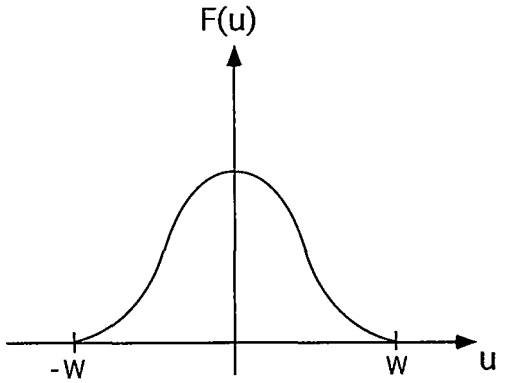

Figure 3.20: The Fourier transform of the sampled and recovered function

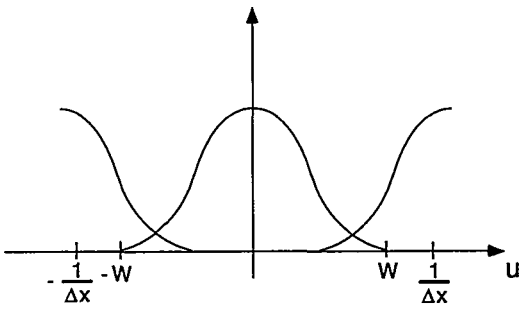

Figure 3.21: Sampling with aliasing

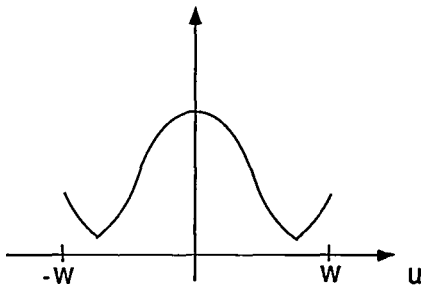

Figure 3.22: The recovered function from the sampled one

If the sample function used, $s(x)$, do not satisfy the Nyquist criterium, aliasing is introduced, and $K(u)$ will look like the pattern shown in Fig. 3.21

If the window function is introduced in the Fourier plane for $k(x)$ then

$$G(u)\cdot K(u) = G(u)\cdot[F(u)\otimes S(u)] \neq F(u) \tag{3.15}$$

An error is introduced at the bandwidth ends $-W$ and W (see Fig. 3.22), and the function $f(x)$ can only be recovered for the smaller space frequencies (greater distances).

In the two-dimensional case the sampling function $s(x,y)$ is given as in Fig. 3.23. The window function is given as

$$G(u) = \begin{cases} 1 & (u,v) \text{ inside the rectangle R} \\ 0 & \text{elsewhere} \end{cases} \tag{3.16}$$

No aliasing is introduced if

$$\frac{1}{\Delta x} > 2W_u \text{ and } \frac{1}{\Delta y} > 2W_v \tag{3.17}$$

The important factor in the digitalization process when using CCD cameras is therefore the bandwidth of the PIV image. The bandwidth gives the lower pixel resolution that we can use in a CCD camera. A band limited signal is given as

$$F(u,v) = 0 \text{ for } |u| > W_u \text{ and } |v| > W_v \tag{3.18}$$

in the 2-dimensional case, see Fig. 3.24.

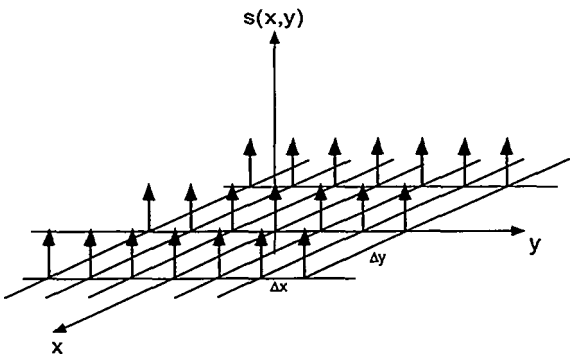

Figure 3.23: The sampling function in two dimensions

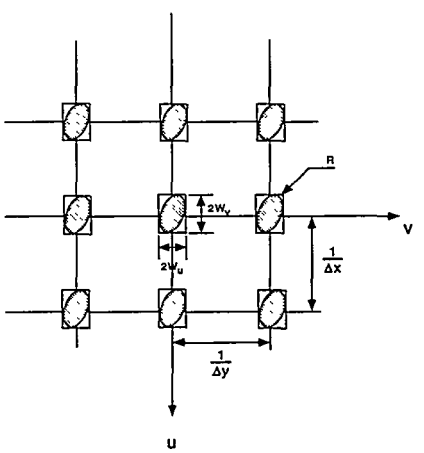

Figure 3.24: The Fourier transform of a sampled two dimensional band-limited function, adapted from Gonzalez and Woods (1992)

This means that the Fourier transform of a signal is zero outside a region given by W_u and W_v.

The bandwidth of $F(u,v)$ is given as W if we assume that x and y are equally spaced, and thereby u and v also will be equally spaced

$$W_u = W_v = W \tag{3.19}$$

A normal optical system for use in PIV is shown in Fig. 3.5. For this system the bandwidth is given as

$$W = \frac{D}{\lambda z_0} = \frac{D}{\lambda f(M+1)} \tag{3.20}$$

where z_0 is given in Fig. 3.5.

Westerweel (1993) gives an example of the optical bandwidth of a system like the one in Fig. 3.5. By choosing $f/D = 8$, $M = 1$ and $\lambda = 0.5\,\mu$m the bandwidth, W, is $125\,\text{mm}^{-1}$. The sampling rate will then have to be $2W = 250\,\text{mm}^{-1}$. The resolution of films given in the beginning of this chapter was $320\,\text{mm}^{-1}$, which is more than enough. For a normal CCD camera the resolution do not exceed $100\,\text{mm}^{-1}$. One important aspect is that $2W$ is the sampling rate needed to resolve the whole optical bandwidth and thereby reconstruct the image exactly. However in PIV there is no need to resolve the whole optical bandwidth to get fairly accurate results from interrogation analysis. In other words, there is no need to reconstruct the exact shape of each and every particle in the image; their position is enough. So instead of looking at the bandwidth of the optical system we should look at another parameter which is more fitting for the information stored in the image, namely the spectral density function of the random field that describe the statistics of a PIV image $R(u,v)$ (Westerweel 1993). If $R(u,v)$ is looked at as "nearly band limited" in the Fourier plane, it is a function that vanishes, but do not have to be zero:

$$R(u,v) \sim 0 \quad \text{for} \quad |u| > W_u \text{ and } |v| > W_v. \tag{3.21}$$

If a new bandwidth W_p is defined as the width of a cylinder which has the same volume as $R(u,v)$ ($\text{Volume}_{R(u,v)} = 1$) and has the same height as $R(0,0)$ (see Fig. 3.25), this gives

$$W_p = \sqrt{\frac{\frac{1}{\pi}}{R(0,0)}} \tag{3.22}$$

When W_p, which is the radius of a circular cylinder, is used on a square grid, W_p has to be related to the sampling on the square grid, see Fig. 3.26

The number in Fig. 3.26 represents the ratio of the side of the square compared to the diameter of the disk. In this case the area of the square and the circle are the same.

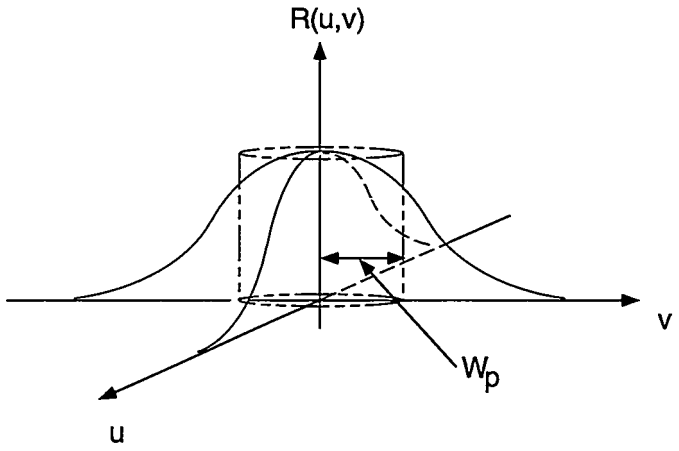

Figure 3.25: The bandwidth according to the definition of Parzen

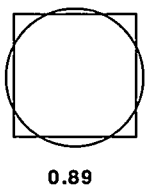

Figure 3.26: The relation of the bandwidth of a circular symmetric spectral density function to the sampling on a rectangular grid

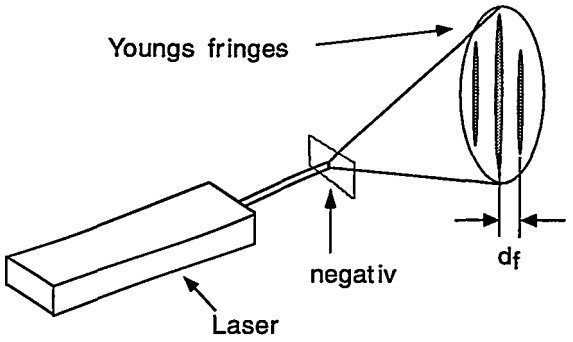

Figure 3.27: Optical Youngs fringes analysis

For the spectral density function of the random field that describe the statistics of a PIV image, $R(u, v)$, the height at origin is given as

$$R(0,0) \propto 4\pi\sigma_h^2 \tag{3.23}$$

where

$$\sigma_h = \frac{\lambda z_0}{D}\frac{\sqrt{2}}{\pi} \tag{3.24}$$

(Westerweel 1993). σ_h is the standard deviation for $R(u, v)$.

If $d_p \rightarrow 0$ is assumed, and the parameters are the same as for the calculations of the optical band width, $W_p = 76.5\,\mathrm{mm}^{-1}$. This shows that the CCD camera has enough spatial resolution for direct recording (Westerweel 1993).

3.4 Processing of a PIV-image

3.4.1 Optical methods

When PIV was introduced as a measuring technique, the computer capacity was not good enough for processing images digitally. Therefore the early PIV-analysis used optical methods. The most common was Youngs fringes, as shown in Fig. 3.27. In this method a small area of film was illuminated with a focused laser beam.

The film transparent was a multiple-exposure PIV-image (Vogt, Reichel, and Kompenhans 1994). The diffraction produced by the small coherent illuminated interrogation area of

the film generated the fringe pattern in the Fourier plane of a lens. In the optical correlation method it is assumed that the intensity pattern produced by a double exposure is represented by the function

$$d(x,y) = i_1(x,y) + i_2(x,y) \tag{3.25}$$

where i_1 and i_2 are the intensity patterns produced by the particles in the first and second exposure. In an interrogation area the intensity pattern produced by the two exposures are used to produce the velocity vector. If it is assumed that in the small interrogation area. the fluid motion is two-dimensional and uniform. all the particles in this small area have a corresponding particle. The average particle displacement in this area is given by

$$\Delta\vec{s} = (\Delta x, \Delta y) \tag{3.26}$$

As a consequence of this assumption the intensity of the second exposure may be looked at as

$$i_2(x,y) = i_1(x + \Delta x, y + \Delta y) \tag{3.27}$$

This gives the total intensity pattern

$$d(x,y) = i_1(x,y) + i_1(x + \Delta x, y + \Delta y) \tag{3.28}$$

If this is looked at as a sampling process (see Section 3.3), the total intensity may be written as

$$d(x,y) = i(x,y) \otimes [\delta(x,y) + \delta(x + \Delta x, y + \Delta y)] \tag{3.29}$$

where $\otimes$ is the convolution operator and $\delta(x,y)$ is the Dirac delta function at (x,y). The convolution integral is given as

$$f(\vec{x}) \otimes g(\vec{x}) = \int_{-\infty}^{\infty} f(\vec{u}) g(\vec{x} - \vec{u}) du \tag{3.30}$$

where $f(\vec{x})$ and $g(\vec{x})$ are arbitrary functions.

For the optical PIV-analysis, the total intensity recorded in an interrogation area will be given by the transmittance, τ, of the negative

$$\tau(x,y) = a + bd(x,y) \tag{3.31}$$

where a and b are photographic constants.

The laser and optical system (see Fig. 3.27) is used to produce the Fourier transform of $\tau(x,y)$

$$\hat{\tau}(u,v) = a\hat{\delta}(u,v) + b\hat{I}(u,v)[1 + e^{j2\pi\frac{u\Delta x + v\Delta y}{\lambda f_L}}] \tag{3.32}$$

where f_L is the focal length of the converging lens used (Lourenco 1996).

Today the computer capacity has improved, and the processing of PIV -images is done using computers. Four different approaches are used.

- Correlation methods (the most common)
- Fourier methods
- Statistical methods
- Neural networks

Since the correlation methods are the most commonly used, detailed description of this method will be given, while the three other methods will only be mentioned briefly.

3.4.2 Correlation methods

Correlation methods can be referred to as matching methods. The basic idea of the correlation methods is that a "cost"-function is set up, which is to be maximized or minimized. This "cost"-function measures the correlation or match between two regions in the interrogation area. It is maximum or minimum when $\Delta\vec{s}$ gives the best correlation. The correlation between two arbitrary continuous functions $f(x)$ and $g(x)$ is given by

$$f(x) \circ g(x) = \int_{-\infty}^{\infty} f^*(\alpha) g(x+\alpha) d\alpha \tag{3.33}$$

where $*$ denotes the complex conjugate (Gonzalez and Woods 1992). If $f(x)$ and $g(x)$ are the same function Eq. 3.33 becomes an auto correlation, and if $f(x)$ and $g(x)$ are different Eq. 3.33 is a cross correlation. Figure 3.28 gives an example of how the correlation is working. The correlation is computed by sliding $g(x)$ past $f(x)$ and integrate the product from $-\infty$ to ∞ for each value of displacement x. In Fig. 3.28 the dark area indicate where the product is non zero.

In the two dimensional and discrete case this is given by

$$f_d(x,y) \circ g_d(x,y) = \sum_{m=0}^{M-1} \sum_{n=0}^{N-1} f_d^*(m,n) g_d(x+m, x+n) \tag{3.34}$$

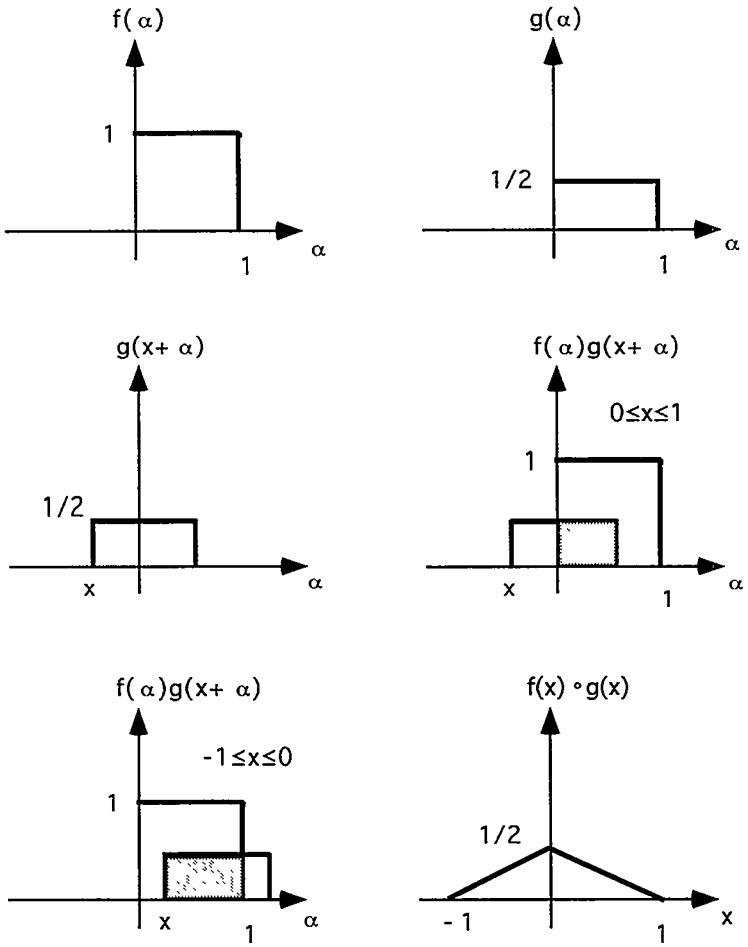

Figure 3.28: Graphical illustration of correlation, adapted from Gonzalez and Woods (1992)

where f_d and g_d are discrete functions of the arbitrary functions f and g respectively.

For the correlation of two functions the correlation theorem states both for continuous and discrete functions

$$f(x,y) \circ g(x,y) \leftrightarrow \hat{F}^*(u,v)\hat{G}(u,v) \tag{3.35}$$

(Gonzalez and Woods 1992). In practice this means that correlation in the spatial domain is the same as multiplication with the complex conjugate in the frequency domain. This is very useful when the correlation is to be implemented in a computer.

There are three types of correlations used in the PIV analysis. The type of correlation used, is a matter of hardware, e.g. what type of pulse and recording system used (see Section 3.1.1). These three types are

- Auto correlation
- Cross correlation
- Single frame cross correlation

Auto Correlation

If $f(\vec{x})$ and $g(\vec{x})$ are the same function the correlation is referred to as autocorrelation

$$\begin{aligned} f(\vec{x}) \circ f(\vec{x}) &= \int_{-\infty}^{\infty} f(\vec{s}) f(\vec{s}+\vec{x}) d\vec{s} \\ &= \int_{-\infty}^{\infty} f(\vec{s}) f(\vec{s}-\vec{x}) d\vec{s} \\ &= \int_{-\infty}^{\infty} \hat{F}(\vec{u}) \hat{F}^*(\vec{u}) e^{j2\pi\vec{x}\vec{u}} d\vec{u} \\ &= \int_{-\infty}^{\infty} |\hat{F}(\vec{u})|^2 e^{j2\pi\vec{x}\vec{u}} d\vec{u} \end{aligned} \tag{3.36}$$

where $\hat{F}(\vec{u})$ is the Fourier transform of $f(\vec{x})$. This equation gives the relation between the Fourier domain and the space domain.

The equivalence to the optical Fourier transform is the Fourier transform produced in the computer on the digital image. As for the optical case we have

$$d(x,y) = i(x,y) \otimes [\delta(x,y) + \delta(x+\Delta x, y+\Delta y)] \tag{3.37}$$

We know that convolution in space is the same as multiplication in frequency domain. The Fourier transform of the Dirac delta function is

$$\delta(x) \leftrightarrow 1 \tag{3.38}$$

and that shifting in space gives

$$f(x-\alpha) \leftrightarrow \hat{F}(u)e^{-j2\pi\alpha u} = |\hat{F}(\vec{u})|^2[\cos(2\pi\alpha u) - j\sin(2\pi\alpha u)] \tag{3.39}$$

(see e.g. Baher 1992).

This gives that

$$\hat{D}(u,v) = \hat{I}(u.v)(1 + e^{-j2\pi(u\Delta x + v\Delta y)}) \tag{3.40}$$

where $\hat{I}(u.v)$ is the Fourier transform of the intensity $i(x,y)$ produced by the particles in one exposure. The Youngs fringes, as found in the optical analysis can also be found from the computed Fourier transform. $|\hat{D}(u,v)|^2$ referred to as the powerspectrum, gives the Youngs fringes. see e.g Gonzalez and Woods (1992).

The periodicity and orientation of these fringes are given by the inverse Fourier transform of the powerspectrum.

$$\begin{aligned} h(x,y) &= \mathcal{F}^{-1}[|\hat{D}(u,v)|^2] \\ &= \int_{-\infty}^{\infty}\int_{-\infty}^{\infty} |\hat{D}(u,v)|^2 e^{-j2\pi(u\Delta x + v\Delta y)} du dv \\ &= 2\int_{-\infty}^{\infty}\int_{-\infty}^{\infty} |\hat{I}(u,v)|^2[1 + \cos(2\pi(u\Delta x + v\Delta y)e^{-j2\pi(ux+vy)} du dv \\ &= 2r(x,y) + r(x+\Delta x, y+\Delta y) + r(x-\Delta x, y-\Delta y) \end{aligned} \tag{3.41}$$

where $r(x,y) = \mathcal{F}^{-1}[|\hat{I}(u,v)|^2]$. This result is shown schematically in Fig. 3.29.

The self-correlation peak $r(x,y)$ has two symmetrical peaks on each side . The velocity (magnitude and angle) is found by locating of one of the peaks $r(x+\Delta x, y+\Delta y)$ or $r(x-\Delta x, y-\Delta y)$. The problem with the auto correlation is the directional ambiguity problem. The result is symmetric and might lead to a 180° error.

Cross Correlation

The cross correlation function is given by

$$h(\vec{x}) = f(\vec{x}) \circ g(\vec{x}) = \int_{-\infty}^{\infty} f(\vec{u}) f^*(\vec{u} + \vec{x}) d\vec{u} \tag{3.42}$$

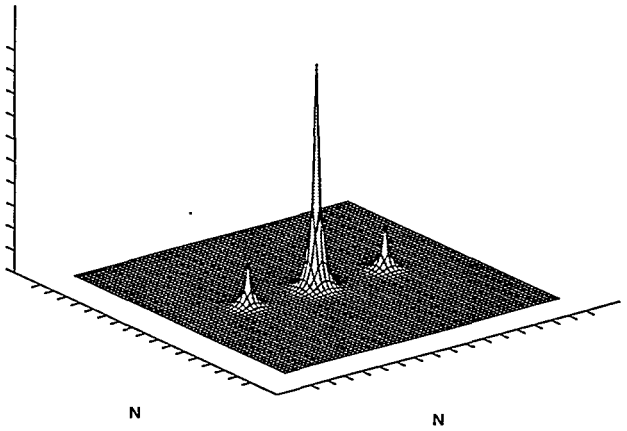

Figure 3.29: The result of the auto correlation shown schematically

(Gonzalez and Woods 1992). In the cross correlation function $h(\vec{x})$ is not a symmetric function which is the case for the auto correlation. This means that

$$f(\vec{x}) \circ g(\vec{x}) \neq g(\vec{x}) \circ f(\vec{x}) \tag{3.43}$$

As for the auto correlation, the multiplication is done in the Fourier plane.

The first exposure is on frame one and the second exposure is on frame two. This means that the exposures are separated. The transform of the first exposure is given as

$$\mathcal{F}[i(x,y) \otimes \delta(x,y)] = \hat{I}(u,v) \tag{3.44}$$

The transform of the second exposure is

$$\mathcal{F}[i(x,y) \otimes \delta(x+\Delta x, y+\Delta y)] = \hat{I}(u,v) e^{-j2\pi(u\Delta x + v\Delta y)} \tag{3.45}$$

The cross correlation $\hat{H}(u,v)$ is found by multiplying the first exposure with the complex conjugate of the second one (Gonzalez and Woods 1992).

$$\hat{H}(u,v) = |\hat{I}(u,v)|^2 e^{j2\pi(u\Delta x + v\Delta y)} \tag{3.46}$$

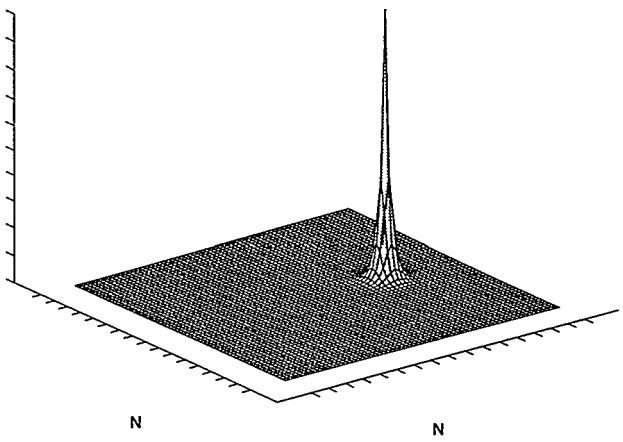

Figure 3.30: The result of the cross correlation shown schematically

In the space domain the cross correlation is given as

$$\begin{aligned} h(x,y) &= \mathcal{F}^{-1}[\hat{H}(u,v)] &&= \mathcal{F}^{-1}[|\hat{I}(u,v)|^2 e^{j2\pi(u\Delta x+v\Delta y)}] \\ &&&= \int_{-\infty}^{\infty}\int_{-\infty}^{\infty} |\hat{I}(u,v)|^2 e^{j2\pi(u\Delta x+v\Delta y)} e^{j2\pi(ux+vy)} du dv \\ &&&= \mathcal{F}^{-1}[|\hat{I}(u,v)|^2 \circ \delta(x+\Delta x, y+\Delta y)] \end{aligned} \tag{3.47}$$

Compared to the auto correlation this gives only one peak, with a much larger amplitude. This is schematically shown in Fig. 3.30.

The main advantages of the cross correlation method compared to the auto correlation method is that there is no directional ambiguity and better signal to noise ratio for the correlation peak.

Single Frame Cross Correlation

The cross correlation method need two single exposed frames to find the velocity vector. If the hardware of the PIV-system does not allow this, i.e. recording media is not fast enough, a double exposure single frame is the only solution. An alternative to the auto correlation is the single frame cross correlation. This approach is very useful when the amount of image shifting (see Section 3.5.1 for image shifting) is large compared to the interrogation area used. In the single frame cross correlation mode a cross correlation is

taken between two regions in the same image. If $\Delta\vec{s} = (\Delta x, \Delta y)$ is assumed to be the total displacement (including image shifting), the intensity pattern produced by a double exposure for the first region is given by

$$d_1(x,y) = i(x,y) \otimes [\delta(x,y) + \delta(x+\Delta x, y+\Delta y)] \tag{3.48}$$

with its Fourier transform

$$\hat{D}_1(u,v) = \hat{I}(u,v)[1 + e^{-j2\pi(u\Delta x + v\Delta y)}] \tag{3.49}$$

The intensity pattern produced by the two exposures on the second shifted region is given by

$$d_2(x,y) = i(x,y) \otimes [\delta(x - X_s, y - Y_s) + \delta(x + \Delta x - X_s, y + \Delta y - Y_s)] \tag{3.50}$$

with its Fourier transform

$$\hat{D}_2(u,v) = \hat{I}(u,v)[e^{j2\pi(uX_s + vY_s)} + e^{-j2\pi(u(\Delta x - X_s + v\Delta y - Y_s))}] \tag{3.51}$$

The correlation between these two regions is given by the product of the first exposure with the complex conjugate of the second one

$$\hat{D}_1(u,v)\hat{D}_2(u,v)^* \tag{3.52}$$

where $\hat{D}_2(u,v)^*$ is the complex conjugate of $\hat{D}_2(u,v)$.

$$\hat{D}_2(u,v)^* = \hat{I}(u,v)[e^{-j2\pi(uX_s + vY_s)} + e^{j2\pi(u(\Delta x - X_s) + v(\Delta y - Y_s))}] \tag{3.53}$$

The Fourier transform of the cross correlation is given as

$$\begin{aligned}
\hat{H}(u,v) \;= \hat{D}_1(u,v)\hat{D}_2(u,v)^* \;&= |\hat{I}(u,v)|^2[e^{-j2\pi(uX_s + vY_s)} + e^{j2\pi(u(\Delta x - X_s) + v(\Delta y - Y_s))} \\
&\quad + e^{-j2\pi(u\Delta x + v\Delta y + uX_s + vY_s)} \\
&\quad + e^{-j2\pi(u\Delta x + v\Delta y + u(X_s - \Delta x) + v(Y_s - \Delta y))}] \\
&= |\hat{I}(u,v)|^2[2e^{-j2\pi(uX_s + vY_s)} + e^{-2\pi(u(X_s - \Delta x) + v(Y_s - \Delta y))} \\
&\quad + e^{-2\pi(u(X_s + \Delta x) + v(Y_s + \Delta y))}]
\end{aligned} \tag{3.54}$$

This result is transformed back to the spatial domain

$$\begin{aligned}
h(x,y) &= \mathcal{F}^{-1}[\hat{D}_1(u,v)\hat{D}_2(u,v)^*] \\
&= 2r(x,y) + r(X_s - \Delta x, Y_s - \Delta y) \\
&\quad + r(X_s + \Delta x, Y_s + \Delta y)
\end{aligned} \tag{3.55}$$

where $r(x,y) = \mathcal{F}^{-1}[|\hat{I}(u,v)|^2]$.

The shape of the correlation peaks will depend on the amount of shift

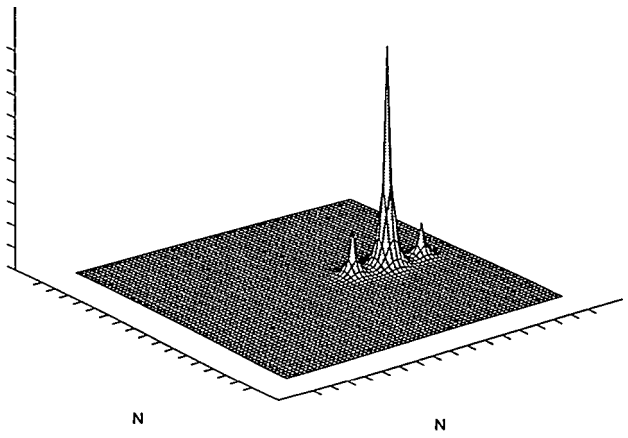

Figure 3.31: The result of the single frame correlation for image shift smaller than half the interrogation area

1. The shift is less than half the interrogation area. This will be similar to the auto correlation, except that the most intensive peak is not the self correlated one, but the cross correlation peak between the two regions. This is because the correlation area is not correlated with itself (see Fig. 3.31).

2. If the shift is more than half the interrogation area, but less than the total interrogation area length, the peak will be similar to case one, but one of the peaks is missing. The one furthest away form the self-correlation will not be present, see Fig. 3.32.

3. If the shift is more than one interrogation area length, the peak will look like the cross correlation, except that it is more noisy. See Fig. 3.30 for the cross correlation peak.

The actual peak position

After the transformation back to the spatial domain the correlation is given as a discrete peak, see Fig. 3.33. The displacement $\Delta\vec{s}$ is given as the peak position of the continuous correlation.

The actual peak position will be somewhere between these "peaks" calculated, at some subgrid scale. This means that there is a need for interpolation to find the actual position. Many authors have described interpolating schemes to detect the peak (e.g Westerweel 1993 or Lourenco 1996). Four such interpolators are

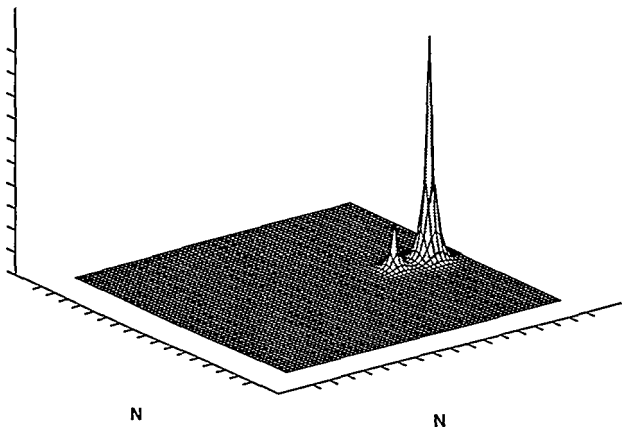

Figure 3.32: The result of the single frame correlation for image shift greater than half the interrogation area

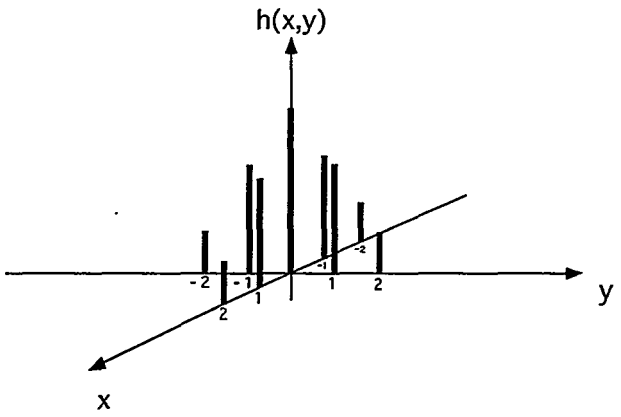

Figure 3.33: The digital peak

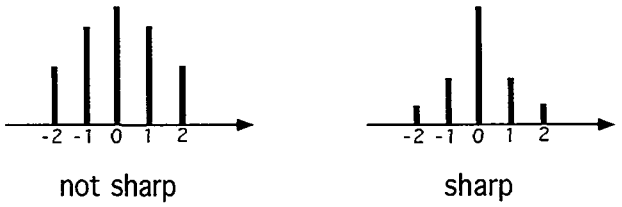

Figure 3.34: The shape of the digital peak

- Centre of gravity. a widely used interpolator. This requires that the centred of the five elements is the strongest one. This interpolator is very robust, but not sensitive to the sharpness of the digital peak
- Parabolic interpolator. This uses a parabolic function to find the peak position. Better than the centre of gravity, because it assumes a shape of the peak
- Gaussian interpolator. This is similar to the parabolic one. It assumes a gaussian shape of the peak, and therefore also better than the centre of gravity
- Whittaker reconstruction. To increase the resolution of the gaussian and parabolic interpolators zeros are added to the Youngs fringes before transforming back to the spatial domain (zero padding). This only increase the distance between the fringes. The time needed for the inverse transform will increase by a factor of four. The Wittaker reconstruction is an alternative. It offers a comparable accuracy as parabolic and gaussian interpolators, but no zero padding is needed. Therefore the Whittaker reconstruction is much more computational efficient (Lourenco 1996).

3.4.3 Fourier methods

In the same way as for the correlation methods, the intensity pattern $i(x,y)$ is transformed to the Fourier plane. The transform of the first exposure is

$$\mathcal{F}[i(x,y) \otimes \delta(x,y)] = \hat{I}(u,v) \tag{3.56}$$

and for the second one

$$\mathcal{F}[i(x,y) \otimes \delta(x+\Delta x, y+\Delta y)] = \hat{I}(u,v) e^{-j2\pi(u\Delta x + v\Delta y)} \tag{3.57}$$

The difference between these two Fourier transforms lies in the phase angle between them.

$$\Delta\phi = 2\pi(u\Delta x + v\Delta y) \tag{3.58}$$

By solving Eq. 3.58 for frequency pairs (u_i, v_j), the displacement $\Delta\vec{s} = (\Delta x, \Delta y)$ can be found. The difference between the predicted frequency pairs (u_i, v_j) and the computed

phase difference $\Delta\phi_{ij}$ is minimized by means of least square. Equation 3.59 is used to find Δx and Δy.

$$\frac{\partial E_{ij}^2}{\partial \Delta x} = \sum_{ij}(u_i\Delta x + v_j\Delta y - \frac{\Delta\phi_{ij}}{2\pi})u_i = 0$$
$$\frac{\partial E_{ij}^2}{\partial \Delta y} = \sum_{ij}(u_i\Delta x + v_j\Delta y - \frac{\Delta\phi_{ij}}{2\pi})v_j = 0 \tag{3.59}$$

3.4.4 Statistical methods

The displacement $\Delta\vec{s}$ is found by constructing a two dimensional histogram of the distance between particle pairs in a part of the image. The velocity is given by the most frequent distance between particles in this region. This method was proposed by Takai and Asakura in 1983.

3.4.5 Neural Networks

Lately a new approach to analyze PIV-images has been proposed. It is based on a new type of programming structure.

The most common way of programming is to tell the computer to do one thing at a time. As the computer technology develops new types of computers become available, such as parallel processor computers. A new programming structure called artificial neural network (an imitation of the humane brain) is suitable for such a computer.

This technique of programming is now used in many different areas (weather forecast, voice recognition among others). Carosone and Cenedese (1996) have developed this technique for use in Particle Tracking Velocimetry (low density PIV). They have found that after the "training" period, the neural network method used on Young fringes where much faster than the standard inverse Fourier transform (~200 times). The problem with this method is that the training period is quite long for the time being (~ 5 hours).

3.5 Special considerations in PIV

There are some special considerations that are important for PIV. The problem of directional ambiguity, seeding of flow and so on. Some of these effects will be described in this section.

3.5.1 The directional ambiguity

The problem of determining the flow direction has to be solved to avoid limiting the PIV-technique enormously. If unsolved, PIV can not be used for recirculating flows for example.

When the cross correlation is used, each of the exposures are "saved" on different frames. In this mode there is no problem with flow direction. The problem with this technique is the recording media. The need to acquire images with high speed is extensive. Today high speed cameras have poor spatial resolution. If high spatial resolution is required, the speed of acquiring images is slowed down dramatically because of limitations in data rate transfer between camera and the storing media, or by the flexibility to acquire images. This means that cross correlation for the time being only can be applied to applications which only require low spatial resolution (Kompenhans, Raffel, and Willert 1996).

If the exposures are saved on the same image, the two exposures can not be separated from each other, and the cross correlation mode can not be applied to this image. There are several ways of solving this problem, and these can be divided into two groups.

- Pulse coding
- Image shifting

Pulse coding

The idea of the pulse coding is to make the two exposures in the image separable by differentiating them either by colour (see Fig. 3.35) or by shape (see Fig. 3.36). If a colour recording media is used, green light can be used for the first exposure and red on the second one. The two exposures can then be separated, and normal cross correlation can be applied.

If there is no possibility of using colours, another way is to provide different pulse codes that can be used to detect the direction when processing the image afterwards. Adrian (1986) gives examples of different pulse codings.

The problem with all these methods is that they can not be applied to high densities of particles, i.e. they can only be used for particle tracking (Adrian 1988).

Image shifting

Yet another method for solving the directional ambiguity, is to provide image shifting. This means to translate the recording media by a known uniform amount between the two exposures. The flow field is recorded in a moving reference, which means that a known velocity bias is superimposed on the actual velocity. This method was introduced to PIV

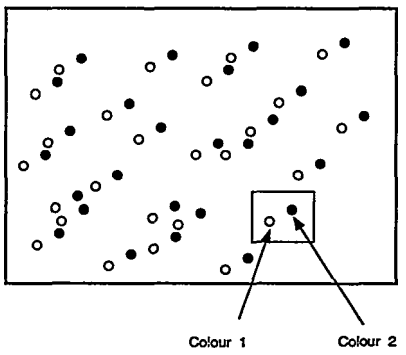

Figure 3.35: Colour coding to solve the directional ambiguity

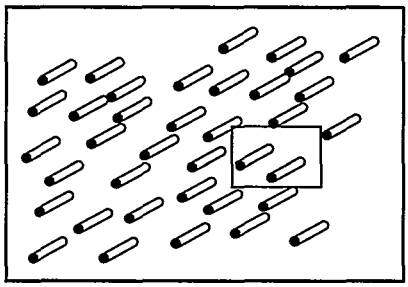

Figure 3.36: Pulse coding to solve the directional ambiguity

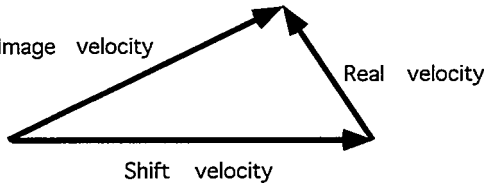

Figure 3.37: The idea of image shifting

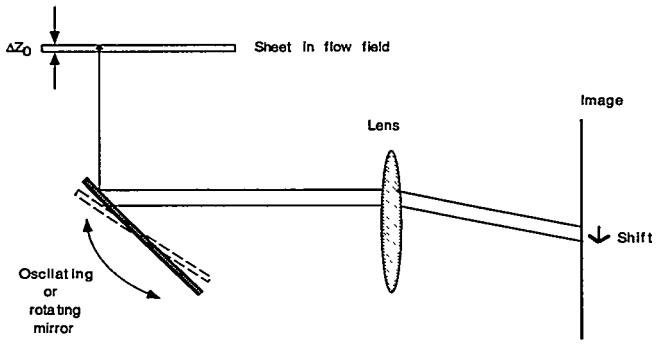

Figure 3.38: Image shifting by rotating/oscillating mirror

by Adrian (1986) among others. This method will improve the dynamic range of a PIV system (see Section 3.5.2), as well as solve the problem with direction.

There are several ways that the image shift can be provided. They can be divided into two groups.

- Image shifting by optical means
- Image shifting by physical translation

Image shifting by optical means This is the most commonly used technique of providing image shifting. Several authors have reported techniques that come into this group. Adrian (1986), Landreth et al. (1988) and Kompenhans et al. (1996) have reported work using a rotating or oscillating mirror.

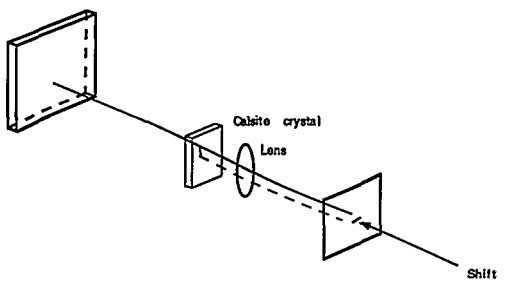

Figure 3.39: Image shifting by bifringent crystal

The recording area in the camera "sees" the observation area in the flow field trough a rotating or oscillating mirror, see Fig. 3.38. The shift applied depends on several things. The angular speed of the mirror. The distance between the mirror and the light sheet, the magnification of the imaging system and the time delay between the two pulses. The advantages of this type of system are

- It can easily be implemented into an already existing PIV-system.
- Negligible depolarisation effects.
- The shift velocity can be adapted very easily.
- The shift velocity range is very high.

The main disadvantage with the mirror system is that it can not be synchronized with a non-periodic flow event. The position of the mirror controls the opening of the recording media and timing of the light pulses.

The disadvantages of the mirror system type have been pointed out by several authors. Other types have been suggested for passive image shifting systems that do not require the movement of mechanical components. Landreth and Adrian (1988) switched the polarisation of the illuminating beam, the light scattered from the seeding particles was then polarised. Then they placed a birefringent crystal, calcite, in front of the lens to displace the particle images between the two exposures, see Fig. 3.39. They did use a "pocket cell" to rotate the polarisation 90°.

The advantage is that it is quite effective, provided that most of the light scattered by the particles retain its original state of polarisation. This is true for particles and optics used in PIV. The disadvantage with this method is that the amount of shift for a given

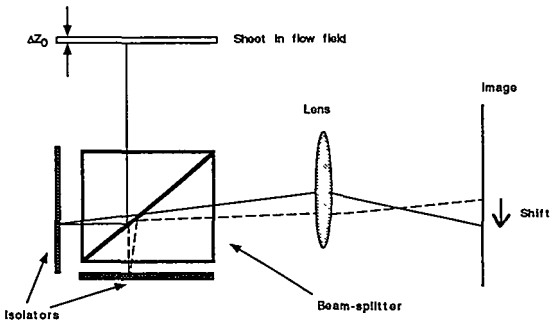

Figure 3.40: Image shifting by beam-splitter/isolator arrangement

magnification can not be changed unless the crystal thickness is varied. Lourenco (1993) used a polarisation beam splitter cube and two isolators, see Fig. 3.40.

Both of these methods are based on the idea of rotating the polarisation direction of the laser light and reflecting particles. This means that flourecent particles can not be used. Bertuccioli et al. (1996) have proposed another type of system based on bifringent and ferro electrical liquid crystals. This system can be used for fluorescent particles. The disadvantages are that the minimum pulse separation for this system is $100\,\mu$sec., and excitation of unwanted rays are not perfect. Not perfect means that "ghost images" (image of particles that does not exist) are present in some of the brighter areas of the image.

Image shifting by physical translation Another way of producing image shifting is by moving the recording media. The first attempts to this were to move the whole camera a known distance between the two pulses. But this is not easy to control, and quick translation is in practice not possible, so this method can only be used for small shift velocities. Wormell and Sopchak (1993) used a CCD camera in which the charge (light) associated with the first pulse is moved electronically a few pixels before the second light pulse. The advantage of this technique compared to translation of the whole camera is that this does not involve mechanically moving parts. Since there are no moving parts, the minimum pulse separation can be as short as $\sim 40\,\mu$sec. The disadvantage of this system is that CCD cameras already have a limited number of pixels. By cutting of a part of the sensor (certain number of pixels) for use in the shifting, the resolution of the imaged area is limited even more.

3.5.2 The dynamic range of a PIV system

The dynamic range refers to the maximum difference in velocity that the PIV system can resolve within a flow field. The upper range is set by the fact that the displacement can theoretically not be more than the interrogation area size, and in practice not more than half the interrogation area length (Lourenco and Krotapalli 1987). The minimum distance that the particles can move is one diameter to be able to look at it as particle pairs. This gives

$$\Delta t = \frac{l_{\text{int}}}{2M} \tag{3.60}$$

where l_{int} is the length of the interrogation area. The minimum velocity will be given by

$$|\vec{U}_{\text{min}}| = \frac{d_i}{\Delta t} \tag{3.61}$$

which gives

$$\frac{d_i}{|\vec{U}_{\text{min}}|} = \frac{l_{\text{int}}}{2M|\vec{U}_{\text{max}}|} \tag{3.62}$$

Given as a normalized velocity difference, the velocity dynamic range is given by

$$\frac{|\vec{U}_{\text{max}}| - |\vec{U}_{\text{min}}|}{|\vec{U}_{\text{min}}|} = \frac{|\vec{U}_{\text{max}}|}{|\vec{U}_{\text{min}}|} - 1 = \frac{l_{\text{int}}}{2Md_i} - 1 \tag{3.63}$$

3.5.3 Increasing the number of exposures in a single frame

Lourenco and Krotapalli (1987) have reported an improved signal to noise ratio (SNR) for the auto correlation by increasing the number of exposures to three. If we look at the intensity pattern of a multiple exposure image it is given as

$$d(x,y) = i_1(x,y) + i_2(x,y) + i_3(x,y) + \ldots\ldots\ldots\ldots\ldots\ldots \tag{3.64}$$

This gives

$$d(x,y) = i(x,y) + \sum_{n=1}^{N} i(x + n\Delta x, y + n\Delta y) = i(x,y) \otimes [\sum_{n=0}^{N-1} i(x + n\Delta x, y + n\Delta y)] \tag{3.65}$$

where N is the total number of exposures.

The Fourier transform in this case will be

$$\hat{D}(u.v) = \hat{I}(u,v)[1 + \sum_{n=0}^{N-1} e^{-j2\pi(nu\Delta x + nv\Delta y}] \tag{3.66}$$

and its complex conjugate given as

$$\hat{D}(u,v) = \hat{I}(u,v)[1 + \sum_{n=0}^{N} e^{j2\pi(nu\Delta x + nv\Delta y}] \tag{3.67}$$

With

$$e^{jz} = \cos z + j\sin z \tag{3.68}$$

and

$$e^{-jz} = \cos z - j\sin z \tag{3.69}$$

the spectrum becomes

$$\hat{D}(u.v)^2 = |\hat{I}(u,v)|^2\{N + \sum_{n=1}^{N-1} 2n\cos[2\pi(N-n)(d\Delta x + v\Delta y)]\} \tag{3.70}$$

Then the auto correlation function is given as the inverse Fourier transform of $\hat{D}(u,v)^2$.

$$\begin{aligned} h(x.y) \;&= \mathcal{F}^{-1}[\hat{D}(u,v)^2] \;= Nr(x,y) + \sum_{n=1}^{N-1}(N-n)r(x+\Delta x, y+\Delta y) \\ &\quad + \sum_{n=1}^{N-1}(N-n)r(x-\Delta x, y-\Delta y) \end{aligned} \tag{3.71}$$

Compared to Eq. 3.41 the self-correlation peak has increased in strength. If we define the signal-to-noise ratio (SNR) as the ratio between the self-correlation peak and the first one offset of this. the peak at the displacement, SNR is given by

$$\text{SNR} \propto \frac{N-1}{N} = 1 - \frac{1}{N}, \quad N \to \infty \Rightarrow \text{SNR} \to 1 \tag{3.72}$$

SNR is increased in strength with increasing number of exposures as found by Lourenco and Krotapalli (1987). It is not meaningful to use more than four or five exposures, because the problem of moving out of the interrogation area will occur if there are too many exposures. The benefit of increasing the number of exposures any further is lost.

3.5.4 Error-sources in PIV

There are lots of sources that might lead to error in PIV measurements. These error-sources can be divided into three different groups.

- Particle, seeding and flow
- Recording
- Evaluation

Particle, seeding and flow

This category includes all errors due to the particle themselves, the concentration of particles and the flow field. Non-uniform size of the particles, locally varying concentration due to e.g. centrifugal forces in vortices or generally low seeding in the interrogation area and loss of image pairs due to significant out of plain motion. All these effects may lead to a low signal to noise ratio and a noisy correlation field, and in addition no peak detection.

In the case of non-constant displacement of particle images in the interrogation area due to smaller length scales in the flow field than the size of the interrogation area, there may be a signal peak present but at slightly different location than the correct one.

Recording

Light reflection from the surface of the model investigated and recording optics not exactly focused might reduce the SNR, and no peak detection is possible.

Evaluation

Noise of video camera and/or noise in the video A/D converter might also lead to bad signal to noise ratio and problems in peak detection.

Chapter 4

Experimental setup

4.1 The water tunnel

The water tunnel used has a vertical test section of 1 m×0.14 m×0.14 m. The capacity of the tunnel is $Q_{max} = 0.027\,m^3/s$, which gives a maximum velocity of 1.5 m/s. The walls in the test section are made of glass, which makes the tunnel suitable for PIV and LDV measurements. Figure 4.1 and Fig. 4.2 give a schematical description of the tunnel.

Water is pumped from the lower reservoir by a centrifugal pump to the upper reservoir, which acts as a settling camber. To maintain a constant total pressure, the overflow water is lead back to the lower reservoir. This gives also the advantage that we can produce very modest flow velocities in the test section. In the settling chamber four screens are used to reduce the flow pulsations the water. From the settling chamber the water is lead trough a 2.8 m long vertical channel, $0.65\times0.65\,m^2$. There are 6 screens and a honeycomb in this part of the tunnel.

The inlet to the test section is a 0.6 m long nozzle with a contraction ratio of 21.5 : 1. The test section has been investigated with LDV (Dahlsveen and Morud 1990), and the velocity profile across the test section is uniform with a deviation of 0.07%, outside the wall boundary layers.

4.2 The PIV system

The PIV system at MTF-Fluid dynamics consists of two parts. One high resolution film based system, and a second low resolution CCD based cross correlation system with 18 frames per second.

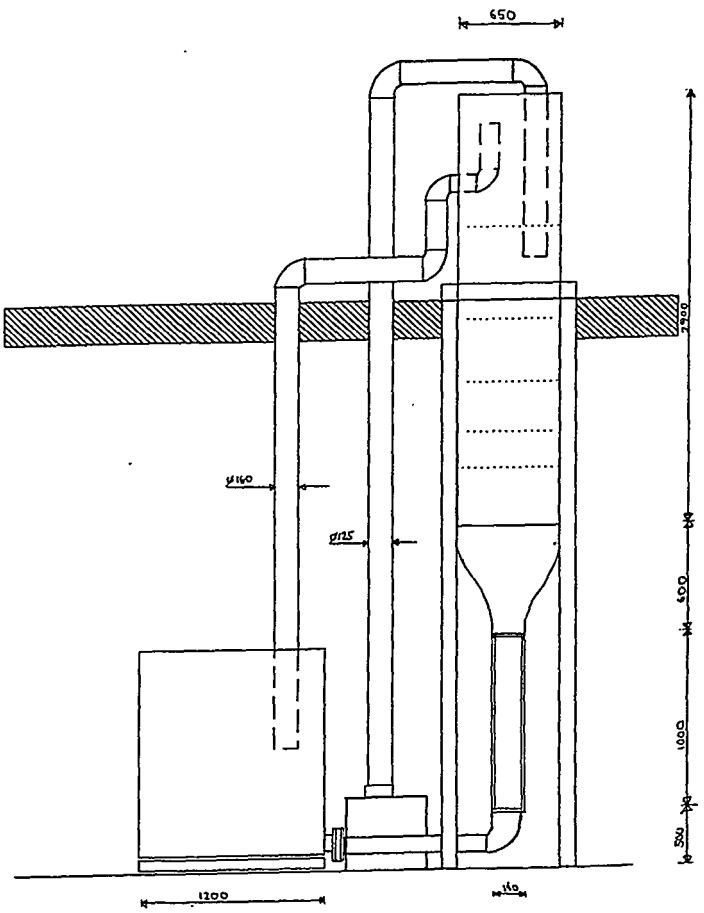

Figure 4.1: Front view of the water tunnel used

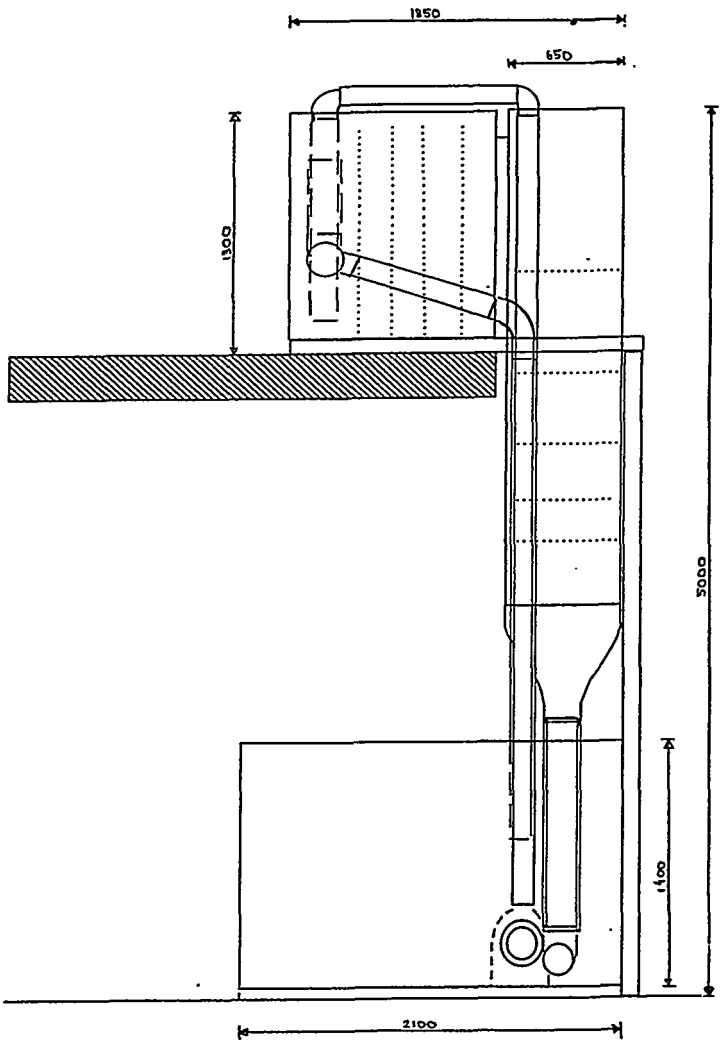

Figure 4.2: Side view of the water tunnel used

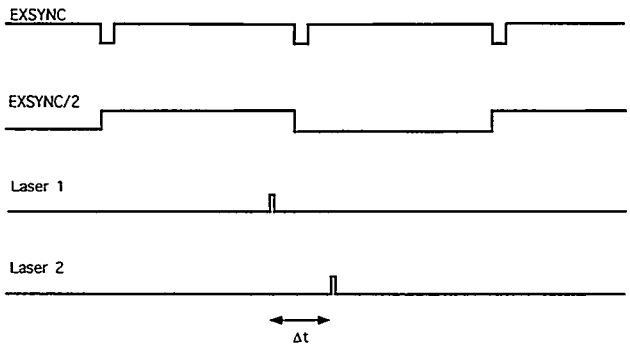

Figure 4.3: The control signals for the light pulses

4.2.1 The cross correlation system

For the cross correlation system a non-standard CCD camera is used. A frame grabber sends a control signal to the camera (EXSYNC) and to the light source unit.

The EXSYNC-signal tells the camera when to illuminate the CCD (EXSYNC high) and when to read the image (EXSYNC low). In the light source unit the start of every second frame is found. This makes it possible to pulse the light source at the end of frame one and at the beginning of the second, see Fig. 4.3.

The camera used is a DALSA CAD1-0256S. This is a full frame camera with 256×256 pixels (active 250×240). The camera is controlled by a Matrox Magic EISA frame grabber. The framegrabber is mounted in a 486-DX2 PC. The light pulses are produced by two Continium Minilite-10 ND:YAG lasers. They produce an energy of 10 mJ 532 nm in 4−−6 nano second pulses.

The repetition rate of a Minilate-10 laser is 10 Hz. This means that the maximum frame rate with one pulse per frame and two lasers is 20 Hz. Therefore we have chosen a framerate of 18 Hz.

The pulse separation Δt (see Fig. 4.3) and the trigging of the grabber PC is controlled by a Power Macintosh 7200 PCI based computer. The computer has a NI-PCI1200 IO-board and LabView software. The control program is an inhouse-made LabView VI.

To interface the grabber PC, lasers and controller PC, an inhouse-made connection box is used. The box inverts the trigger pulse for the lasers, and finds the start of every second frame to use as a trigger for the IO-board. A schematical drawing of the cross correlation PIV system is given in Fig. 4.4.

The particles used are hollow glass spheres coated with silver. They are 12 μm in diameter and have a specific gravity of 1.17 with 20% silver coating.

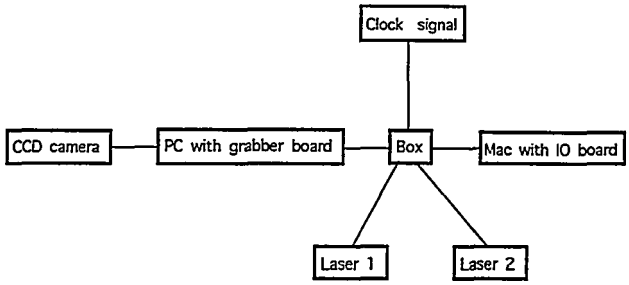

Figure 4.4: The cross correlation system

The images produced are stored as .tif-files in the grabber PC. These .tif-files are processed by the commercial PIV-software VisiFlow from AEA Technologies. Two pictures are used to produce one PIV-picture by cross correlation.

Measurements were taken in the flow of the empty test section, both with 64×64 and 128×128 pixels in one interrogation area. In each series of measurements 104 frames were taken, which gives 52 PIV pictures with a repetition rate of 9 Hz.

The mean for each field is given in Fig. 4.5. In the same figure one position in the field is given.

By finding the mean and rms for the time varying field mean, the result can be compared with the LDV measurements obtained by Dahlsveen and Morud (1990). The measurements show that there is almost no difference between 64×64 and 128×128 pixels interrogation area. The turbulence measured based on the 64×64 data is 0.39%. This is in the same range as measured by Dahlsveen and Morud (1990), and confirm that the PIV-technique is capable of measuring these low turbulence levels. The level measured is about 0.15% lower than measured using LDV. One reason for this is that the measuring area using LDV is 1/200 of the interrogation area in the PIV measurements. There is an integration over a larger area, and which reduces the turbulence level somewhat.

4.2.2 The high resolution film-based camera system

For this system we use a film camera, NIKON N90s. This is a single frame double pulse system, and therefore an image shifting option is provided. See Fig. 4.6 for a description of the system.

For the image shifting system we use a $60 \times 40\,\mathrm{mm}^2$ aluminum mirror specially designed for green light, 532 nm. The electromotor to run the mirror is an Cambridge Technology product especially designed for accurate positioning. Two Continium Minilite 10 ND:YAG lasers are used to produce the two light pulses on each frame.

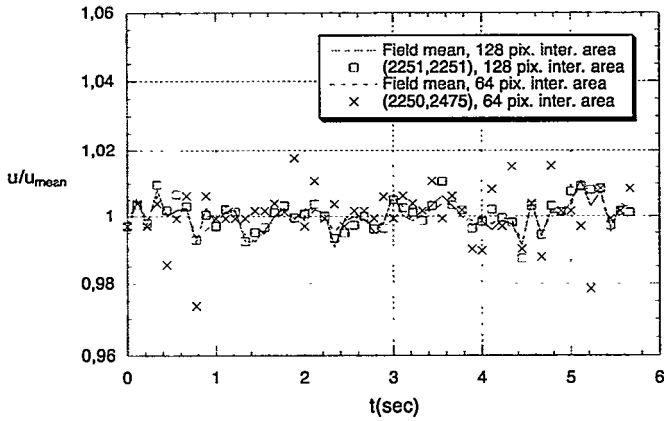

Figure 4.5: The freestream measured with PIV

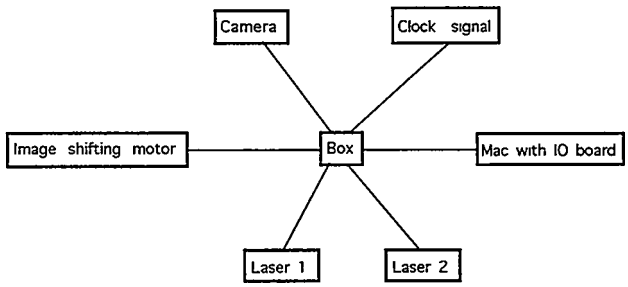

Figure 4.6: The film based PIV system

To control camera, mirror and lasers a Macintosh with IO board and Labview is used. An inhouse-made box is used to interface all the parts (see Fig. 4.6 for description of the system).

The computer is used to produce a -5 to $+5$ Volt analog signal that is multiplied by 2 by the inhouse-made box.

This analog signal, produced by an inhouse-made Labview VI is used to drive the mirror. A control signal from the mirror gives the actual position of the mirror. This control signal is used to trigger the camera and the lasers.

The film type used is normally a black and white film, Kodak Tmax pro. After exposure, the film negatives are digitised by a Polaroid Sprint Scan 35 negative scanner. They are stored as .tif-files and processed by the same software as for the cross correlation system.

The resolution in this case is much higher than for the cross correlation system. A 35 mm film has an area of $36 \times 24\,\mathrm{mm}^2$ which gives a pixel resolution of up to 3800×2550 pixels in one digitised image.

4.2.3 Testing of the PIV-system on grid generated turbulence

The PIV cross correlation system was used to measure grid generated turbulence. Normally grid generated turbulence is divided into four different stages downstream of the grid,

- Build-up period
- Initial period of decay
- Transition period of decay
- Final period of decay

Build-up period starts just after the grid, and is normally defined as far as $5M$ to $10M$ downstream the grid (Batchelor 1953), see Fig. 4.7 for a description of M. In this stage the turbulence is neither homogeneous nor isotropic (see e.g. Hinze 1975 for definition of homogeneous and isotropic turbulence). The grid produces jet and wake areas, and these have not been able to mix this close to the grid. The flow in this area will be strongly influenced by these jet-wake interactions.

Initial period of decay is the next stage of the grid generated turbulence. It starts were the build-up period ends and goes down to $\frac{x}{M}$ between 100 and 150. In this period there is a distinct separation between the strong vortices with much energy and the dissipative vortices. The dissipative vortices are dependent on the viscosity, and are small. On the other hand, the strong vortices with much energy are dependent on the size if the grid, and will not be affected by the viscosity.

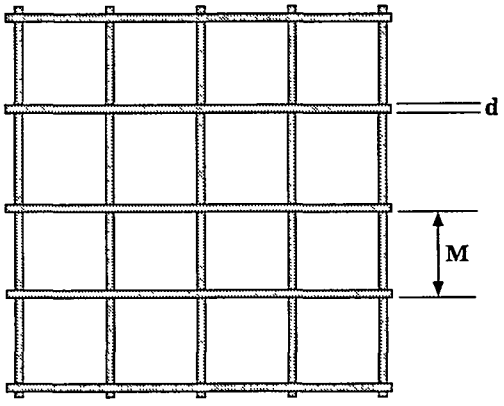

Figure 4.7: The different grid parameters

Transition period of decay The change between the stages in grid generated turbulence is weak. and strongly dependent on the Reynolds number based on the mesh size, Re_M. This stage is normally looked at as an intermediate stage between the *Initial period of decay* and the *final period of decay.*

Final period of decay Townsend (1956) has shown that this period can last for more than $500M$.

The size of the grid used in these measurements is

$$M = 14.0\,\text{mm} \tag{4.1}$$
$$d = 3.0\,\text{mm} \tag{4.2}$$
$$\beta = 63\% \tag{4.3}$$

where d and M is given by Fig. 4.7, and β is given by Eq. 4.4.

$$\beta = 1 - \frac{d^2}{M^2}(2\frac{M}{d} - 1) \tag{4.4}$$

The size of the test section and the size of the grid do not make it possible to measure in all the different stages. Therefore the measurements are done in the first part of stage two, *the initial period of decay.*

In these tests the PIV-pictures were used to calculate the dissipation scale λ. λ is defined as

$$\lambda_g^2 = \frac{u'^2}{\overline{(\frac{\partial u_1}{\partial x_1})^2}} \tag{4.5}$$

Table 4.1: PIV results from grid-generated turbulence

Point	$\frac{u'}{v'}$	$\frac{u'}{\overline{U}}$
1	1.18	2.77%
2	1.09	2.54%
3	1.07	2.67%

(see page 66 in Tenekes and Lumley 1972).

150 PIV-pictures were used, with six $\frac{\partial u_1}{\partial x_1}$ and u'^2 found from each picture. This gives a total of 900 $\frac{\partial u_1}{\partial x_1}$ and u'^2 used to calculate

$$\lambda_g = 1.43\,\text{mm} \tag{4.6}$$

with $x/M = 30$, $\overline{U} = 1.48\,\text{m/s}$ and $Re_M = 20300$.

Dahlsveen and Morud (1990) found from their LDV measurements $\lambda_g = 1.5\,\text{mm}$ for $x/M = 30$, $\overline{U} = 1.46\,\text{m/s}$ and $Re_M = 20300$. They did use the Taylor's hypothesis, see e.g. Hinze (1975).

Batchelor (1953) has shown that λ_g for grid generated decaying turbulence may be written as

$$\lambda_g^2 = \frac{10\nu}{\overline{U}}(x - x_0) \tag{4.7}$$

were x_0 is between $5M$ and $10M$. For $x/M = 30$ and $\overline{U} = 1.48\,\text{m/s}$ λ_g will be between 1.37 mm and 1.54 mm.

Three different positions in the field were also used to find u'/v' and $u'/\overline{U}$, see Table 4.1.

Dahlsveen and Morud (1990) did get

$$\frac{u'}{v'} = 1.1$$
$$\frac{u'}{\overline{U}} = 2.9\%$$

From these results we can state that the PIV-system can be used to measure turbulent flows, and also get the same results as LDV for some quantities.

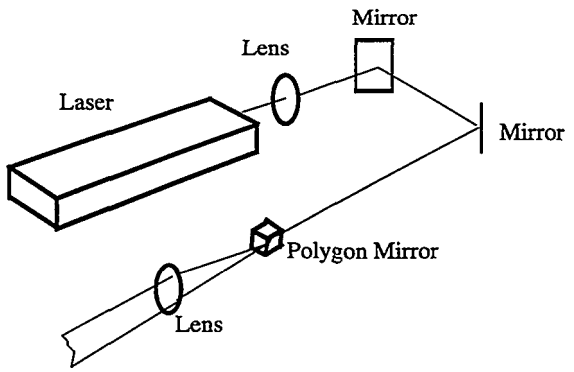

Figure 4.8: A sketch of the laser visualisation system

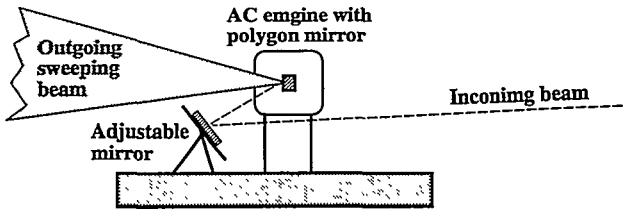

Figure 4.9: A closeup look at the polygon mirror system

4.3 The laser sheet visualisation system

The laser sheet visualisation system is based on a 5 W Ion Argon laser from LEXEL. It produces green light at 514 nm. A sketch of the system is shown in Fig. 4.8.

At the opening of the laser a lens with a long focal length is placed. The purpose of the lens is to gather the beam, and make it be convergence through the whole area that is to be illuminated. The two mirrors are used to lead the beam into the rotating polygon mirror system, see Fig. 4.9 for a closeup of the rotating polygon mirror system.

An AC engine is used to drive the polygon mirror. By using an AC engine the rotating speed becomes very stable. This is important if the visualized pictures are to be used for flow velocity predictions. To regulate the rotation speed a SIEMENS Micromaster inverter is used. With the use of the inverter the rotation speed may be changed from 1 rpm to 18000 rpm.

The polygon mirror is placed at the focal point of another lens. This lens is used to change the direction of the sweeping beam. The laser beam will always be normal to the windows in the test section. By doing this the reflection of the laser beam is hidden inside the main beam. Figure 4.10 shows how the reflected beam will be with and without the last lens.

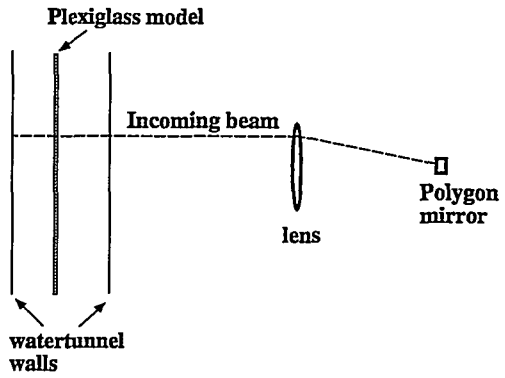

(a) Using the lens

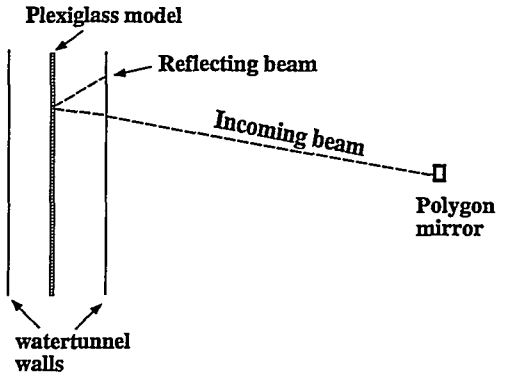

(b) Without the lens

Figure 4.10: A sketch of the reflecting laser beam

The particles used are the same as used in the PIV system, see section 4.2.

Chapter 5

Visualisation

The main task of flow visualisation is to make the flow events visible for the human eye. In this work laser sheet flow visualisation will be used to characterize the flow inside the cavity. For a description of the laser sheet visualisation system see Chapter 4. The latest supplement to the visualisation techniques is the quantitative PIV-Technique. Since it produces vector fields, it may be classified both as a visualisation technique and as a measurement technique. The three different cavity geometries used were the same as used by Løland, Sætran, and Sakariassen (1998). For a description of the different cavities see Fig. 5.1.

5.1 Visualisation using laser sheet

As a part of these visualisations both photo and video were used as a recording medium. The video part was done by using a PULNIX CCD camera with a NIKON 50 mm 1:1,8 lens and a Panasonic Super VHS video recorder. For the photo part a NIKON camera with the same lens was used. The film was a Kodak TMAX Pro 3200. The negatives were digitised by using a Polaroid Sprint Scan 35 with Adobe Photoshop LE software.

Figure 5.2 and Fig. 5.3 show two arbitrarily chosen photos from the sloping cavity pointing in the flow direction.

As seen from the two pictures there is one vortex in the upper part, and smaller one further inside the cavity. The difference between these two pictures show the in and outflow into the cavity. This is clearly visualized near the downstream corner (to the right in the pictures).

For the other configuration in an ultrasonic flowmeter, the cavity is placed pointing countercurrent. Figure 5.4 and Fig. 5.5 show two pictures taken in this geometry.

The pictures show that the vortex system is different in this case. There is a small fast vortex at the downstream corner, and a bigger slow one covering the whole cavity width

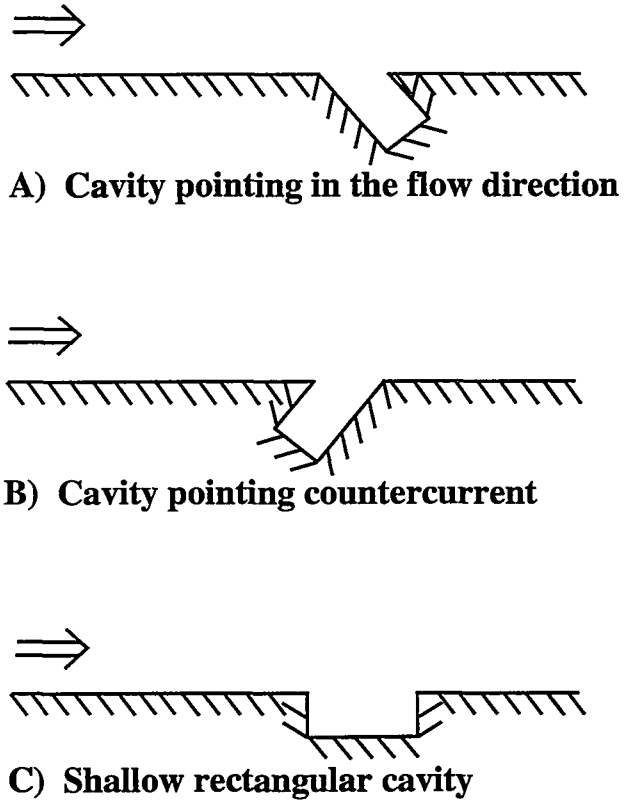

Figure 5.1: The three different geometries used in the present study.

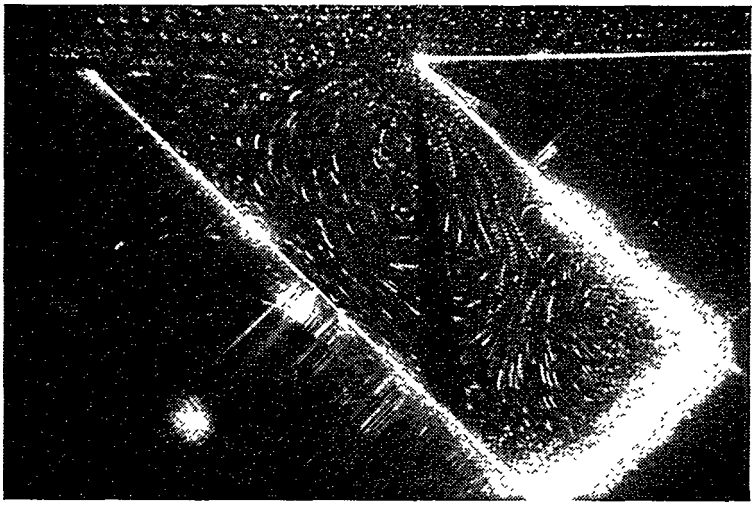

Figure 5.2: A picture from the sloping cavity pointing in the flow direction. This picture is from setup A. Main flow from left to right.

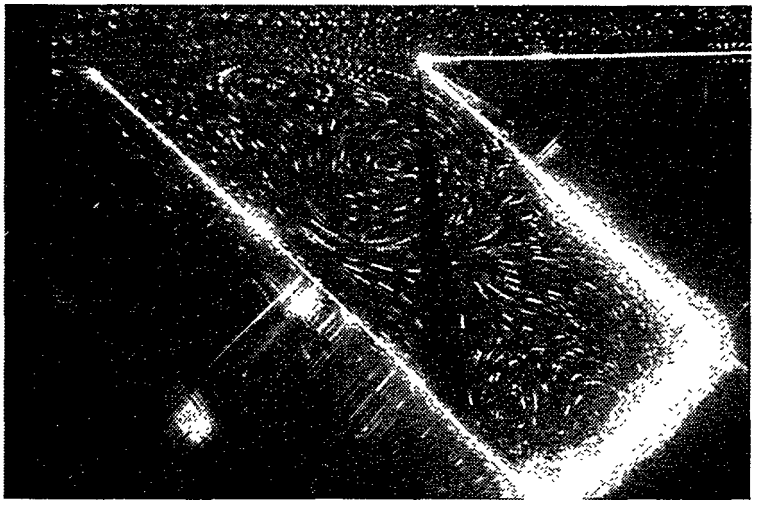

Figure 5.3: A picture from the sloping cavity pointing in the flow direction. This picture is from setup A. Main flow from left to right.

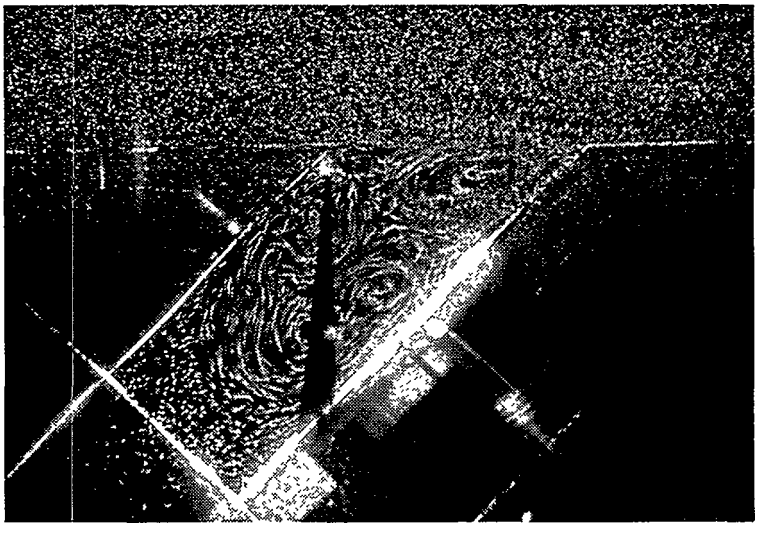

Figure 5.4: A picture from the sloping cavity pointing countercurrent. This picture is from setup B. Main flow from left to right.

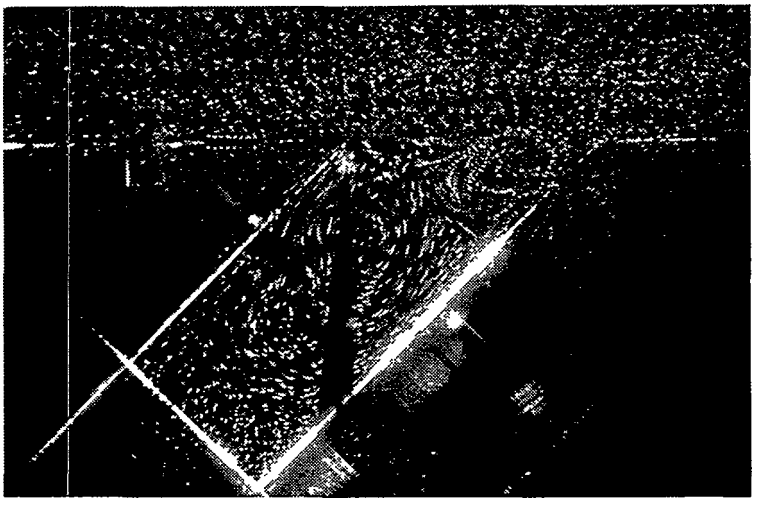

Figure 5.5: A picture from the sloping cavity pointing countercurrent. This picture is from setup B. Main flow from left to right.

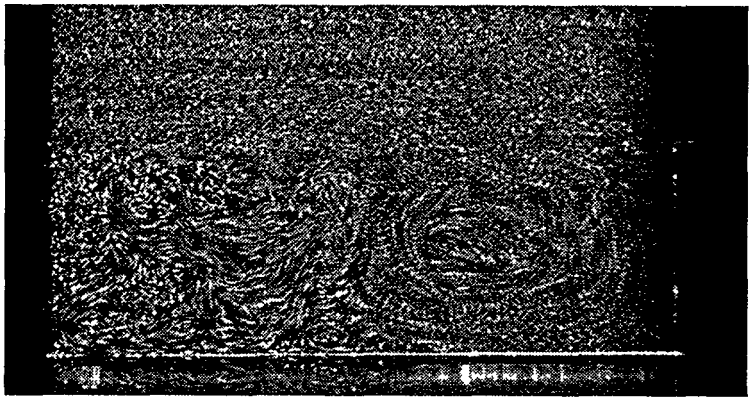

Figure 5.6: A picture from the rectangular cavity. This picture is from setup C. Main flow from left to right.

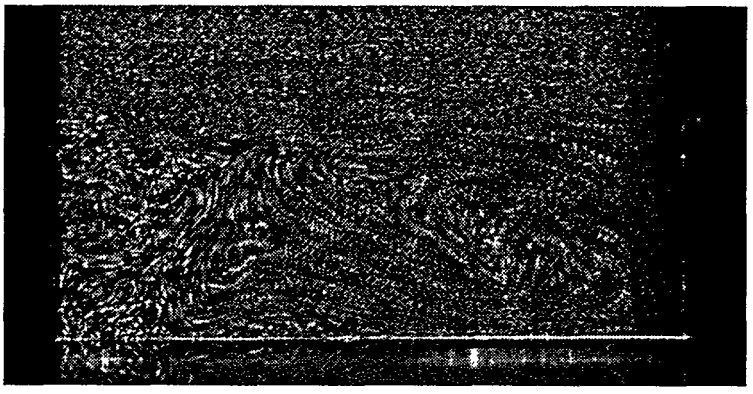

Figure 5.7: A picture from the rectangular cavity. This picture is from setup C. Main flow from left to right.

in the lower part of the cavity. The speed of the vortices is not shown on these pictures. The video show that the small vortex is the faster one. The small vortex as shown in these pictures do not appear in the opposite ultrasonic flow meter cavity. Also visible in these pictures is the stagnation point in the cavity at the downstream wall. This means that the vortex structure depends on the orientation of the cavity.

The third geometry used was a rectangular cavity of dimension $D = 20\,\text{mm}$ and $W = 60\,\text{mm}$. This type of cavity was studied by eg. Sarohia (1977) and Ethembabaoglu (1973). Figure 5.6 and Fig. 5.7 show two pictures taken in the rectangular cavity.

As seen in the pictures there is a stagnation point at the downstream wall. There is also clearly visible a vortex, which is placed at the downstream part of the cavity. Further upstream there is no clear vortex. The stagnation point indicates that there is flow into

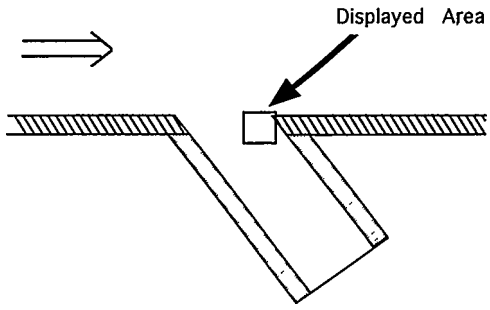

Figure 5.8: The measured area in the cavity pointing in the flow direction.

the cavity. The downstream corner and wall will then set up the border for the flow going into the cavity. Since there is flow into the cavity, outflow will also have to be present. This gives the boundaries for the cavity flow, which sets up a vortex structure. The same results are described by Ethembabaoglu (1973).

5.2 Visualisation using Particle Image Velocimetry, PIV

The inhouse-made PIV-system described in Chapter 4 was used to measure flow fields. The system was used as a cross correlations system, which takes care of the flow direction. This system makes it possible to take 130 pictures in series, which produce 65 PIV fields with a 9 Hz sampling rate. The main disadvantage with this system is the limited number of pixels in the camera, only 250×240 active pixels. In practice this did limit us to study only parts of the cavity at a time. The time between the laser pulses was set in a way that we always ensured that the particles had moved more than one pixel (the smallest velocities), and not more than 35% of the chosen interrogation area. Velocities detected showing greater displacement than half the interrogation area ($s = v \cdot t$) indicated that they were bad vectors. Also velocities smaller than 2 pixels displacement would also be a bad vector. This time in the sense that we were not able to detect the velocity. The time between the pulses, Δt, was adjusted to find the best hit for Δt to minimize the numbers of bad vectors in the fields. Also LDV measurements were used to confirm the PIV measurements.

The analysis program Visiflow has the option to display mean fields and streamlines when time series have been captured. In our investigations the two ultrasonic flowmeter cavity models were studied.

Figure 5.9 and Fig. 5.10 show two discrete time shots of the downstream corner for the

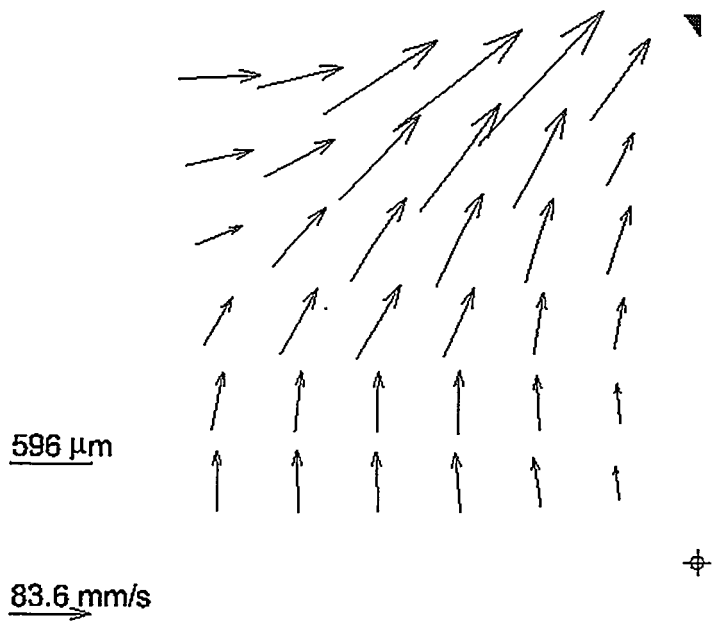

Figure 5.9: A PIV field taken in the cavity pointing in the flow direction.

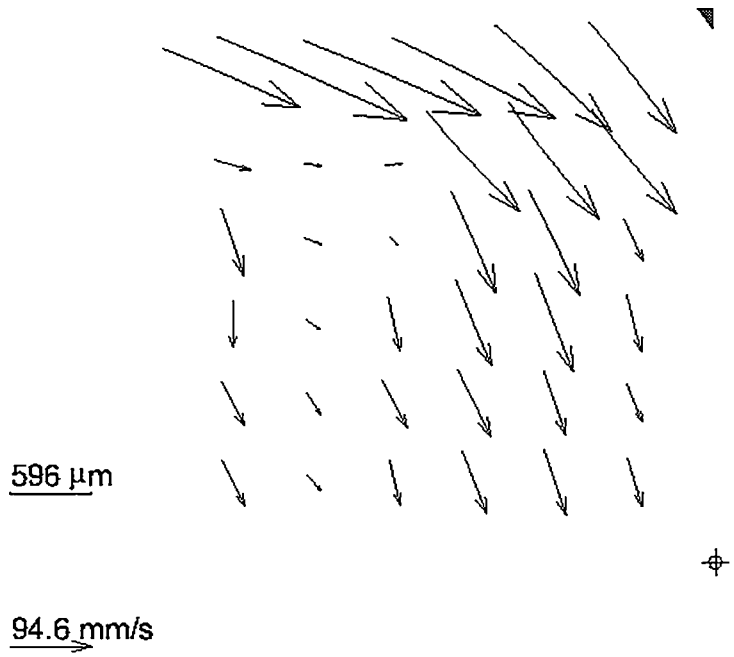

Figure 5.10: A PIV field taken in the cavity pointing in the flow direction.

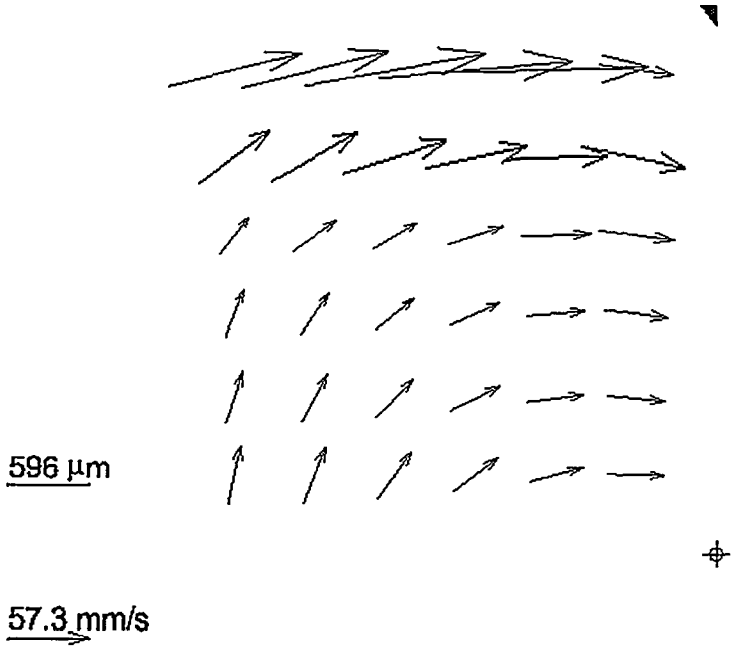

Figure 5.11: The PIV mean field in the cavity pointing in the flow direction.

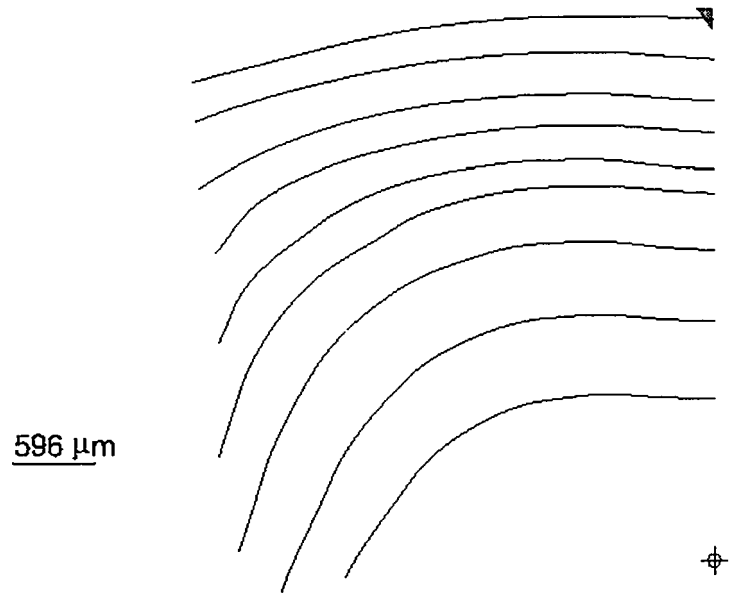

Figure 5.12: The PIV streamlines in the cavity pointing in the flow direction.

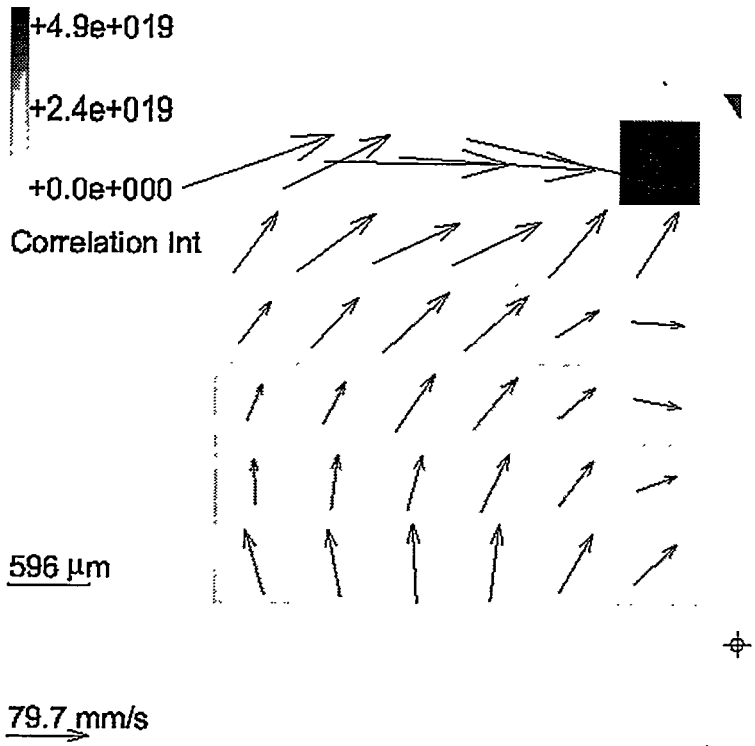

Figure 5.13: The PIV correlation field in the cavity pointing in the flow direction.

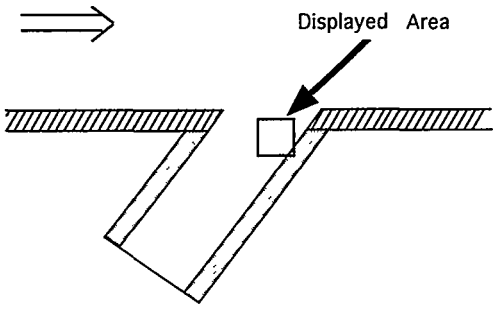

Figure 5.14: The measured area in the cavity pointing countercurrent.

sloping cavity pointing in the flow direction (for a description of the measuring area see Fig. 5.8). The mean field is shown in Fig. 5.11 and streamlines for the mean field in Fig. 5.12. Also an example from the time serie showing the correlation intensity is given in Fig. 5.13. The poor resolution of the camera did not make it possible to capture more of the vortex. and thereby producing better "boundary conditions" for the streamlines, see Fig. 5.12. From the figure it can be seen that the streamlines show no flow into the cavity, and this is in contradiction to the visualisations in Fig. 5.2 and Fig. 5.3.

Figure 5.15 and Fig. 5.16 show two discrete time shots of the downstream wall for the sloping cavity pointing countercurrent (for description of the measured area see Fig. 5.14). The mean field is shown in Fig. 5.17 and streamlines for the mean field in Fig. 5.18. In this part the center of a small vortex as shown from the visualisation studies given in Fig. 5.4 and Fig. 5.5. The mean field in Fig. 5.17 shows that the center of the vortex is in the middle of the captured field.

The stagnation point shown in Fig. 5.4 and Fig. 5.5 is also detected by the PIV-system, as seen in Fig. 5.21 and Fig. 5.22. Here the downstream corner is captured (see Fig. 5.20 for description of the measured area). The downstream wall in this case covers a large area. This will influence on the velocities found near the surface. The interrogation areas in this part if the image have the wall covering half of their area, and this will influence on the result (the particle intensity will have to be very high near the surface to get enough particle pairs).

The correlation intensity for the three areas displayed is given in Fig. 5.13, Fig. 5.19 and Fig. 5.23. As seen from the figures the areas near surfaces may be very much influenced by the shape of the surface. The reflected light may be influenced by small shape differences in the surface. and the reflected light may not fill the pixels imaging the surface equally. This is clearly shown by Fig. 5.23. which show that the correlation intensity increase along the wall. The two other cases Fig. 5.13 and Fig. 5.19 show the same effect. In Fig. 5.13 the correlation peak is strong near the wall. This means that there is strong signal to noise ratio. The light reflected from the wall will in this case not be picked up by the sensor, and

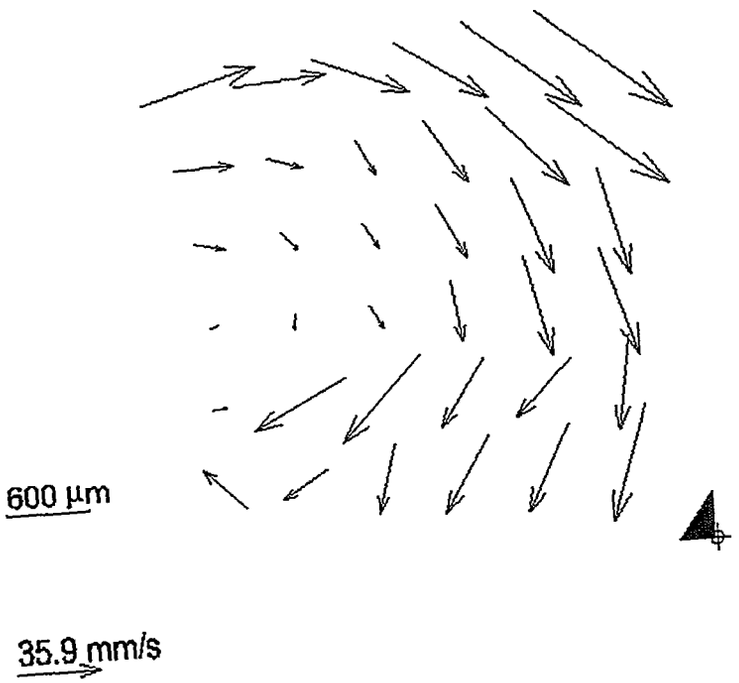

Figure 5.15: A PIV field taken in the cavity pointing countercurrent.

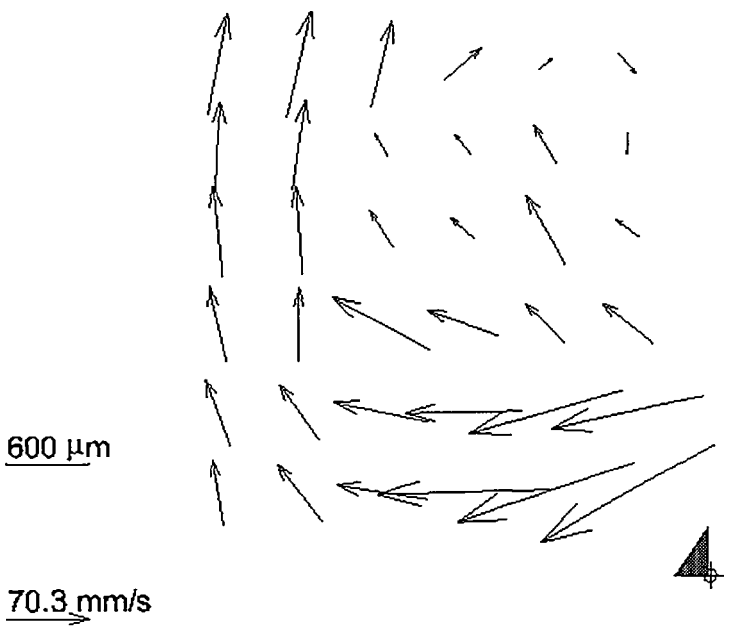

Figure 5.16: A PIV field taken in the cavity pointing countercurrent.

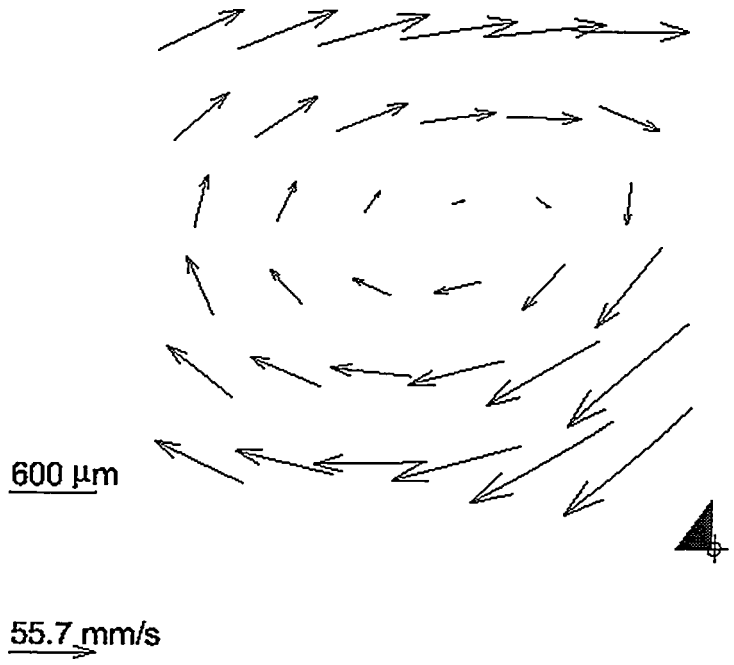

Figure 5.17: The PIV mean field in the cavity pointing countercurrent.

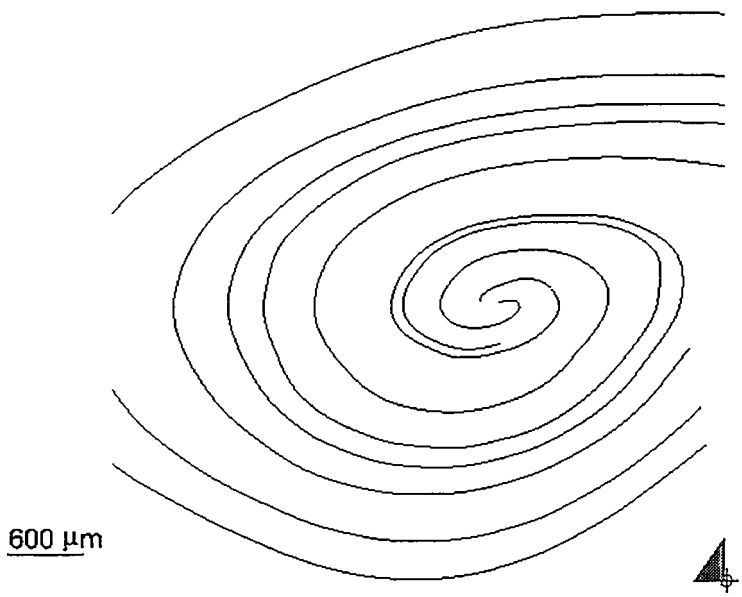

Figure 5.18: The PIV streamlines in the cavity pointing countercurrent.

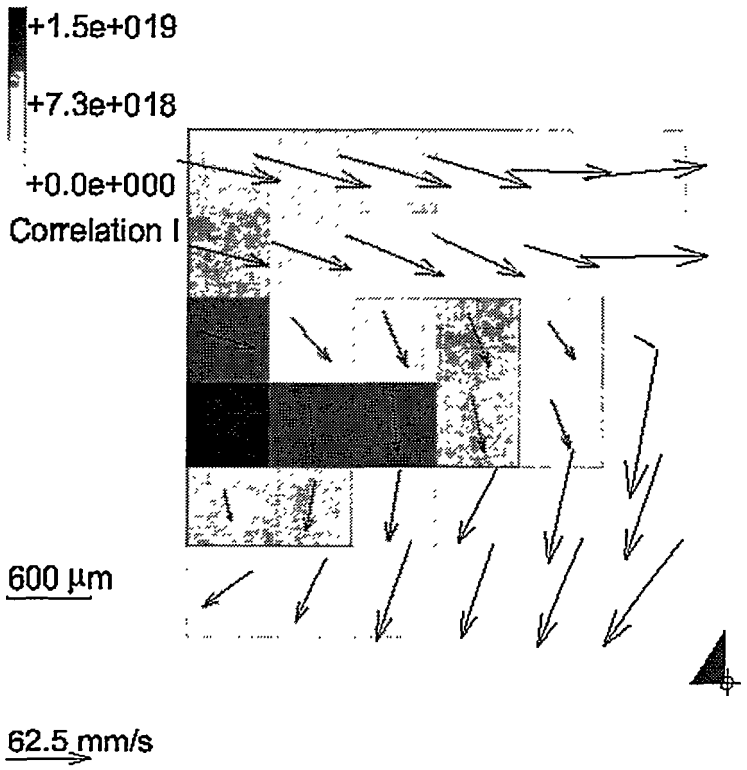

Figure 5.19: The PIV correlation field in the cavity pointing countercurrent.

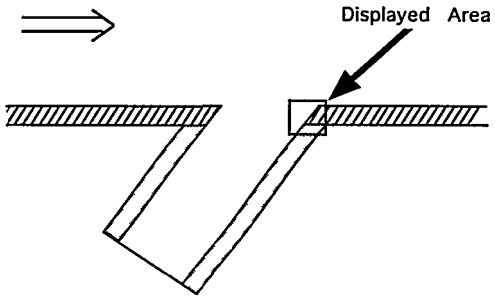

Figure 5.20: The measured area in the cavity pointing countercurrent at the downstream corner.

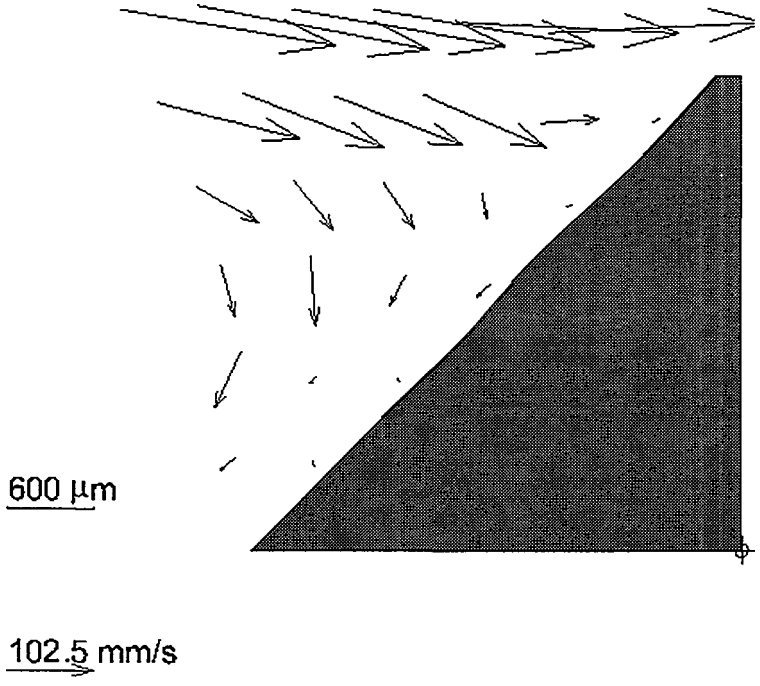

Figure 5.21: The PIV mean field in the cavity pointing countercurrent at the downstream corner.

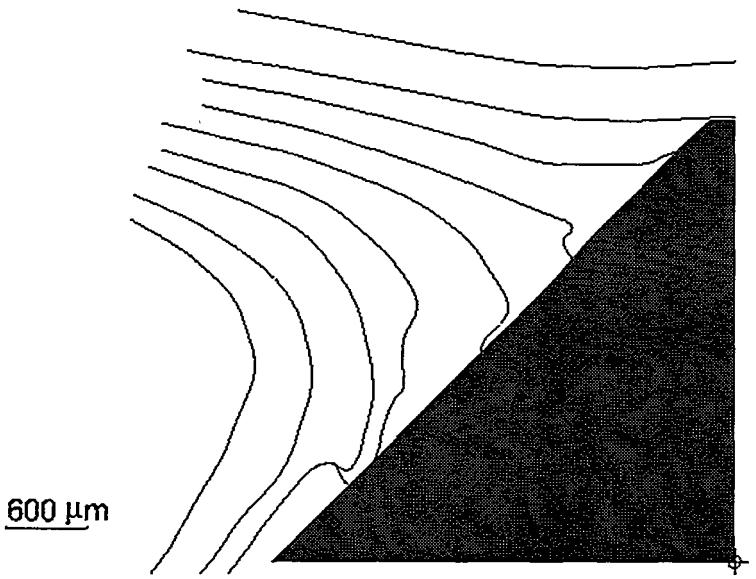

Figure 5.22: The PIV streamlines in the cavity pointing countercurrent at the downstream corner. Note the stagnation point indicated by the streamlines.

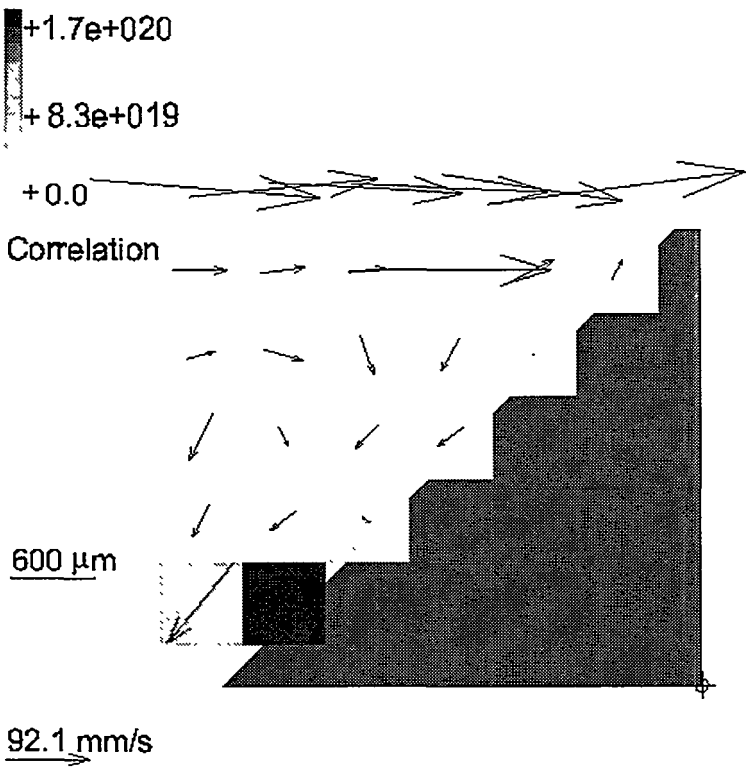

Figure 5.23: The PIV correlation field in the cavity pointing countercurrent at the downstream corner.

produce noise in the interrogation area. In other words the detection of the velocity in this case is good. The opposite is true in Fig. 5.19. The correlation peak is weak, which means that there is a low signal to noise ratio. There is a stronger uncertainty in the velocity in this case.

The correlation intensity field may be used to see how well the PIV-system has measured the velocities near surfaces. It may be concluded that the reflected light from a wall may be very difficult to control, and that the results found in this area may be influenced by the wall.

Chapter 6

LDV measurements

In this chapter, LDV measurements of the boundary layer entering the cavity and the flow inside the cavity will be presented.

6.1 The boundary layer flow

The flow entering the cavity is a wall bounded flow, see Fig. 6.1 for a description of a model in the water tunnel.

The test section of the tunnel is a 1 m long channel of 140 mm square section. The cavity model is a 12 mm thick plexiglas plate placed in the middle of the test section, dividing the test section into two halves, 70 mm on the cavity topside and 58 mm on the cavity backside, see Fig. 6.1. This means that the geometry defining the flow entering the cavity is given as a rectangular channel of 70 mm×140 mm.

The flow on the plexiglas plate will be a wall bounded flow, a boundary layer flow. We assume that this is a 2-dimensional stationary flow, i.e. a flow where $W = 0$ and the spanwise derivative vanishes, $\frac{\partial}{\partial z} = 0$. The set of equations valid for this case is

$$\frac{\partial U}{\partial x} + \frac{\partial V}{\partial y} = 0 \tag{6.1}$$

and

$$U\frac{\partial U}{\partial x} + V\frac{\partial U}{\partial y} = -\frac{1}{\rho}\frac{\partial P_e}{\partial x} + \frac{1}{\rho}\frac{\partial}{\partial y}(\mu\frac{\partial U}{\partial y} - \rho\overline{uv}) \tag{6.2}$$

In these equations Reynolds averaging and boundary layer assumptions have been applied, see e.g. Hinze (1975). The boundary layer assumption means that the characteristic length scale in the streamwise direction is much greater and changes much slower than for the direction normal to the wall (Hinze 1975).

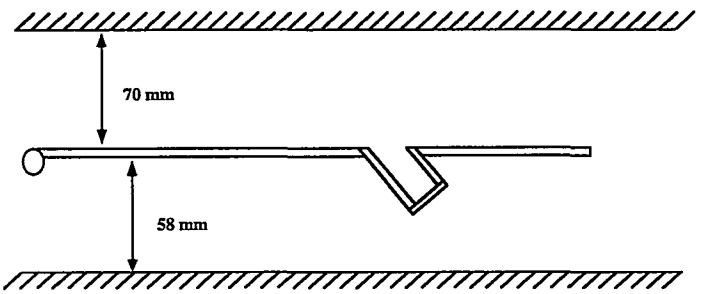

Figure 6.1: A sketch of a model in the water tunnel

Outside the boundary layer these equations may be reduced to

$$V = \int_0^Y \frac{dU}{dx} dy \tag{6.3}$$

and

$$U_e \frac{dU_e}{dx} = -\frac{1}{\rho} \frac{dP_e}{dx} \tag{6.4}$$

where U_e is the velocity in the free unbounded flow.

Townsend (1956) suggested a characteristic scale for the velocity, given as

$$u_\tau = \sqrt{\frac{\tau_w}{\rho}} = U_e \sqrt{\frac{C_f}{2}} \tag{6.5}$$

where τ_w is the wall shear stress, C_f is the skin friction coefficient and ρ is the density of the fluid. u_τ is normally named the friction velocity.

The length scale was chosen to be the boundary layer thickness, δ, which normally is given as

$$\frac{U(y=\delta)}{U_e} = 0.99 \text{ or } 0.995 \tag{6.6}$$

A boundary layer velocity profile can be divided into three different regions

- Inner layer, where viscous shear dominates
- Outer layer, where turbulent shear dominates
- The overlap layer, where both viscous and turbulent shear are present

In 1979 Musker suggested a law that works for all the different parts of the boundary layer. This is an explicit expression given as

$$\begin{aligned} U^+ &= 5.424 \cdot tan^{-1}\left(\frac{2y^+ - \alpha'}{16.}\right) \\ &+ \log_{10}\left[\frac{(y^+ + 10.6)^{9.6}}{(y^{+2} - 8.15y^+ + 86)^2}\right] \\ &- \gamma' \\ &+ \frac{1}{\kappa}\left[(1 + 6\Pi)\left(\frac{y}{\delta}\right)^2 - (1 + 4\Pi)\left(\frac{y}{\delta}\right)^3\right] \end{aligned} \tag{6.7}$$

Musker used Granwille (1976) suggestion for fulfilling the outer boundary layer conditions. Therefore this law is called the Musker-Granwille's law.

Π given in Eq. 6.7 is Coles wake parameter (see e.g. Skåre 1994). It is determined as the maximum deviation from the log law as shown in Fig. 6.2.

By choosing $\alpha' = 8.75$ and $\gamma' = 3.31$ in Eq. 6.7, the log law is given with $B = 5.2$. Originally $\alpha' = 8.15$ and $\gamma' = 3.52$ and this gives $B = 4.96$ for the log law, see e.g. Skåre (1994).

A boundary layer that fulfills the conditions

$$\frac{\partial \delta}{\partial x} = \text{const.} \quad C_f = \text{const.} \quad \beta = \frac{\delta^*}{\tau_w}\frac{dP_e}{dx} = \text{const.} \tag{6.8}$$

is called an equilibrium boundary layer. β is called Clauser's equilibrium parameter (page 416 White (1991)). δ^* in Clauser's equilibrium parameter is called the displacement thickness and is given by

$$\delta^* = \int_0^\infty (1 - \frac{U}{U_e})dy \cong \int_0^\delta (1 - \frac{U}{U_e})dy \tag{6.9}$$

Clauser also defined another parameter, G. G is called Clauser's shape parameter and it remains constant in the streamwise direction for equilibrium boundary layers. G is given

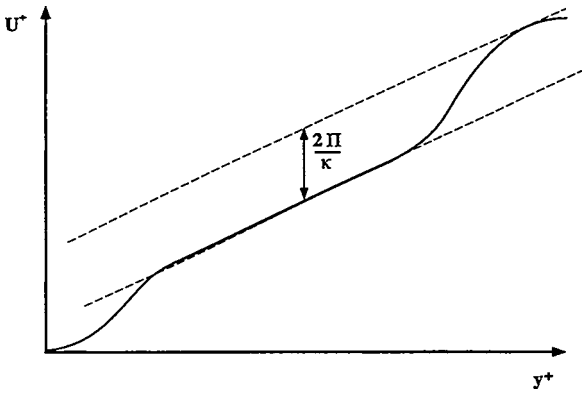

Figure 6.2: Coles wake parameter

as

$$G = \frac{\int_0^\infty (\frac{U_e - U}{u_\tau})^2 dy}{\int_0^\infty (\frac{U_e - U}{u_\tau}) dy} \cong \frac{\int_0^\delta (\frac{U_e - U}{u_\tau})^2 dy}{\int_0^\delta (\frac{U_e - U}{u_\tau}) dy} = \frac{H-1}{H}\sqrt{\frac{2}{C_f}} \tag{6.10}$$

In Eq. 6.10 it is seen that the ordinary Von Kárman shape parameter H can be related to the Clauser shape parameter G. H is given by the displacement thickness δ^* and the momentum thickness θ as

$$H = \frac{\delta^*}{\theta} \tag{6.11}$$

where

$$\theta = \int_0^\infty \frac{U}{U_e}(1 - \frac{U}{U_e})dy \cong \int_0^\delta \frac{U}{U_e}(1 - \frac{U}{U_e})dy \tag{6.12}$$

In boundary layer analysis a commonly used parameter is Re_θ, defined as

$$Re_\theta = \frac{U\theta}{\nu} \tag{6.13}$$

A boundary layer with $Re_\theta < 6000$ is called a low-Reynolds-number turbulent boundary layer (Erm and Joubert 1991).

In the present case the boundary layer coordinate system is defined as x in the streamwise direction, y normal to the plate and z parallel to the plate and normal to the stream direction. The origin is at the beginning of the plate, see Fig. 6.3.

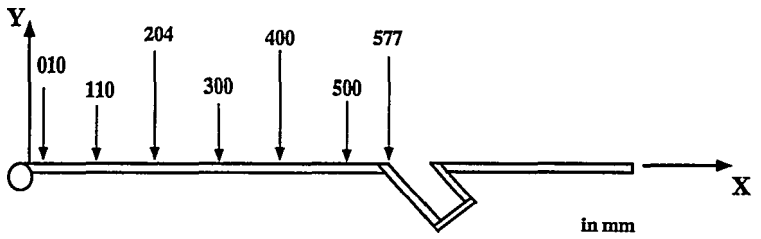

Figure 6.3: The coordinate system in this case

To investigate the incoming boundary layer a TSI Laser Doppler Velocimetry, LDV, system was used. Velocity profiles were measured at seven positions from the start of the plate and downstream to the beginning of the cavity, see Fig. 6.3. The profiles were measured along the plate center line. At the front of the cavity three profiles were measured in the z-direction to verify that the incoming boundary layer was 2-dimensional.

The measured mean velocity profiles in the streamwise direction are given in Fig. 6.4. The figure shows the development of the velocity along the plate.

The measured mean profiles at the front of the cavity are given in Fig. 6.5. As the figure shows, there is no clear difference in the mean velocity of these profiles. Also the turbulence intensity given in Fig. 6.6 show good 2-dimensionality.

As shown in Fig. 6.4 there is a development in the boundary layer. The four last positions $x = 204\,\text{mm}$, $x = 300\,\text{mm}$, $x = 400\,\text{mm}$ and $x = 500\,\text{mm}$ were used to find how well developed the boundary layer was. They were reduced using an inhouse-made software (Skåre 1994). It was used to find u_τ and thereby u^+ and y^+ for the measurements. They were compared to the Musker-Granwille's boundary layer law, see Fig. 6.7 for results.

In these profiles $\kappa = 0.41$ and $B = 5.2$. The same constants were used by Skåre (1994) and Erm and Joubert (1991).

At $x = 204\,\text{mm}$, $x = 300\,\text{mm}$ and $x = 400\,\text{mm}$ there are scatter in 3 or 4 points near the surface. This can be seen both in Fig. 6.4 and Fig. 6.7. Small scratches on the test section window will turn the laser beam and thereby move the measuring volume. The traverse mechanism used did have small irregularities at some places in the traversing direction. These two effects will lead to scatter in the mean velocity profile as shown in the two figures.

The cavity boundary layer was compared to Erm and Joubert zero pressure gradient boundary layer measurements. The mean velocity given as outer variables, or in the defect type is shown in Fig. 6.8 for $x = 500\,\text{mm}$.

As shown in the figure the LDV measurements of the cavity boundary layer have lower values than found by Erm and Joubert.

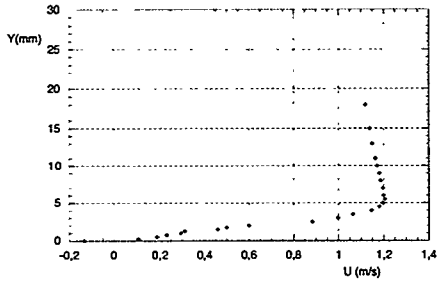

(a) $x = 0\,\text{mm}$

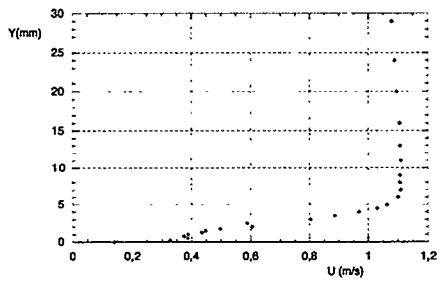

(b) $x = 10\,\text{mm}$

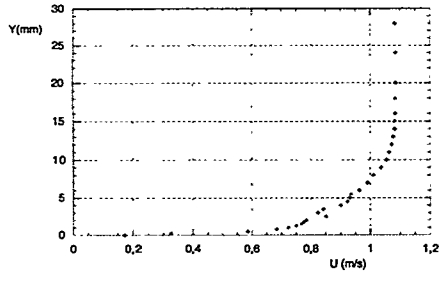

(c) $x = 110\,\text{mm}$

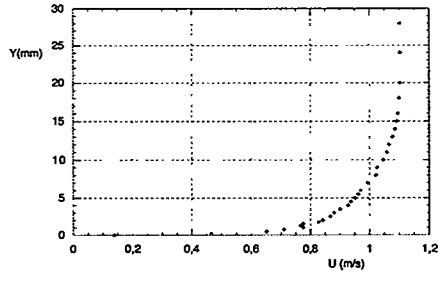

(d) $x = 204\,\text{mm}$

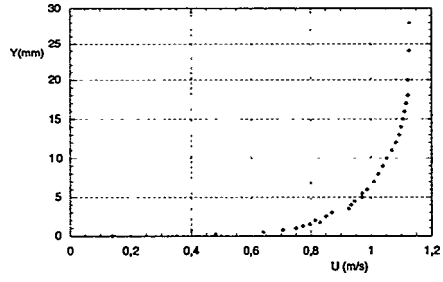

(e) $x = 300\,\text{mm}$

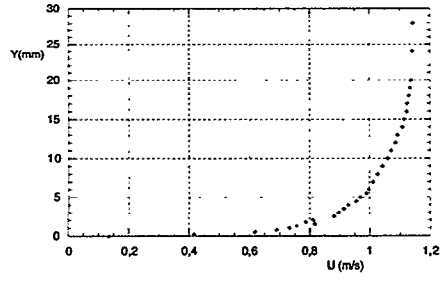

(f) $x = 400\,\text{mm}$

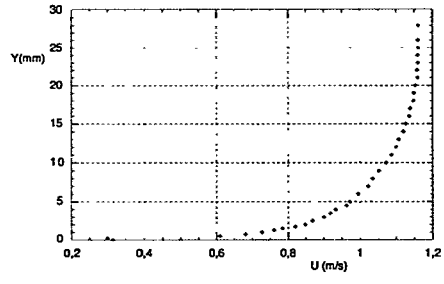

(g) $x = 500\,\text{mm}$

Figure 6.4: Mean velocity profiles along the plate

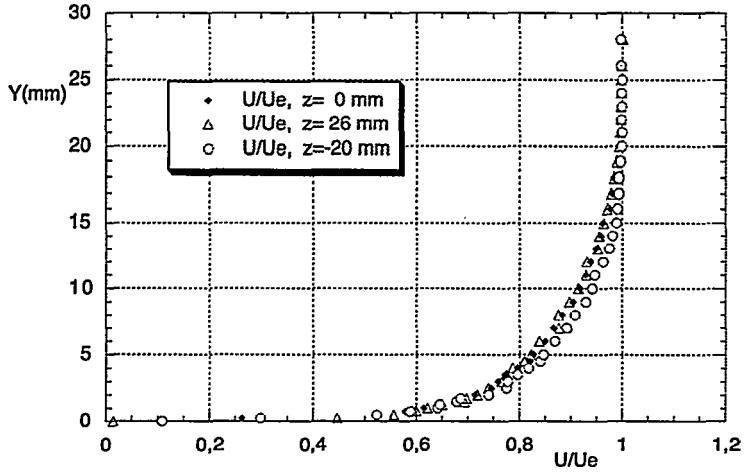

Figure 6.5: The mean velocity at the front of the cavity

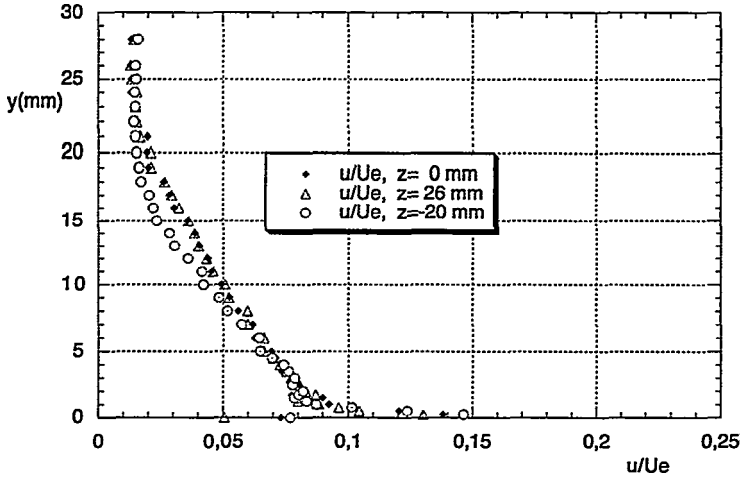

Figure 6.6: The turbulence intensity profile at the front of the cavity

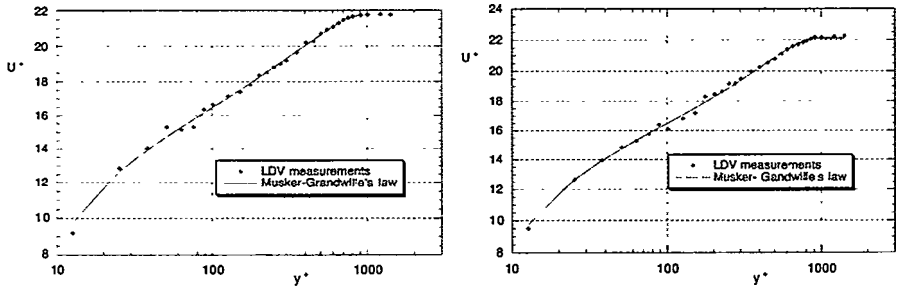

(a) $x = 204\,\text{mm}$ (b) $x = 300\,\text{mm}$

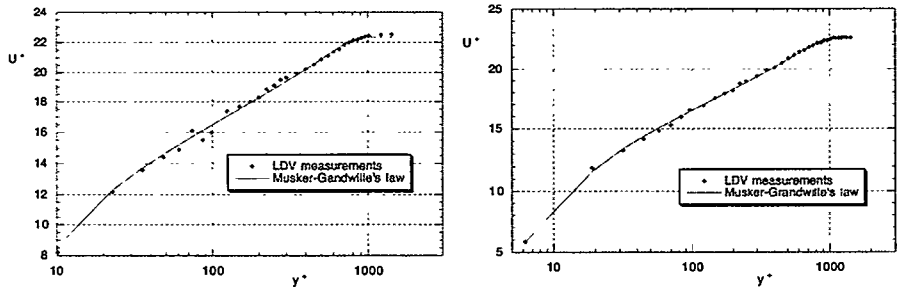

(c) $x = 400\,\text{mm}$ (d) $x = 500\,\text{mm}$

Figure 6.7: The four last mean velocity profiles in inner variables

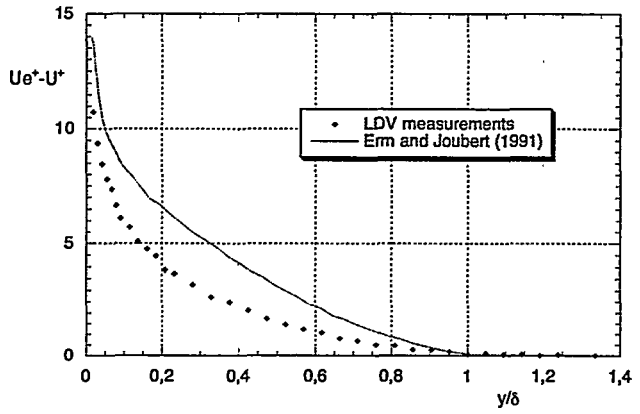

Figure 6.8: The mean velocity profile at $x = 500\,\text{mm}$ given in outer variables

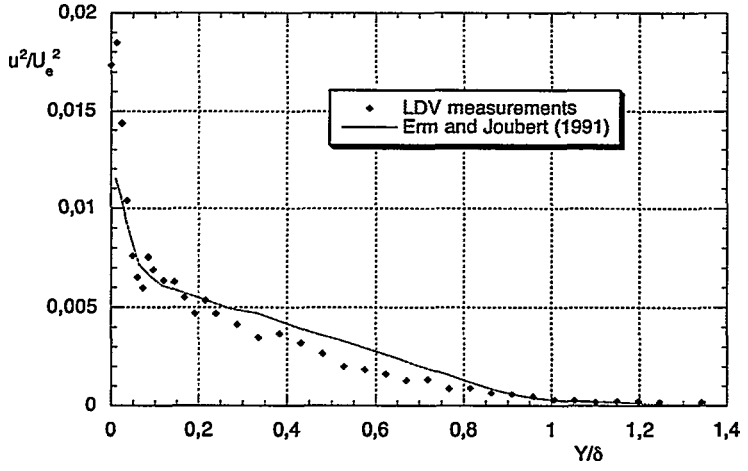

Figure 6.9: The normal stress profile at $x = 500\,\text{mm}$

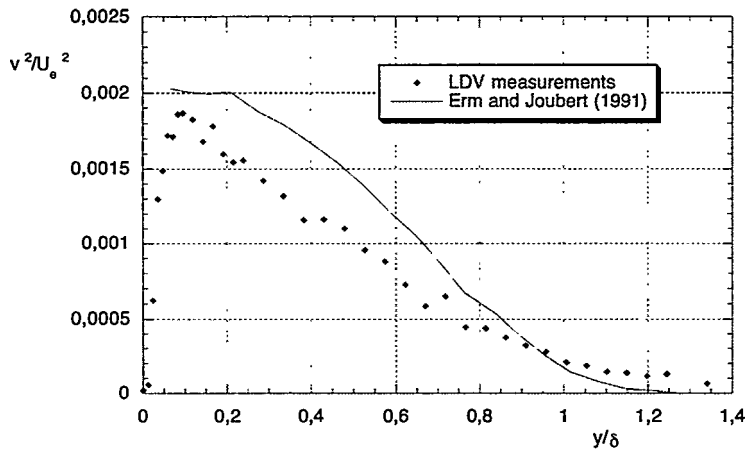

Figure 6.10: The normal stress profile at $x = 500\,\text{mm}$

Also the normal stress for u and v shown in Fig. 6.9 and Fig. 6.10 show somewhat lower levels than for zero pressure gradient boundary layer.

In Table 6.1 some parameters for the cavity boundary layer at $x = 500\,\text{mm}$ are given.

The parameter δ was found by

$$\frac{U(y=\delta)}{U_e} = 0.995 \tag{6.14}$$

Von Kármans shape factor, H, found from Erm and Joubert (1991) was $H = 1.42$ for $Re_\theta = 2226$. This means that the shape factor for the cavity boundary layer is somewhat too low compared to the zero pressure gradient boundary layer.

The parameter ΔU^+ given by Coles (see e.g. Sætran 1984) is $\Delta U^+ = 2.15$ for $Re_\theta = 2250$. This means that the wake strength Π is smaller than for the zero pressure gradient boundary layer (see Tab. 6.1). The relation between Π and ΔU^+ is given by Fig. 6.2.

The Clauser shape parameter, G, for zero pressure gradient boundary layer is $G \approx 6.6$, see eg. Skåre (1994). This means that this factor also is lower.

All these parameters G, ΔU^+ and H are lower than for zero pressure gradient boundary layer. The velocity defect $U_e^+ - U^+$ and the turbulence profiles also show a lower tendency than for zero pressure boundary layers. This indicate that a favourable pressure gradient can be present in the test section.

Clauser's equilibrium parameter also indicate that there is a favorable pressure gradient.

Table 6.1: The parameters from the boundary layer at $x = 500\,\text{mm}$.

Parameter	value
δ	20.88 mm
δ^*	2.36 mm
θ	1.76 mm
H	1.34
C_f	$3.91{\cdot}10^{-3}$
u_τ	0.052 m/s
G	5.64
ΔU^+	0.31
Re_θ	2050

Equation 6.15 was used to calculate β.

$$U_e \frac{dU_e}{dx} = -\frac{1}{\rho}\frac{dP_e}{dx} \tag{6.15}$$

This equation was normalized by using a reference velocity. The reference velocity, U_{ref}, was found by the pressure measurements over the contraction entering the test section, see Fig. 4.1. This gives

$$\frac{dP_e}{dx} = \rho U_e U_{\text{ref}} \frac{d}{dx}\left(\frac{U_e}{U_{\text{ref}}}\right) \tag{6.16}$$

Using Eq. 6.16 and $\tau_w = u_\tau^2 \rho$, this gives

$$\beta = \frac{\delta^*}{u_\tau^2} U_e U_{\text{ref}} \frac{d}{dx}\left(\frac{U_e}{U_{\text{ref}}}\right) = -0.17 \tag{6.17}$$

The parameter U_e/U_{ref} for varying x is shown in Fig. 6.11.

As seen in the figure there is a 15% increase in velocity per meter. A negative Clauser equilibrium parameter, $\beta = -0.17$, and an increase of 15% in the freestream velocity is a verification of an favorable pressure gradient. A constant value of β shows that this is an equilibrium flow (see page 416 White (1991)).

These results, indicating a favourable pressure gradient, were expected since the test section not was constructed to compensate for the boundary layer growth.

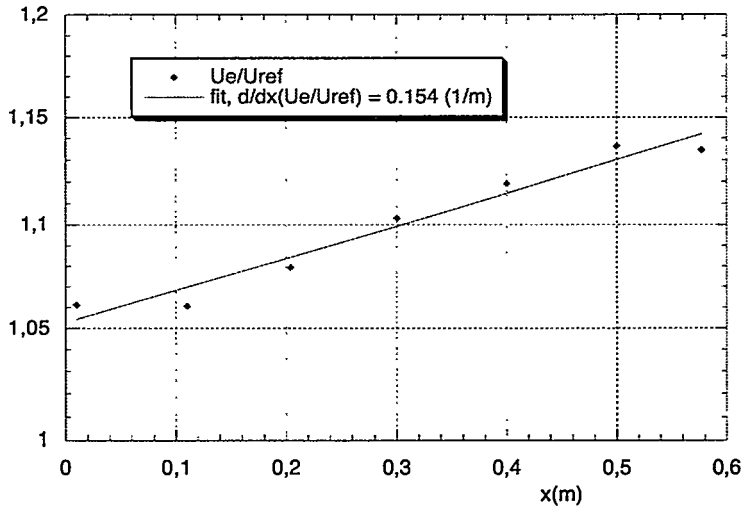

Figure 6.11: The normalized freestream velocity in the test section

6.1.1 Comparison of theoretical and measured development of momentum thickness for the cavity boundary layer flow

To verify the conditions of the incoming flow, the development of the momentum thickness was calculated along the plate. A method described by White (1991) was used. Von Kármans equation is given as

$$\frac{d\theta}{dx} + (2+H)\frac{\theta}{U_e}\frac{dU_e}{dx} = \frac{C_f}{2} \tag{6.18}$$

To close the equation White suggested to use four algebraic relations

$$\lambda = \frac{2 + 3.179\Pi + 1.5\Pi^2}{\kappa(1+\Pi)} \cdot \frac{H}{H-1} \tag{6.19}$$

where Π is Coles wake parameter and $\lambda = (2/C_f)^{1/2}$.

$$C_f \approx \frac{0.3 \cdot e^{-1.33H}}{(\log_{10} Re_\theta)^{1.74+0.31H}} \tag{6.20}$$

$$\beta \approx -0.4 + 0.76\Pi + 0.42\Pi^2 \tag{6.21}$$

$$\beta = \frac{\delta^*}{\tau_w}\frac{dP_e}{dx} = -\lambda^2 H \frac{\theta}{U_e}\frac{dU_e}{dx} \tag{6.22}$$

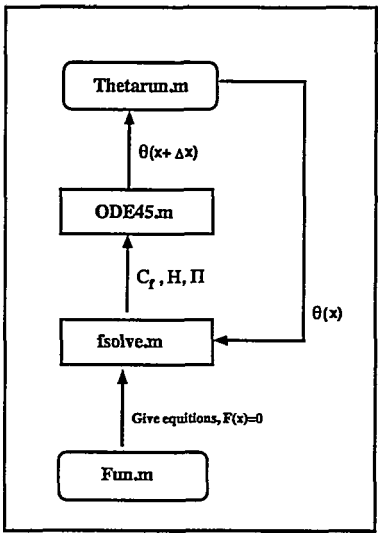

Figure 6.12: The solving structure for the development of θ.

These four algebraic relations are based on measurements performed by different researchers (see White 1991).

The procedure to solve the set of equations is as follows. At each step in the streamwise direction the set of algebraic relations are solved to find C_f, H and Π for a given θ. Then the differential equation is solved using a method like Runge Kutta to find θ at the next x-position (in the streamwise direction).

The algorithms doing these calculations were written in Matlab using standard routines in Matlab for solving differential equations and algebraic relations.

A block diagram showing the solution algorithm is given in Fig. 6.12

The development of θ found from the LDV measurements and calculations are shown in Fig. 6.13.

As shown in the figure the development of θ shows that there will not be a zero displacement at the start of the plate. As mentioned earlier, there is a cylinder at the front of the model. Exact solutions for a cylinder (see e.g. page 202 Schlichting (1968)) shows that θ at the front will be $\theta_{0^\circ} = 0.43\frac{R}{2}\sqrt{\frac{\nu}{U_\infty R}}$ and at the top of the cylinder $\theta_{90^\circ} = 0.71\frac{R}{2}\sqrt{\frac{\nu}{U_\infty R}}$, where R is the radius of the cylinder. In the present case this will give $\theta_{90^\circ} = 3.36{\cdot}10^{-5}$ mm. This value is too low compared to the start value used, $\theta_{\text{start}} = 1.15$ mm.

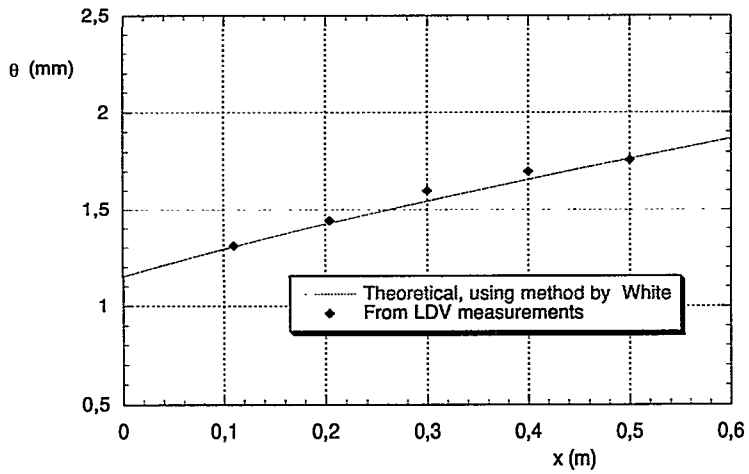

Figure 6.13: The development of θ in the test section.

Davis (1980) calculated three different leading edge configurations for flow over a flat plate at zero incidence. He found that for Reynolds number based on the thickness of the plate of 10^4 - $5{\cdot}10^4$ is the best for minimizing the adverse pressure gradient just after the leading edge. There is also a 14% blockage in the tunnel producing a velocity increase near the surface of the plate, as can be seen by Fig. 6.4. This velocity-increase will lead to a faster boundary layer growth than without the blockage.

Figure 6.14 shows the development of the turbulence intensity from the start of the plate. The figure show that there is a turbulent area near the surface even at $x = 0$. According to the theory $Re_x = \frac{U_\infty x}{\nu} \approx 10^5$ will give a transition from laminar to turbulent boundary layer along a flat plate of zero incidence. From Fig. 6.14 it can be seen that even before $Re_x = 10^5 \Rightarrow x = 10\,\text{cm}$ there is a near wall area with turbulence. The note by Davis shows that for different shapes of leading edges it can become turbulent at lower Re_x than 10^5.

6.2 LDV measurements in the cavity flow

The LDV system was used to measure velocity profiles at the front of the cavity, inside the cavity, at the downstream end and further downstream after the cavity. Three different geometries were used. These three geometries are shown in Fig. 5.1. The first two cavities are 2-dimensional models of ultrasonic flowmeter cavities, and the third is a rectangular cavity which is used to compare the measured results with results found by e.g. Sarohia (1977). Ethembabaoglu (1973) and Roshko (1955).

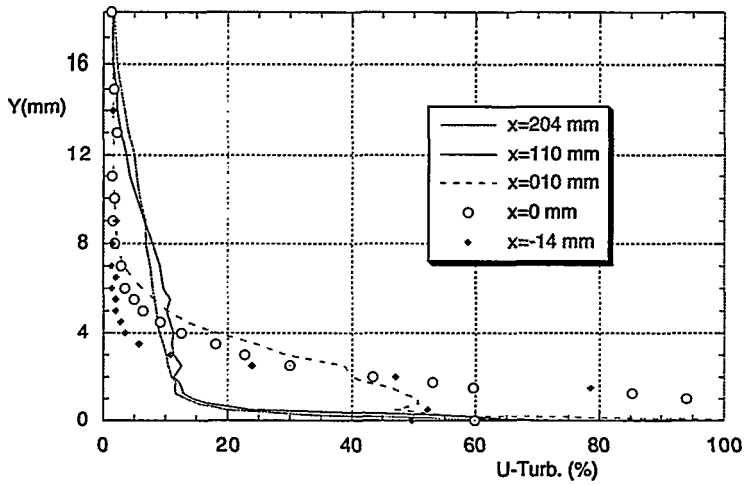

Figure 6.14: The development the turbulence intensity from the start of the plate

6.2.1 Sloping cavity pointed in the flow direction

In Fig. 6.15 the mean velocity profile at the front of the cavity is shown.

This profile gave $\theta = 1.85\,\text{mm}$. The momentum thickness at the front of the cavity was used as a reference thickness for the flow inside the cavity, and thereby named θ_{ref}. This means that θ_{ref} at the front of the cavity is used to normalize the profiles inside the cavity. The mean velocity profile normalized with θ_{ref} is given in Fig. 6.17, and in Fig. 6.18 the turbulence intensity is shown. To check the mean velocity profile with theory for boundary layer flow it was nondimesionalized using u_τ and ν and plotted in inner variables. From Fig. 6.16 it can be seen that the profile is in good agreement with the Musker-Gandwille law. The turbulence intensity profiles at the front of the cavity is given in Fig. 6.18.

Figure 6.20 and Fig. 6.21 show the mean velocity profile and turbulence intensity inside the cavity at $0.25W$ before the downstream corner. In Fig. 6.22 and Fig. 6.23 the same profiles are shown at $0.14W$ before the downstream corner. As seen from the figures there is a difference in the flow inside the cavity. At $0.25W$ the mean velocity profile show that there is a maximum in the backflow for this profile. At $0.14W$ the velocity is only positive. The visualisation studies in Chapter 5, confirms this effect. At this position there is no negative flow in U, only in V. The laser beams hit the wall at the downstream corner earlier for the measurements at $0.14W$, than for $0.25W$. This means that we were not able to measure as far down into the cavity at this position. There were also difficulties in finding the right position in the y-direction inside this cavity. The traversing mechanism did not have an exact scale, and this made it difficult to avoid an error in the positioning. To overcome this problem and place the laser beam crossing in the opening of the cavity,

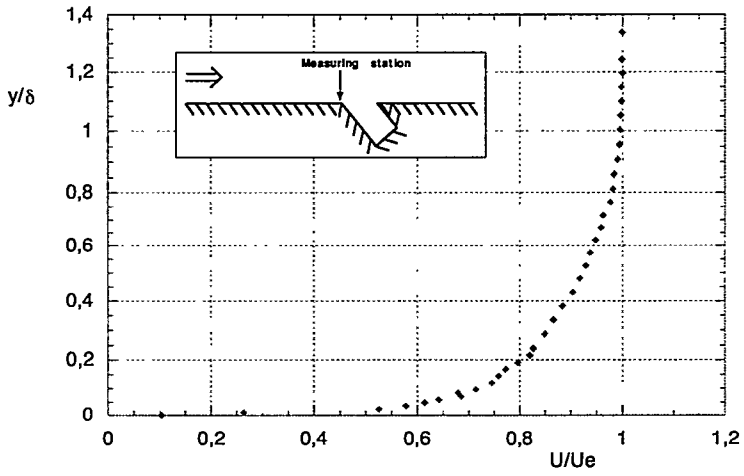

Figure 6.15: The mean velocity profiles at the front of the cavity

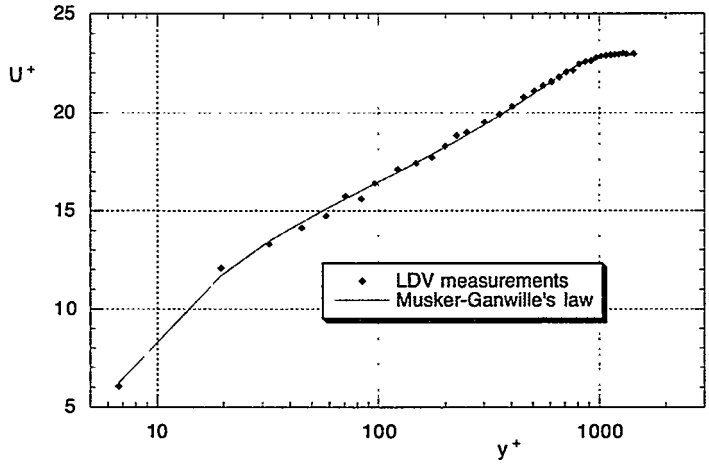

Figure 6.16: The mean velocity profile at the front of the cavity given in inner variables

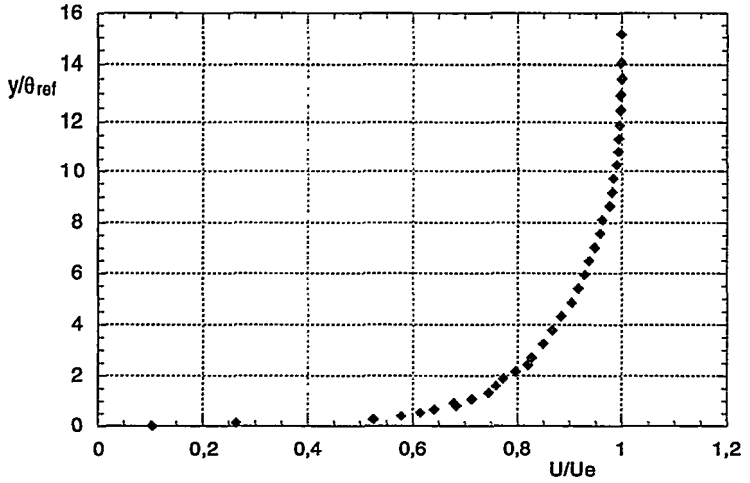

Figure 6.17: The mean velocity profile at the front of the cavity nondimesionalized with θ_{ref}

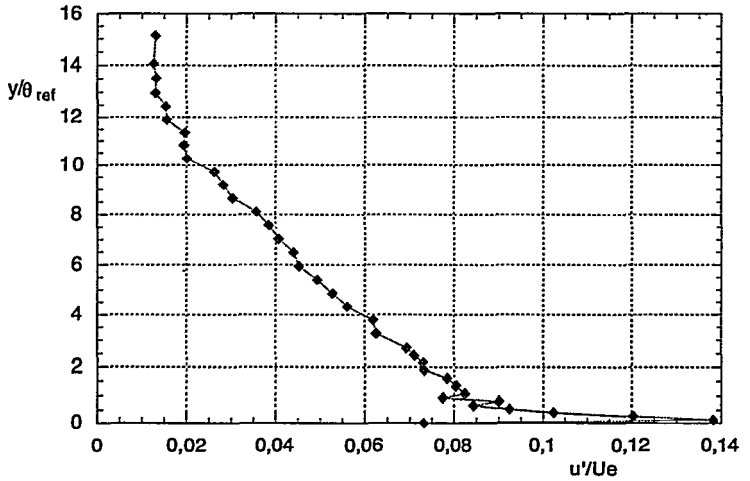

Figure 6.18: The turbulence intensity profile at the front of the cavity

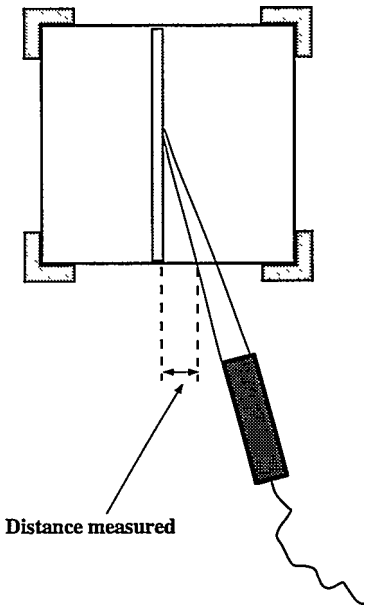

Figure 6.19: The method used to find the opening of the cavity when measuring with LDV.

the distance outside the tunnel from the cavity surface to the beam was measured, see Fig. 6.19.

Knowing the focal length of the LDV lens, and the distance outside the tunnel and the angle of attack, an estimate of the position of the measuring volume could be made. Uncertainty in the position was estimated to be 0.25 mm, or one fourth of a turn.

The cavity changed the conditions for the incoming boundary layer flow. This means that there has been some changes in the near-wall part of the velocity profiles. To verify that there were any changes, a Clauser representation of the mean velocity profiles at the downstream corner was used. The Clauser plot shows the velocity measurements against certain levels of the law of the wall, with a given C_f. If the boundary layer flow is not fully developed, C_f will not be constant. The results for the Clauser plot at 24 mm or $1.9W$ after the cavity shows that there is no clear description of C_f, see Fig. 6.24. In the figure the Van driest (van Driest 1956) law is used with $\kappa = 0.41$ and $A^+ = 26$, see Eq. 6.23. The results will therefore be presented using θ_{ref}, at $1.9W$ downstream after the cavity,

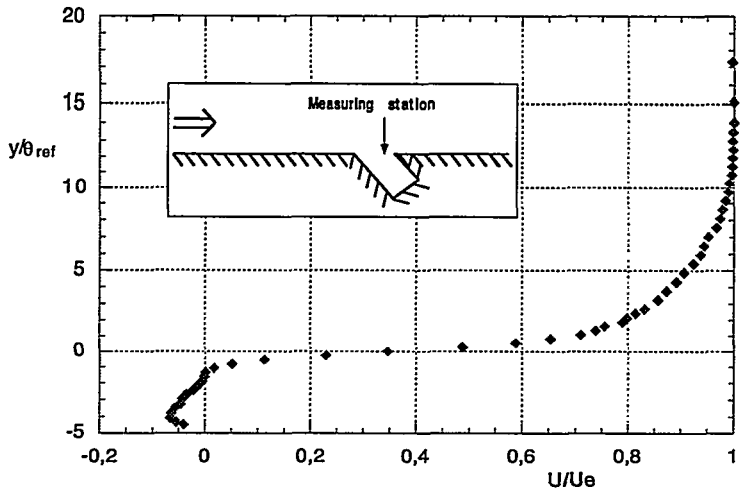

Figure 6.20: The mean velocity profile at $0.25W$ before the downstream corner

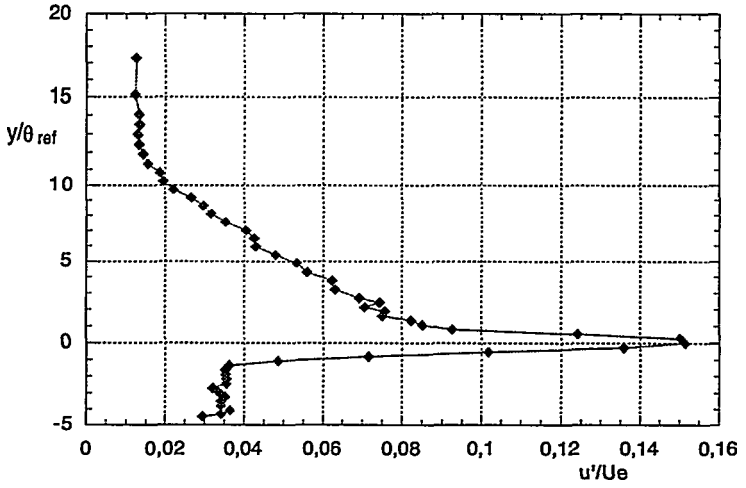

Figure 6.21: The turbulence intensity profile at $0.25W$ before the downstream corner

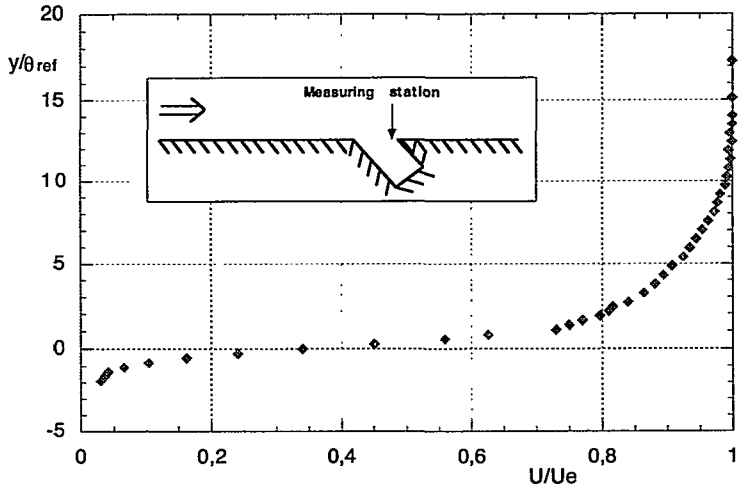

Figure 6.22: The mean velocity profile at $0.14W$ before the downstream corner

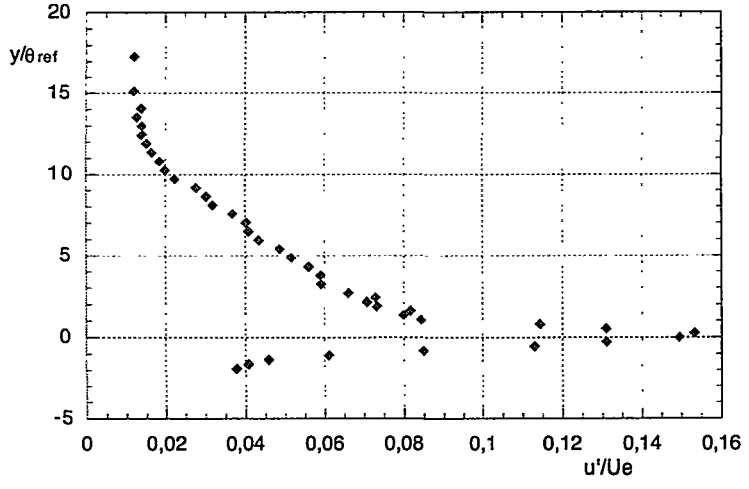

Figure 6.23: The turbulence intensity profile at $0.14W$ before the downstream corner

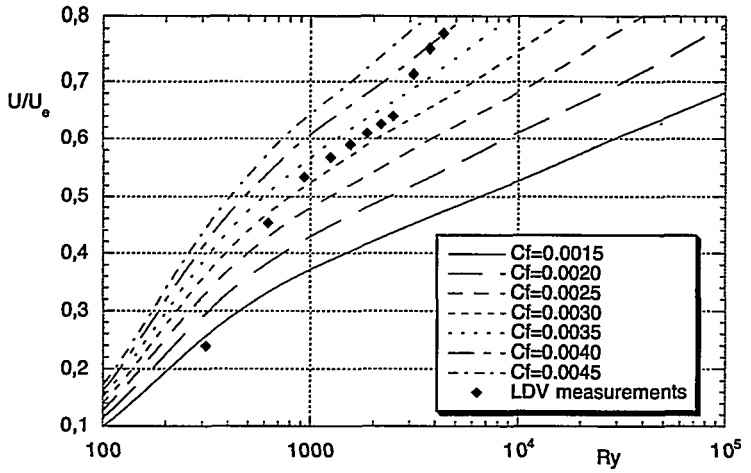

Figure 6.24: Clauser plot of $1.9W$ downstream after the cavity

see Fig. 6.25 and Fig. 6.26.

$$U^+ = \int_0^{Y^+} \frac{2}{1+\sqrt{1+(2\kappa y^+)^2[1-e^{-\frac{y^+}{A^+}}]^2}} dy^+ \tag{6.23}$$

The mean velocity profile at $1.9W$ (see Fig. 6.25) shows that a new boundary layer have started to grow near the wall. This can be confirmed by Fig. 6.26 which shows that the turbulence intensity has a peak at the same position as the interaction between the "new" and "old" boundary layer given by the mean profile in Fig. 6.25. These measurements were taken by using random correlation of data. This was done to ensure a high data rate.

6.2.2 Sloping cavity pointing countercurrent

As for the sloping cavity pointing in the flow direction, the mean velocity and turbulence intensity entering the sloping cavity pointing countercurrent were found, given in Fig. 6.27.

And also in this case the mean velocity profile at the front of the cavity was used to find $\theta_{ref} = 1.77\,\text{mm}$. As seen from the figure the incoming flow follow the Musker-Granwille's law. There is a small difference between θ_{ref} in this case and in the case of the cavity pointing in the flow direction (see chapter 6.2.1). The water tunnel use a valve to regulate the volume flow in the test section. It is difficult to get the exact same volume flow every time. For these measurements the LDV system was used to measure the freestream velocity at the cavity front at every startup.

Two profiles were also measured inside the cavity. At $0.25W$ from the upstream corner,

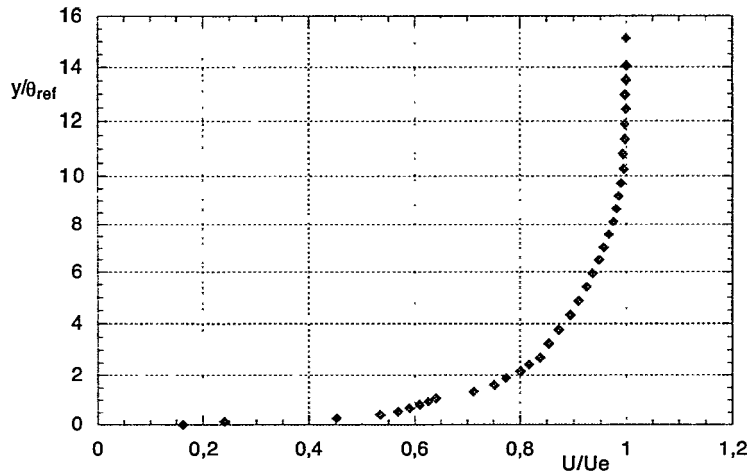

Figure 6.25: The mean velocity profile at $1.9W$ after the cavity

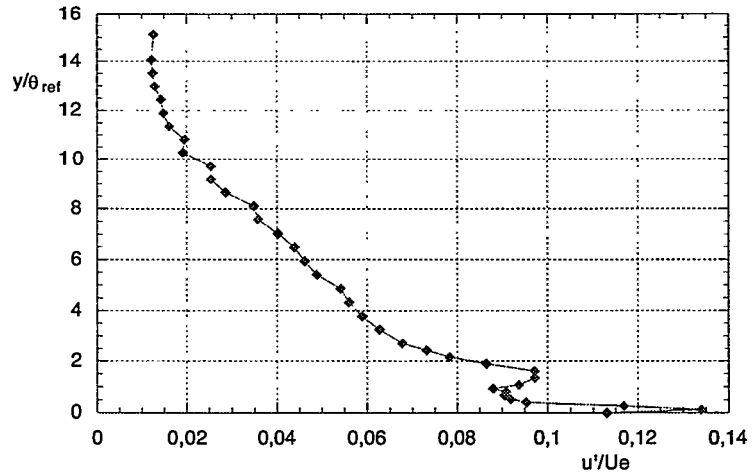

Figure 6.26: The turbulence intensity profile at $1.9W$ after the cavity

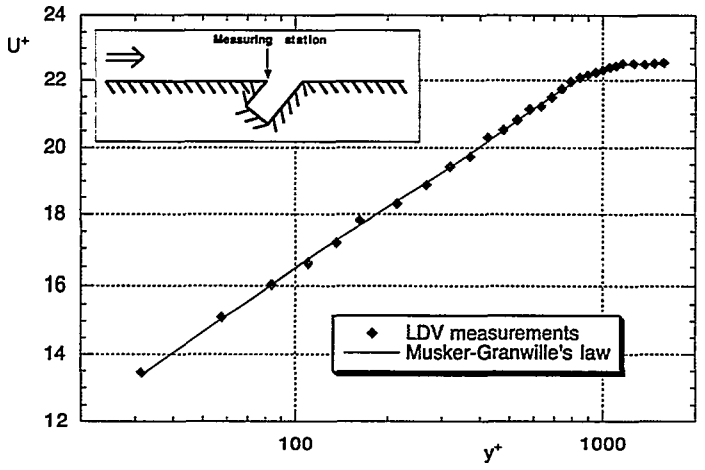

Figure 6.27: The mean velocity profile for the incoming flow given by inner variables

and $0.1W$ from the upstream corner. These results are given in Fig. 6.29 to Fig. 6.32.

The profile at $0.1W$ show that there is a gap between the flow inside the channel and cavity. This can also be seen by turbulence intensity in Fig. 6.30.

At $0.25W$ this gap is decreased, and there is an increase in the turbulence level at the cavity opening. If the mean velocity profiles in Fig. 6.29 and Fig. 6.31 are compared to Fig. 5.4 and Fig. 5.5, the reason for the velocities inside the cavity is visualized. At $0.1W$ the profile is measured through the upper parts of the vortex near the upstream corner. In this area the velocities will only be positive. The profile at $0.25W$ measures through the upstream parts of the vortex near the downstream corner. This is the reason for the negative velocities inside the cavity.

Also in this case the measurements downstream the cavity was plotted using a Clauser representation, Fig. 6.33. This shows that the mean velocity profile seems not to be affected by the cavity downstream corner in this case. The value of C_f from the Clauser plot is $C_f = 0.004$, and C_f at the front of the cavity is $C_f = 0.00394$. This means that the wall friction coefficient in this case is unaffected by the cavity. Figure 6.34 and Fig. 6.35 show the mean velocity profile and the turbulence intensity at the downstream corner. The mean velocity is in good agreement with Musker-Granwille's law. This confirms that in the case of the cavity pointing countercurrent, the mean velocity of the boundary layer is not affected by the cavity. At $1.5W$ downstream after the cavity the same result is found,

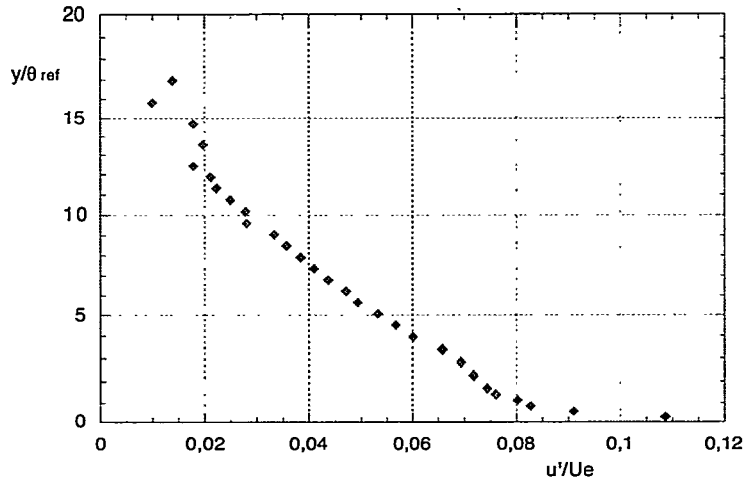

Figure 6.28: The turbulence intensity profile for the incoming flow normalized with θ

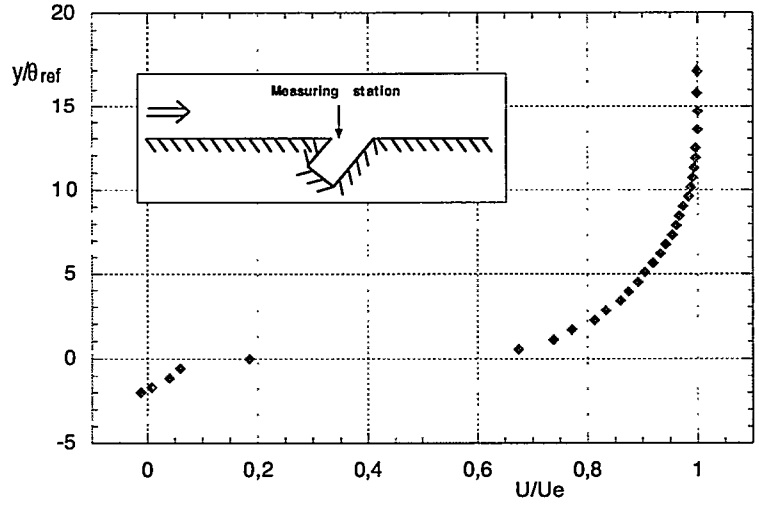

Figure 6.29: The mean velocity profile at $0.1W$ after the upstream corner

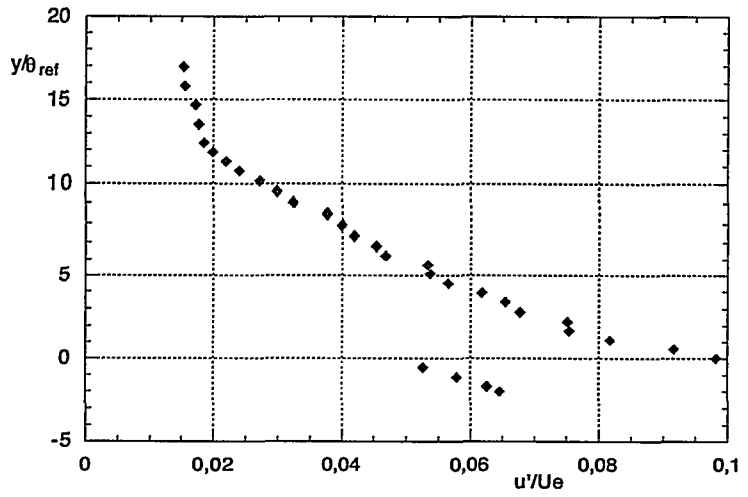

Figure 6.30: The turbulence intensity at $0.1W$ after the upstream corner

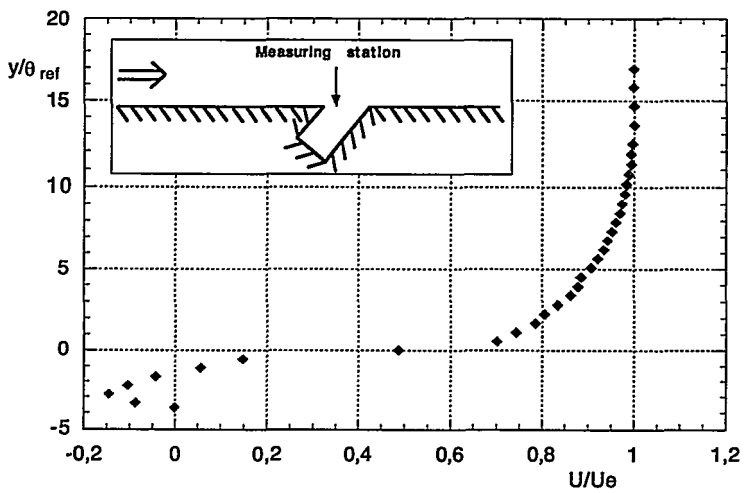

Figure 6.31: The mean velocity profile at $0.25W$ after the upstream corner

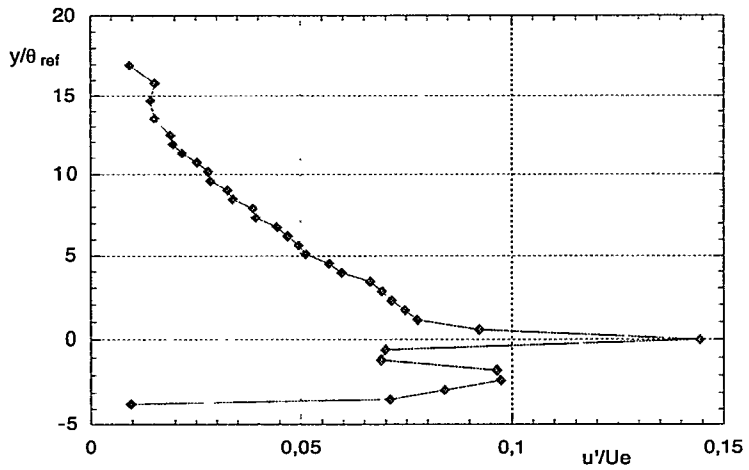

Figure 6.32: The turbulence intensity at $0.25W$ after the upstream corner

see Fig. 6.36.

If the turbulence intensity at the downstream corner (Fig. 6.35) is compared to the turbulence intensity of the incoming flow (Fig. 6.28), it is clear that the turbulence level near the wall has increased. Further downstream after the cavity (Fig. 6.37) the turbulence intensity near the surface has decreased, and the influence of the cavity downstream corner is almost no longer visible. This means that the turbulence level near the surface will be affected by the cavity downstream corner, but the effect will disappear shortly after the cavity.

Comparing the results found from the cavity pointing in the flow direction (chapter 6.2.1) and the cavity pointing countercurrent show that the shape of the downstream corner is important for the influence of the cavity upon the boundary layer. The same results are found by other researchers. The downstream corner shape is important for the flow over the cavity, see eg. Rockwell and Naudascher (1978).

6.2.3 The rectangular cavity

Also along with the sloping cavities, a rectangular cavity was set up and measured. This cavity was used mainly for comparison with earlier investigations, see Fig. 5.1. From his measurements Sarohia (1977) found a criterium for oscillations in a rectangular cavity to happen. For the cavity in Fig. 5.1 U_e has to be $U_e > 1.4\,\mathrm{m/s}$ to be able to produce oscillations. The freestream velocity was therefore set to $U_e = 1.8\,\mathrm{m/s}$.

The mean velocity profile and turbulence intensity for the front of the cavity is given in

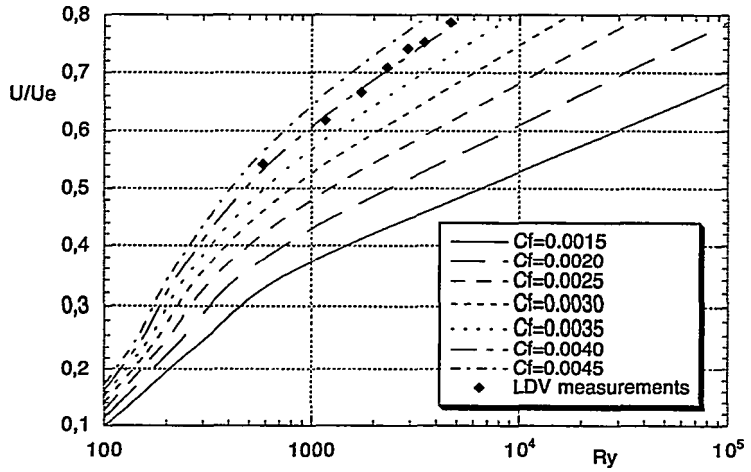

Figure 6.33: Clauser plot of the downstream corner for the cavity pointing countercurrent.

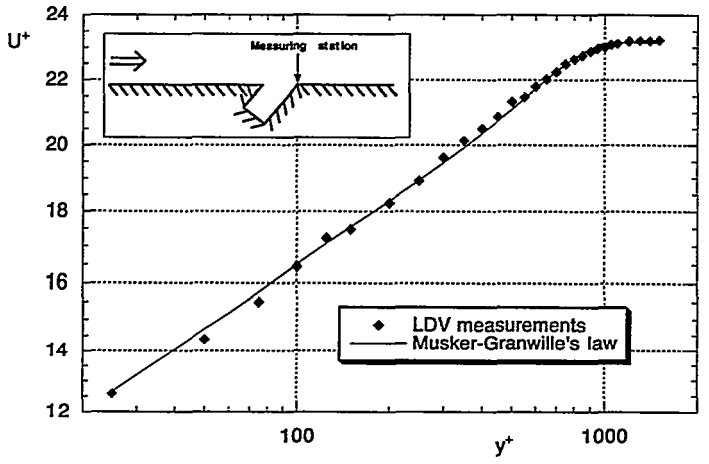

Figure 6.34: The mean velocity profile in inner variables at the down stream corner

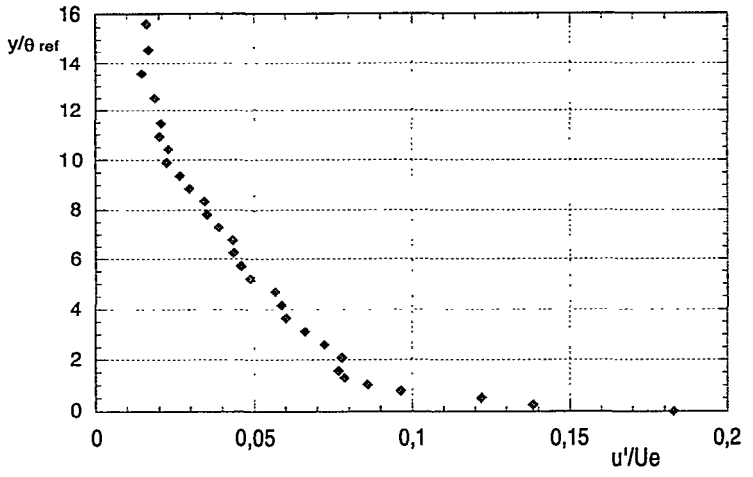

Figure 6.35: The turbulence intensity profile at the downstream corner

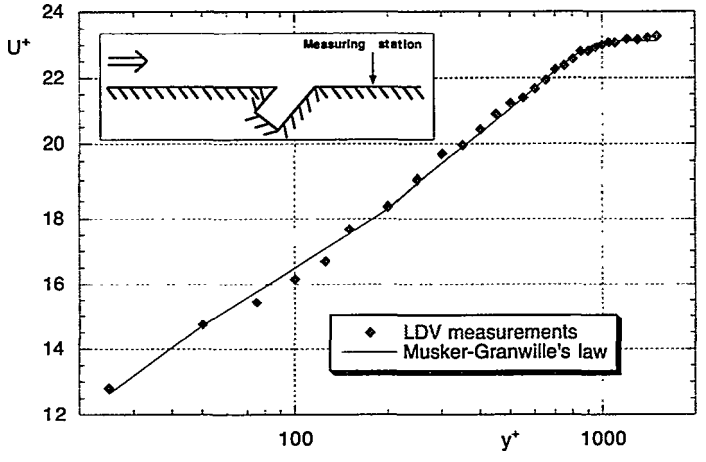

Figure 6.36: The mean velocity profile in inner variables at $1.5W$ after the cavity

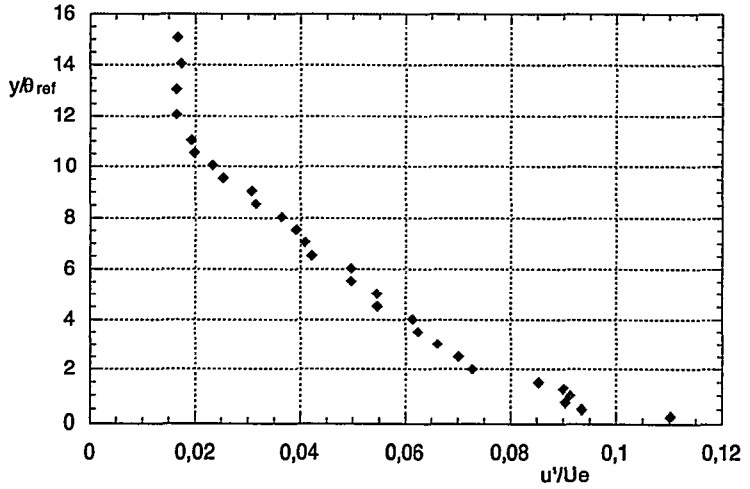

Figure 6.37: The turbulence intensity profile at $1.5W$ after the cavity

Fig. 6.38 and Fig. 6.39. As seen the profile also in this case show good agreement with the Musker-Granwille's law.

As seen from Fig. 6.38 the wake strength in this case is stronger than for the other two cases. In Fig. 6.40 the profiles are reduced with outer variables. As seen from the figure the profile for $U_e = 1.82\,\mathrm{m/s}$ shows much better correspondence with the results from Erm and Joubert (1991). This means that in the case of $U_e = 1.82\,\mathrm{m/s}$ the favorable pressure gradient has decreased, and in this case is more like a zero pressure gradient boundary layer flow.

As for the other cases the displacement thickness θ_{ref} given by the velocity profile at the front of the cavity is used to normalize the profiles inside the cavity.

In Fig. 6.41 and Fig. 6.42 the mean velocity profile and turbulence intensity at $0.25W$ before the downstream corner is given. Figure 6.43 and Fig. 6.44 show the mean velocity and turbulence intensity at $0.1W$ before the downstream corner.

Seen from both the profiles at $0.25W$ and $0.1W$ before the downstream corner, there are two points that fall outside the others. This is because of problems with the traverse. In the case of the rectangular cavity another part of the traverse was used than in the case of the sloping cavities. It was not possible to measure the diffraction, but it was clear that in some parts of the traverse the probe could be turned. In the rest of the investigation these two points are not used.

Figure 6.41 and Fig. 6.43 show that inside the cavity the two profiles are equal. This means that the vortex in this case has to be stretched in the flow direction, and that the downstream end of the vortex has to be very close to the downstream wall. This effect is

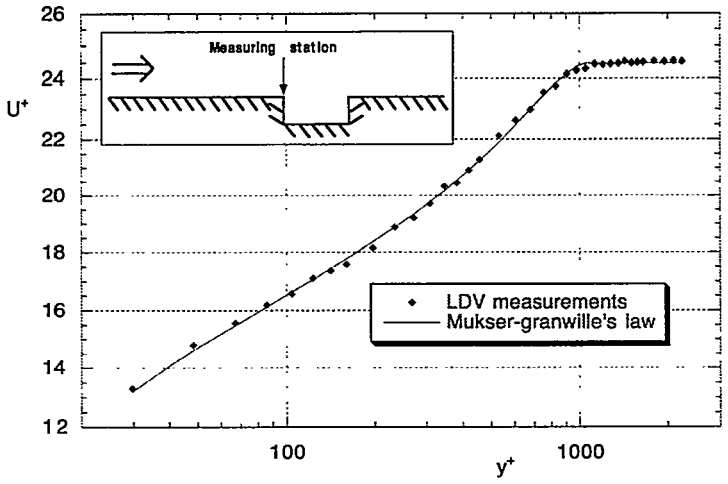

Figure 6.38: The mean velocity profile at the front plotted in inner variables

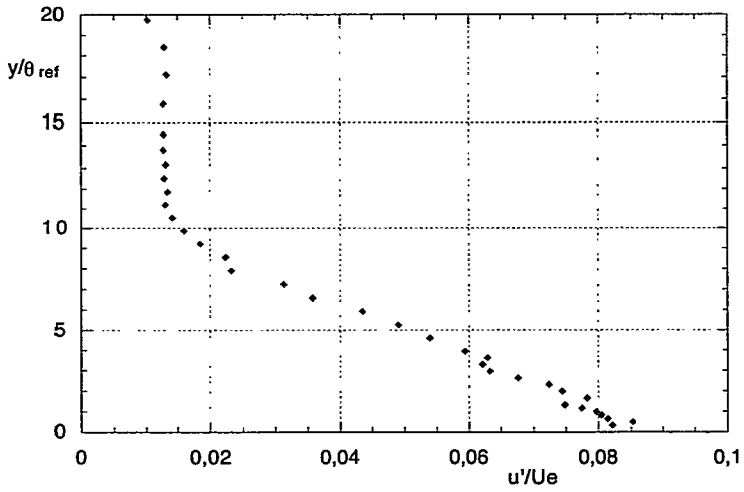

Figure 6.39: The turbulence intensity profile at the front

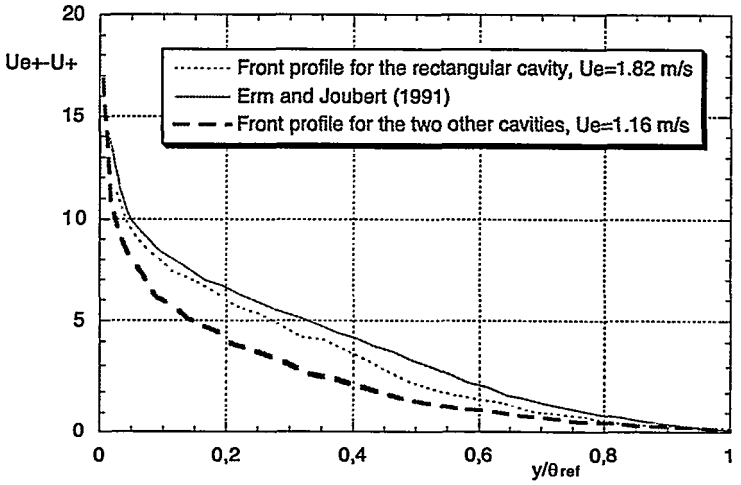

Figure 6.40: The front profiles given in outer variables

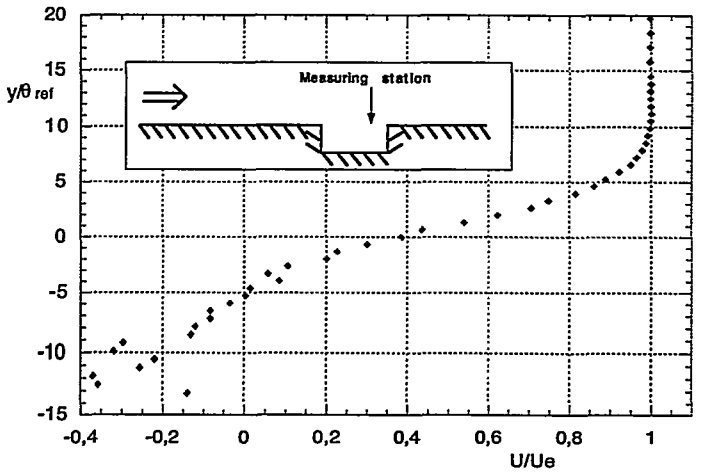

Figure 6.41: The mean velocity profile at $0.25W$ before the downstream corner

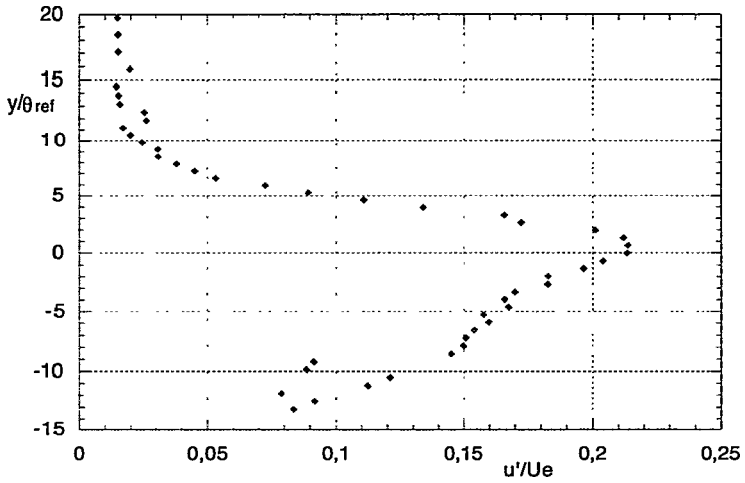

Figure 6.42: The turbulence intensity at $0.25W$ before the downstream corner

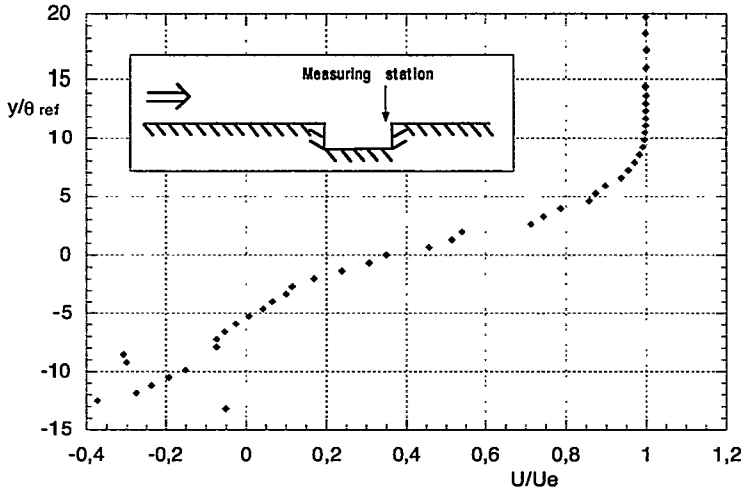

Figure 6.43: The mean velocity profile at $0.1W$ before the downstream corner

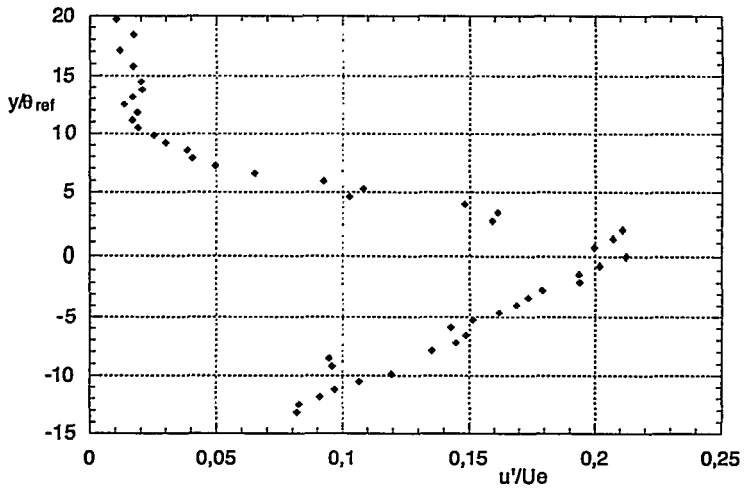

Figure 6.44: The turbulence intensity at $0.1W$ before the downstream corner

confirmed if the result is compared to the visualisations in Fig. 5.6 and Fig. 5.7. As seen from the visualisations, the vortex is stretched in the flow direction, and has a sharp turn near the downstream corner. The visualisations show that there is a stagnation point on the upper part of the downstream wall. This means that the inner parts of the boundary layer flows into the cavity (the same effect is described by Roshko (1955)). This effect can be seen as a jump in the velocity at $y/\theta = 2$ in Fig. 6.43.

Since the stagnation point is inside the cavity, the downstream corner will lead to a "clipping" of the boundary layer. The Clauser representation in Fig. 6.45 show that there is no clear description of C_f. This means that the boundary layer in this case is destroyed by the cavity.

The main purpose of this geometry was to see if we could find any oscillations, and if so how they compared with the results of eg. Sarohia (1977) and East (1966). The TSI FIND software was used to postprocess the LDV measurements. In these measurements `Random`-sampling and `TBD_ON` (time between data given) was used, see the TSI (1993) for more information about the theory for producing powerspectra from random signals.

In the present study no oscillations could be found from the LDV measurements. Extensive investigation of powerspectra around the downstream corner were performed, but no conclusion of oscillations in the flow could be done.

Sarohia (1977) did use two constant temperature hotwire probes, and correlated the two time series to find the oscillations. In the present study only one point measurements were done. Both the energy level and the frequency of the oscillations should be visible in the powerspectra from the present LDV measurements. Although several positions near the

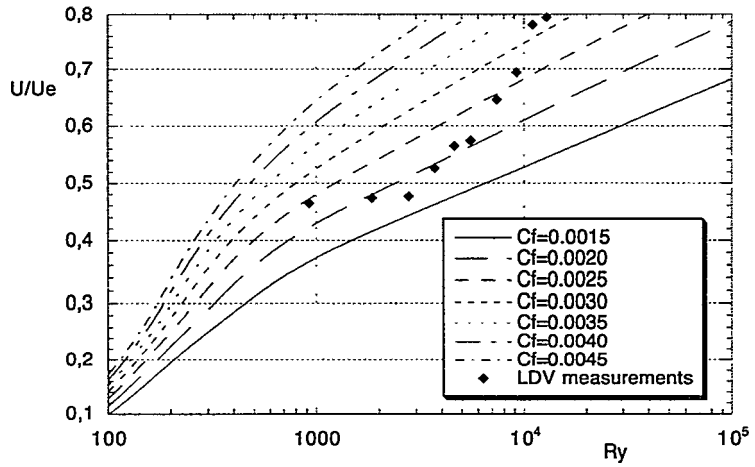

Figure 6.45: The clauser representation of the downstream corner for the rectangular shallow cavity.

downstream corner were investigated, no clear peak indicating the oscillations could be found.

Chapter 7

Mathematical Modeling

Along with the experimental investigation of the cavities, numerical simulations of the same cases were performed. The main intention of doing the numerical simulations was to check the agreement between the two approaches. If agreement was found the numerical simulations could give valuable additional information for the investigation of cavity flow influence on the ultrasonic flowmeters.

7.1 Mathematical Modeling in SPIDER

For the flow simulations, a inhouse-made program general-purpose computational fluid dynamics (CFD) called SPIDER was used. SPIDER was developed for calculating fluid flow in complex geometries. This program is based on the finite-volume concept and uses a non-orthogonal curvilinear computational mesh. There have been a number of publications based on SPIDER, e.g. (Melaaen 1990), (Melaaen 1992a),(Melaaen 1992b).

In the computations presented here, a Cartesian grid with 195×131 nodes is employed. The grid lines are concentrated in the vicinity of the cavity. In this region, the grid spacing is equidistant. Outside the cavity region, a constant expansion of 10 % is used. Since a Cartesian grid is employed, the 45° cavity walls are modeled using a staircase type blocking, resulting in a "saw-tooth" type profile. The standard high-Re k-ε model together with law-of-the-wall treatment has been used to account for the turbulence. A grid with as many as 387×387 was used to verify grid independence.

7.2 Comparison of results

In Fig. 7.1 and Fig. 7.2 the results from both measurements and numerical simulations are given for the sloping cavity pointing in the flow direction. As seen from the figures U show good agreement. There is some deviation inside the cavity. This might be from the

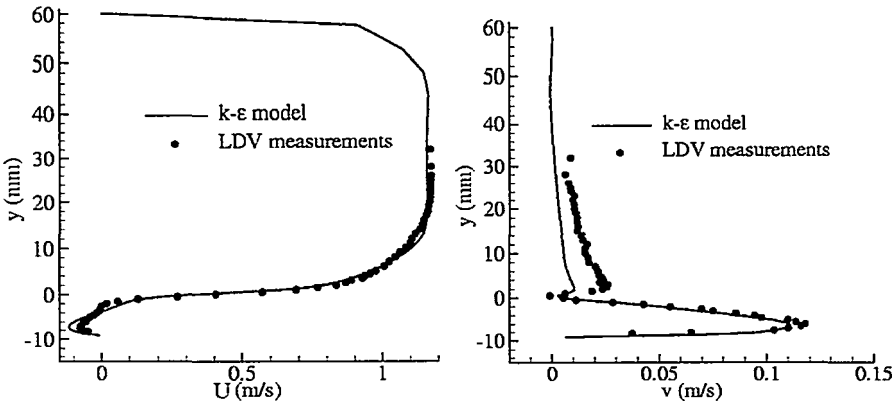

(a) U-mean at $0.25W$ before the downstream corner

(b) V-mean at $0.25W$ before the downstream corner

Figure 7.1: The mean velocity for sloping cavity in the flow direction

fact that it was difficult to find the exact position for the LDV measurement volume in the x-direction. This will lead to some differences, especially inside a vortex. An error of ± 0.3 mm can be expected in the x-direction for the measurements.

In Fig. 7.3 the comparison of some turbulent quantities at $0.25W$ are given. As seen from the figure also the turbulent quantities predicted from the numerical simulations show good agreement with the LDV measurements. The shear stress is not given because random sampling was used in the LDV measurements.

Figure 7.1(b) and Fig. 7.2(b) show the mean velocity in the y-direction, V. The figures show that there are some deviation outside the cavity between the measurements and the numerical simulations. Since this difference is systematic, the Probability Density Function, PDF, of the V mean velocity outside the boundary layer was calculated for the LDV measurements. This is shown in Fig. 7.5. As seen from the figure, the PDF has a gaussian shape with a large kurtosis or flatness factor, and nearly no skewness, as described by Tenekes and Lumley (1972). This means that the mean velocity in this case is the most common velocity measured. This was expected in the freestream if no disturbances were present in the flow. A difference as shown in the Fig. 7.1(b) and Fig. 7.2(b) will be present if the coordinate system of the LDV system do not match the cavity flow coordinate system. If the LDV probe was turned a few degrees, this would lead to an increase in the measured V velocity, and a decrease in U (as illustrated in Fig. 7.6). The difference in Fig. 7.1(b) and Fig. 7.2(b) will lead to a rotation of the coordinate system of $\gamma' = 0.4°$. This is a small angle, and will lead to nearly no change in U. The LDV probe was mounted with the traverse to the bar supporting the contraction as shown in Fig. 4.1 and Fig. 4.2. A

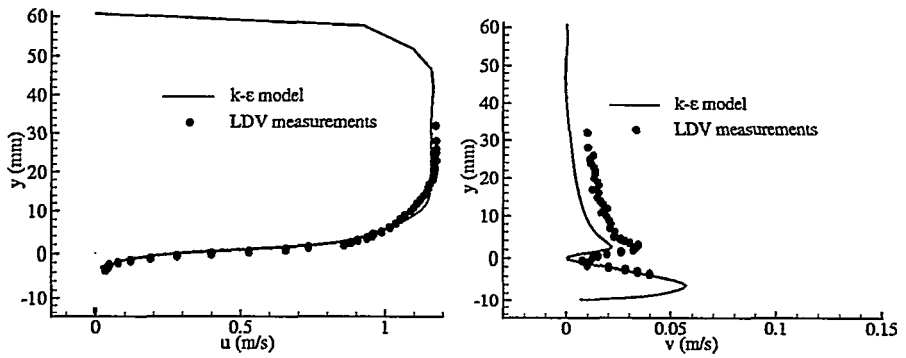

(a) U-mean at $0.14W$ before the downstream corner

(b) V-mean at $0.14W$ before the downstream corner

Figure 7.2: The mean velocity for sloping cavity in the flow direction

rotation between the coordinate systems of the test section and the LDV probe of $\gamma' = 0.4°$ is difficult to avoid.

Figure 7.4 shows that the agreement is good for the shallow rectangular cavity also. Ethembabaoglu (1973) found that the vortex in a shallow cavity moved towards the downstream wall (see chapter 2). Figure 5.6 and Fig. 5.7 show that this is true for the present study also. Figure 7.4 shows a comparison of results near the downstream wall. Figure 7.7 show a vector plot of the cavity flow calculated using k-ε. As seen, the centre of the vortex has moved towards the downstream wall, but the vortex is still covering the whole cavity. This is not in agreement with experiments. This effect will lead to good agreement near the downstream wall (as shown in Fig. 7.4), but not further upstream in the cavity. This is clearly seen if Fig. 7.7 is compared to the visualisations in Fig. 5.6 and Fig. 5.7.

7.3 Correction for the Ultrasonic Flowmeter

In chapter 7.2 we found that the agreement between measurements and numerical simulations is good. The numerical simulations were used to find cavity field mean velocities from parts of the cavities, both for the one pointing in the pipe flow direction and the one pointing countercurrent, as illustrated in Fig. 7.8 and Fig. 7.9.

The ultrasonic pulse is a concentrated beam (like water coming out of a fire hose, p.166 Kinsler and Frey 1962). This concentrated ultrasonic pulse will be influenced by the component of the pipe flow normal to the ultrasonic pulse and the one along the ultrasonic pulse. This influence will lead to a hysteresis in the ultrasonic path as illustrated in Fig. 7.10.

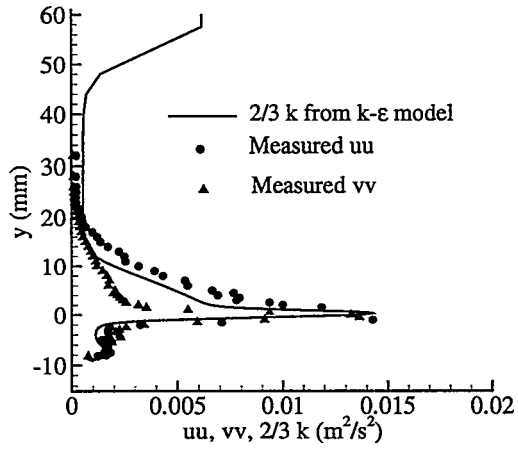

Figure 7.3: Some turbulent quantities at $0.25W$ for the sloping cavity pointing in the flow direction

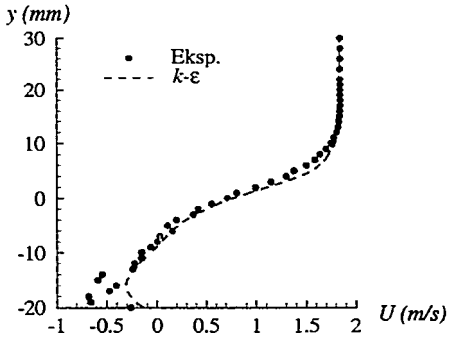

(a) U-mean at $0.57W$ before the downstream corner

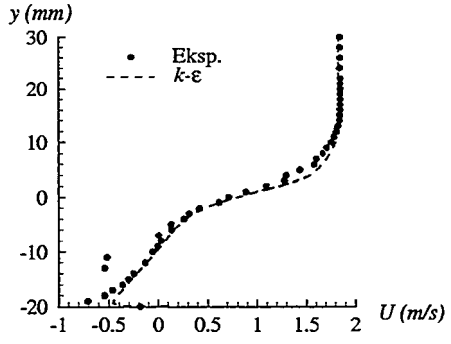

(b) U-mean at $0.75W$ before the downstream corner

Figure 7.4: The results for rectangular cavity

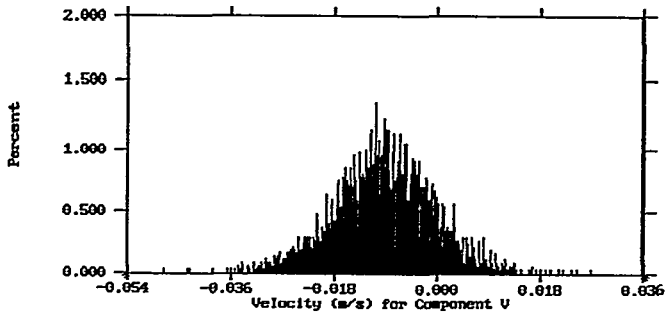

Figure 7.5: The PDF outside the boundary layer in the test section.

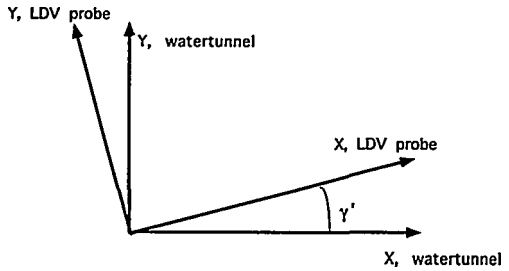

Figure 7.6: Illustration of difference in the coordinate systems

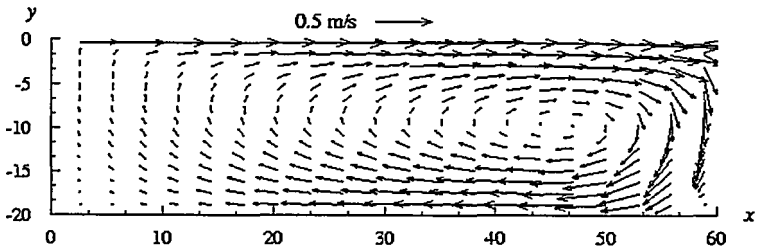

Figure 7.7: Rectangular cavity using k-ε, distance in mm

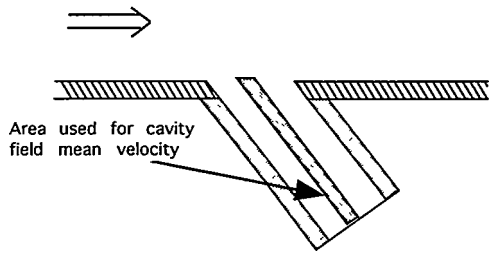

Figure 7.8: The area used to find the cavity field mean velocity for the cavity pointing in the pipe flow direction.

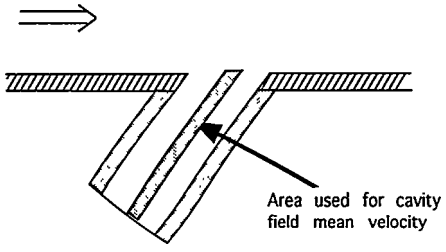

Figure 7.9: The area used to find the cavity field mean velocity for the cavity pointing countercurrent.

This means that it is possible to find relations between the pipe flow and the deflection of the ultrasonic pulse. The ultrasonic pulse will be influenced more and more as it travels through the pipe. For simplicity, only the angle found from Fig. 7.10 is used here. The figure shows the pipe flow vector, $\overline{V}_{\text{bulk}}$, and the ultrasonic path velocity vector, c_0. Also the deflection angle on the ultrasonic pulse is shown in the figure. The deflection will depend on whether the ultrasonic pulse travels in the flow direction or countercurrent. The relations for the deflections found from the present investigation are given in Eq. 7.1 and Eq. 7.2.

$$L_{\text{def},1} = \frac{\overline{V}_{\text{bulk}} \tan\overline{\beta_1}}{c_0 - \overline{V}_{\text{bulk}} \sin\overline{\beta_1}} D \tag{7.1}$$

$$L_{\text{def},2} = \frac{\overline{V}_{\text{bulk}} \tan\overline{\beta_2}}{c_0 + \overline{V}_{\text{bulk}} \sin\overline{\beta_2}} D \tag{7.2}$$

where $L_{\text{def},1}$ and $L_{\text{def},2}$ are illustrated in Fig. 7.11.

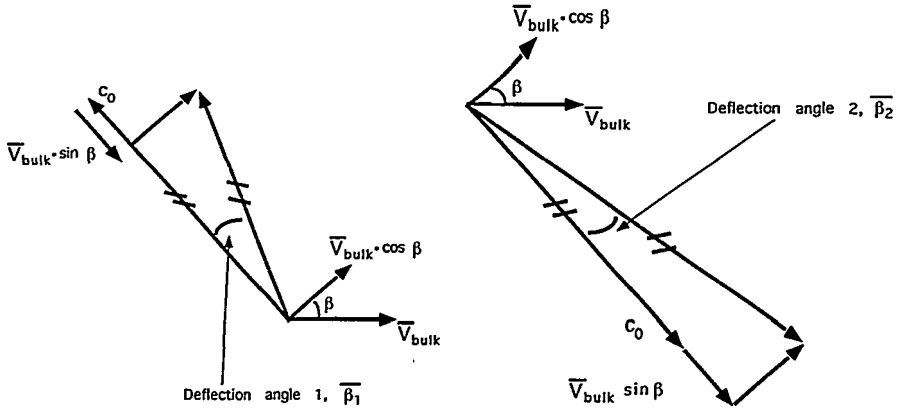

(a) The ultrasonic pulse traveling counter-current

(b) The ultrasonic pulse traveling in the pipe flow direction

Figure 7.10: The deflection angle found from the velocity vectors

It can be seen from Eq. 7.1 and Eq. 7.2 that the deflection depends on both the pipe flow and the diameter of the pipe.

As stated earlier, the ultrasonic pulse is a concentrated beam that will be deflected traveling through the pipe. It will go through several vortices inside the cavities (see Fig. 5.3 and Fig. 5.4) at different positions dependent upon the pipe flow rate. Since the peripheral velocity of a vortex increases going from the center of the vortex, the cavity velocity influencing the ultrasonic pulse increases as the pipe flow increases. This effect is illustrated in Fig. 7.11.

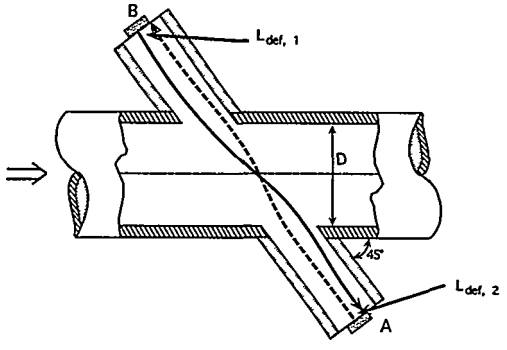

Figure 7.11: The deflection of ultrasonic pulses traveling between the sensors

From the present work it is shown that the vortex structure depends on the orientation of the cavity. This means that the effect of the cavities is different for the ultrasonic pulse traveling in the pipe flow direction than for the one traveling countercurrent.

In the present investigation it is assumed that the width of the ultrasonic pulse is 4 mm. This means that the area used to find the mean has a width of 4 mm. The mean area is moved as the pipe flow increases.

The positive direction is defined as out of the cavity pointing countercurrent and in to the one pointing in the pipe flow direction, as illustrated in Fig. 7.12. The figure also show that cavity A is the one pointing in the pipe flow direction, and cavity B is the one pointing countercurrent.

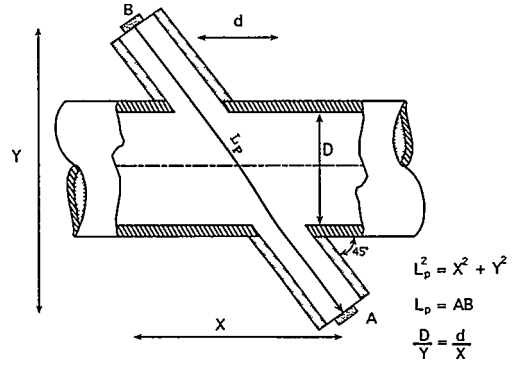

Figure 7.12: Geometric parameters for an ultrasonic flowmeter. The arrow on L_p gives the positive direction.

The numerical simulations show that the cavity field mean velocity, as illustrated in Fig. 7.8 and Fig. 7.9, have a linear dependency with the pipe flow. This is true for all the cavity field mean velocities influencing on the ultrasonic pulse. The results also show that there is a linear increase in the cavity field mean velocity from the cavity center line and outward to the cavity wall. The linearity is strongest for the cavity pointing in the pipe flow direction. Figure 5.3 show that there is a vortex covering almost the whole cavity width in the case of the cavity pointing in the pipe flow direction. For a steady pipe flow the cavity field mean velocity also increased linearly outward from the centre of the cavity. For the cavity pointing countercurrent there is a small vortex at the downstream corner, and a larger one further down in the cavity. Because of the difference in the vortex structure, the linear dependency between the cavity field mean velocity and the distance from the cavity centerline will have to be strongest for the cavity pointing in the pipe flow direction.

These findings were used to correct the formula given in the ISO/DTR 12765 "Measurement of fluid flow in closed conduits - Flow rate measurement by means of ultrasonic flowmeters". A correction was done to the integral for the velocity along the path. It takes into account both the size of the meter and the velocity inside the pipe.

The original equation defining the pipe flow is given as

$$\overline{V} = \frac{L_p^2}{2d}\frac{t_1 - t_2}{t_2 t_1} \tag{7.3}$$

where L_p is given by Fig. 7.12.

In this case the velocity is integrated along the path L_p with the assumption that there is no flow inside the cavity.

$$\int_0^Y v(y)dy = \overline{V}D \tag{7.4}$$

For detailed description of the ultrasonic flowmeters see ISO (1996) and AGA (1997).

The new formula with the correction suggested from these findings is given as

$$\overline{V} = \frac{L_p^2}{2d}\frac{t_1 - t_2}{t_2 t_1} + \frac{1}{4}\left(\overline{V}_{A_1} + \overline{V}_{B_1} + \overline{V}_{A_2} + \overline{V}_{B_2}\right)\left(\frac{x}{d} - 1\right) \tag{7.5}$$

(Løland et al. 1998) where $\overline{V}_{A_1}$ and $\overline{V}_{B_1}$ are the cavity field mean velocities that will influence on the ultrasonic pulse traveling countercurrent from cavity A to cavity B, as illustrated in Fig. 7.11. $\overline{V}_{A_2}$ and $\overline{V}_{B_2}$ are the cavity field mean velocities influencing on the ultrasonic pulse traveling in the pipe flow direction from cavity B to A.

In this case the integration was done along the path based on the findings from the measurements and numerical simulations of the flow inside the cavities. The integral becomes

$$\int_0^Y v(y)dy = D\left(\overline{V} + \left(\overline{V}_A + \overline{V}_B\right)\left(\frac{x}{2d} - \frac{1}{2}\right)\right) \tag{7.6}$$

By using the results from the numerical simulations of cavity velocities, the knowledge about the deflection of the ultrasonic pulse and the new integral given by Eq. 7.6, the influence from the cavity field means velocities was calculated as

$$\text{Relative deviation} = \frac{\frac{1}{4}\left(\overline{V}_{A_1} + \overline{V}_{B_1} + \overline{V}_{A_2} + \overline{V}_{B_2}\right)\left(\frac{x}{d} - 1\right)}{\overline{V}_{\text{bulk}}} \tag{7.7}$$

where $\overline{V}_{\text{bulk}}$ is the pipe flow from the numerical simulations in the two-dimensional pipe flow.

The result is given in Fig. 7.13.

As seen from the figure, there is a linear increase in the relative deviation as the pipe flow increases. A linear increase in the relative deviation means that the absolute deviation

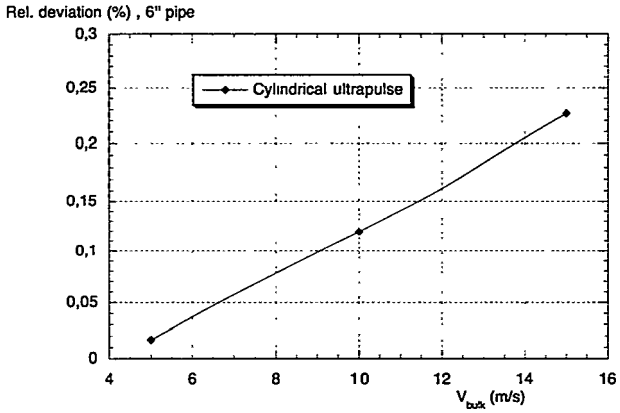

Figure 7.13: The relative deviation as a function of the pipe flow.

would have to increase as $O(\overline{V}_{\text{bulk}}{}^2)$. The investigation show that there is a linear dependency between the pipe flow and the cavity field mean velocities. A linear increase in the cavity field mean velocity outward from the centerline of the cavity is also found. These two effects together will lead to an absolute deviation increasing as $O(\overline{V}_{\text{bulk}}{}^2)$.

The results in Fig. 7.13 show the cavity flow influence on a thin ultrasonic pulse traveling in model cavities. The effect of changing the area used to find the cavity field mean velocity will influence on the observed effect. In reality the width of the beam might be 2 cm. A width of 4 mm as used in this case was used to illustrate the flow effect that a thin ultrasonic pulse would experience traveling through the pipe flow including the cavities.

In the present investigation two dimensional models were used. This was done to optimize the conditions for the experimental techniques applied. The effect of changing from two-dimensional cavities to real ultrasonic cavities has not been considered in the present work. Also the depth and angle of the cavities may influence. In this work the depth was set to 105 mm with an angle of 45°.

All these assumptions

- The area used for the cavity field mean velocity.
- Two dimensional instead of three dimensional cavities.
- Depth and angle of cavities.
- The divergence of the ultrasonic pulse

may influence on the effect on the ultrasonic pulse from the velocities inside the cavities.

The present work indicates that there is flow inside the cavities and that the effect of this flow may influence on the accuracy of the ultrasonic flowmeter.

Chapter 8

Conclusion

Results from an experimental investigation of flow in cavities has been reported. The experimental measuring techniques used are Laser Doppler Velocimetry, LDV, and particle Image Velocimetry", PIV. Also visualisations of the flow structure have been done using Laser Sheet flow Visualisations.

The PIV system used is an inhouse-made system based on cross correlation. Investigation of grid generated turbulence show that the PIV system can measure the flow with the same accuracy as the LDV system. The present work also show that by using cross correlation, the PIV system can be used to measure recirculating flow like the flow inside cavities.

All the three different experimental techniques show good agreement in the cavity flow. The flow structure inside the cavities depends upon the shape of the cavity. The flow direction over a sloping cavity also influences upon the flow structure inside the cavity. The present experimental results show good agreement with numerical simulations of the same type of geometry. For sloping cavities the k-ε model predict the flow structure well. For the shallow rectangular cavity, k-ε moves the vortex towards the downstream wall, but the vortex is still covering the whole cavity. Comparison with laser sheet flow visualisations show that the k-ε model sets up a large vortex that cover the whole cavity, and do not move it towards the downstream wall as seen from the visualisations.

The results from the present cavity flow investigation have been used to find the influence of the cavity velocities on a thin ultrapulse traveling between the two ultrasonic sensors. The present work shows that there will be a hysteresis in the ultrapulse path, dependent upon the pipe flow. There is a linear dependency between the cavity field mean velocity at different positions inside the cavity and the pipe flow. From the present study it is found that the relative deviation from the cavities have a linear dependency with the pipe flow. This means that the influence on the accuracy from the cavity velocities will be $O(\overline{V}^2_{bulk})$. The deviation also depends on the size of the meter. The reason for this is that the size of the cavities used to house the ultrasonic sensors are independent of the size of the pipeline.

It is clear from this investigation that the flow inside the cavities should not be neglected as done in the draft for the ISO technical report on ultrasonic flowmeters.

A further investigation of the influence of real cavities instead of the two dimensional models as used here is requested. The influence of the cavities upon the accuracy of the ultrasonic flowmeter here is based on the results found from the two dimensional model cavities and a thin ultrapulse. The effect of changing to real cavities, area used for cavity field mean velocity and the depth of the cavities will have to be further investigated.

The inhouse made PIV system has a 256×256 pixels CCD camera. This resolution narrows the measuring area to approximately 4 mm×4 mm. This area needs to be increased. With a larger measuring area the PIV system will be more flexible and able to measure whole flows like the cavity models used in this case.

Appendix A

The CCD camera

CCD cameras have become more and more common as the price for a CCD array has gone down. It is still expensive to buy a CCD camera with high resolution, but the price for a normal CCD array is now so low, that for many applications the CCD camera has replaced the normal film camera.

The CCD image sensor can be bought as a ready to use camera system or as a part of a digital integrated package, where the user has to supply the surrounding electronics. PIV-systems designers are usually no experts in the CCD technology, and apply commercial available camera systems. But still some knowledge about the design, operation and characteristics of CCD imaging devices is necessary for getting the best camera for the PIV-system.

CCD cameras can be divided in non-standard and standard cameras. The standard cameras are those who follow the standard video signals for public broadcasting systems, the CCIR (25 frames per second) in Europe and the NTSC (30 frames per second) in USA. The non-standard cameras are specially designed cameras, normally digital cameras, that do not follow either of these two standards.

For simplicity the charged coupled device, or CCD, can be illustrated by using glasses of water. The amount of charge can be illustrated as amount of of water inside the glass. The rain will fill up the glasses, and after a certain time the glasses are emptied, as illustrated in Fig. A.1.

If many water-glasses are used an array is set up.

Both for standard and non-standard cameras, the way the image sensor is organized is the same. There are two types of CCD arrays that are most common today. These are

- Inter line transfer, see Fig. A.2
- Full frame transfer, see Fig. A.3

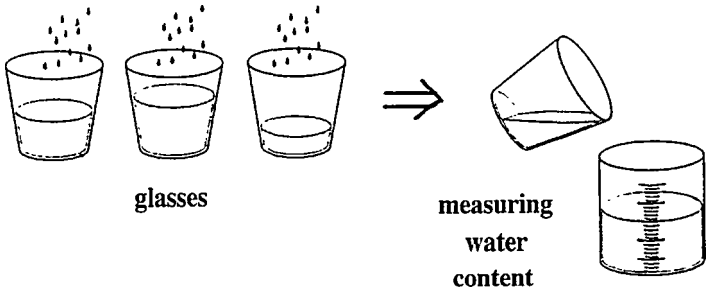

Figure A.1: Water glasses array and emptying, adapted from DALSA (1996)

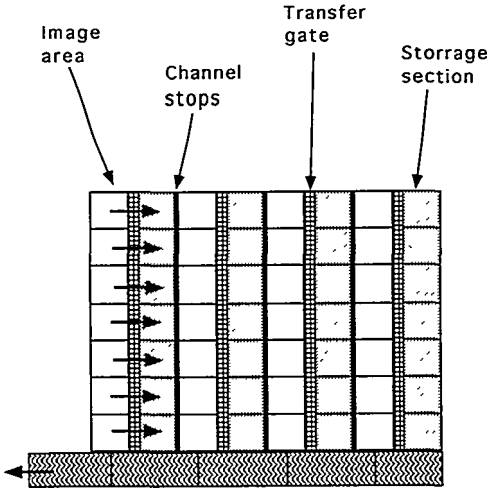

Figure A.2: The working principle of interline transfer CCD

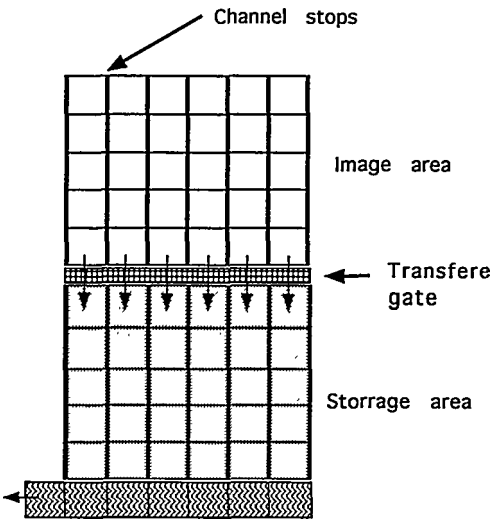

Figure A.3: The working principle of fullframe transfer CCD

The difference between these two types of sensors lies in the method for readout of the sensor, otherwise the working principle is the same. An array of lighted elements is separated by a transfer gate to the shiftregister. After a certain time the transfer gate opens and the electrons are forced to move into the shitfregister. In the shiftregister each element can be read out.

If a number of linear array sensors are combined to a two-dimensional array, an interline transfer CCD is produced. Line by line the output is then transferred to the final storage trough the sensor output (see Fig. A.2). By reading out even and odd rows alternately the interlaced mode of an interline transfer sensor is created.

A full frame transfer sensor is a sensor where the two-dimensional array is divided into two areas, an image area and a masked storage section. Both sections consist of parallel shift registers, separated by insulating walls (see Fig. A.3). After the image has been transferred to the storage region, line by line is read out by a shiftregister (see Fig. A.3).

Each of these two types of sensors have their own advantages. In full frame transfer the whole image is transferred at one time, and it has small separation between each pixel. It is therefore suitable for conditions where pulsed light is used, eg. PIV. The problem is that it is a slow process to read out a whole image compared to the interlaced interline transfer method. The interline sensor on the other hand is a fast sensor, when used in the interlaced mode. In the interlaced mode it will read out even and odd fields successively, and therefor only continuous light can bee used. In the non-interlaced mode only half the pixel resolution will be present in one of the directions, because even and odd pixels are read out as one pixel. The interline transfer type is the most commonly used and

inexpensive of the two types.

Some manufacturers make their CCD with large physical distance between each pixel. This is something that the user must take into account when selecting a camera.

Appendix B

Calculation of the correction

To be able to make use of the findings of this work. The formula used to find the velocity in ISO/DTR 12765 "Measurement of fluid flow in closed conduits - Flow rate measurement by means of ultrasonic flowmeters", needed to be recalculated adding the parameters for the flow inside the cavity.

Consider an ultra pulse leaving transducer A at an angle ϕ, (in Fig. 7.12 the angle $\phi = 45°$). The distance traveled in a time t in a fluid with velocity of sound c_0 we get in the y-direction

$$y = c_0 t_2 \sin\phi \tag{B.1}$$

and in the x-direction

$$x = c_0 t_2 \cos\phi + \int_0^Y \frac{v(y)}{c_0 \sin\phi} dy \tag{B.2}$$

The integral will be

$$\int_0^Y v(y)dy = D(\overline{V} + (\overline{V}_A + \overline{V}_B)(\frac{x}{2d} - \frac{1}{2}) \tag{B.3}$$

This will lead to

$$c_0 \cos\phi = \frac{x}{t_2} - \frac{d}{x}(\overline{V} + (\overline{V}_A + \overline{V}_B)(\frac{x}{2d} - \frac{1}{2})) \tag{B.4}$$

using $\cos^2\phi + \sin^2\phi = 1$ this will lead to

$$\frac{L_p}{t_2} = \sqrt{c_0^2 + \frac{d^2}{L_p^2}(\overline{V} + (\overline{V}_{A_2} + \overline{V}_{B_2})(\frac{x}{2d} - \frac{1}{2}))^2 - \frac{d^2}{x^2}(\overline{V} + (\overline{V}_{A_2} + \overline{V}_{B_2})(\frac{x}{2d} - \frac{1}{2}))^2} + \frac{d}{L_p}(\overline{V} + (\overline{V}_{A_2} + \overline{V}_{B_2})(\frac{x}{2d} - \frac{1}{2})) \tag{B.5}$$

If we consider a pulse traveling in the other direction with transit time t_1 the equation become

$$\frac{L_p}{t_1} = \sqrt{c_0^2 + \frac{d^2}{L_p^2}(\overline{V} + (\overline{V}_{A_1} + \overline{V}_{B_1})(\frac{x}{2d} - \frac{1}{2}))^2 - \frac{d^2}{x^2}(\overline{V} + (\overline{V}_{A_1} + \overline{V}_{B_1})(\frac{x}{2d} - \frac{1}{2}))^2} - \frac{d}{L_p}(\overline{V} + (\overline{V}_{A_1} + \overline{V}_{B_1})(\frac{x}{2d} - \frac{1}{2})) \tag{B.6}$$

We know that x. d and L_p are of the same order, and that $V << c_0$. This means that c_0^2 will be the dominant part under the square root sign in Eq. B.5 and Eq. B.6. The parts $\overline{V} + (\overline{V}_{A_i} + \overline{V}_{B_i})$ and $(\overline{V}_{A_i} + \overline{V}_{B_i})^2$ are therefor neglected.

If we then subtract Eq. B.6 from Eq. B.5 the result becomes

$$\frac{L_p}{t_2} - \frac{L_p}{t_1} = \frac{d}{L_p}(2\overline{V} + (\overline{V}_{A_1} + \overline{V}_{B_1} + \overline{V}_{A_2} + \overline{V}_{B_2})(\frac{x}{2d} - \frac{1}{2})) \tag{B.7}$$

This gives the equation for the velocity including the correction

$$\overline{V} = \frac{L_p^2}{2d}\frac{t_1 - t_2}{t_2 t_1} + \frac{1}{4}(\overline{V}_{A_1} + \overline{V}_{B_1} + \overline{V}_{A_2} + \overline{V}_{B_2})(\frac{x}{d} - 1) \tag{B.8}$$

As seen from the equation the correction depend on the size of the meter and the size of the cavities. Also the velocity inside the cavities, and the direction of the ultra pulse contribute to the correction.

Bibliography

Adrian, R. J. (1984). Scattering particle characteristics and their effect on pulsed laser measurements of fluid flow : speckle velocimetry vs. particle image velovimetry. *App. Opt. 23*, 1690.

Adrian, R. J. (1986). Image shifting technique to resolve directional ambiguity in double-pulsed velocimetry. *App. Opt. 25*, 3855.

Adrian, R. J. (1988). Statisical properities of particle image velocimetry measurements in turbulent flow. In *Laser Anemometry in Fluid Mech. 3*, Lisboan, pp. 115.

Adrian, R. J. (1991). Particle imaging technique for experimental fluid mechanics. *Annu. Rev. Fluid Mech. 23*, 261.

AGA (1997). Measurement of gas by ultrasonic meters. Technical report, American Gas Associaton, Arlington,Virginia. Report no.9, Draft 7.

Baher, H. (1992). *Analog and Digital Signal Processing.* Wiley.

Batchelor, G. K. (1953). *The Theory of Homogeneous Turbulence.* Cambridge University Press.

Bertuccioli, L., S. Gopalan, and J. Katz (1996). Image shifting for PIV using Birefringent and ferroelectric liquid crystals. *Exp. Fluids 21*, 341.

Bosio, J. and A. Erdal (1996). Gas metering technology - a strategic objective. In *IEA International Conference on Natural gas Transmission, Berlin, Germany.*

Carosone, F. and A. Cenedese (1996). Youngs fringes analysis by neural networks. In *Symp. Appl. Laser Tech. to Fluid Mech.*, Lisboan.

Collicott, S. J. and L. Hesselinh (1987). Real time speckle velocimetry with recording in potorefractive crystals. In *AIAA Pap. No. 87-1376.*

Dahlsveen, J. and S. A. Morud (1990). Eksperimentell undersøkelse av homogen og isotrop turbulens. Master's thesis, The Norwegian Institute of Technology. In Norwegian.

DALSA (1996). *Advancing Image Capture Technology.* DALSA INC.

Davis, M. R. (1980). Design of flat plate leading edge to avoid flow separation. *AIAA Journ. 18*, 598.

East, L. F. (1966). Aerodynamically induced resonance in rectangular cavities. *J. Sound and Vibrations 3*. 277.

Erdal. A. (1997). *Computational analysis of the flow field downstream of flow conditioners*. Dr. Ing. thesis. Norwegian University of Science and Technology.

Erm. L. P. and P. N. Joubert (1991). Low-reynolds-number turbulent boundary layer. *J. Fluid Mech. 230*. 1.

Ethembabaoglu. S. (1973, June). *On the Fluctuating Flow Characteristics in the Vicinity of Gate Slots*. Dr. Ing. thesis. Division of Hydraulic Engineering, Norwegian Institute of Technology.

Franke, M. E. and D. L. Carr (1975). Effect of geometry on open cavity flow-induced pressure oscillations. In *AIAA Aero-Acoustic Conference, Hampton, VA, Mar.24-26.*

Gonzalez. R. C. and R. E. Woods (1992). *Digital Image Processing*. Addison Westly.

Granwille. P. S. (1976). A modified law of the wake for turbulent shear layers. *J. of Fluids Engineering 98*. 578.

Hecht, E. and A. Zajac (1974). *Optics*. Addison Westly.

Hinze. J. O. (1975). *Turbulence*. McGraw-Hill.

ISO (1996). 10th working draft: Measurement of fluid flow in closed conduits - methods using transit time ultrasonic flowmeters. Technical report, International Organisation for Standariazation. ISO/DTR 12765 by ISO/TC 30/WG 20 N.

Kinsler. L. E. and A. R. Frey (1962). *Fundamentals of Acoustics* (2. ed.). John Willey and Sons. Inc.

Kompenhans. J., M. Raffel, and C. Willert (1996). Particle image velocimetry. In *Von Karman Lecture Ser. 1996-03*.

Koseff. J. R. and R. L. Street (1984, March). Visualisation studies of a shear driven three-dimensional recirculating flow. *J. of Fluid Engineering 106*, 21.

Landreth. C. C. and R. J. Adrian (1988). Electrooptical image shifting for particle image velocimetry. *Appl. Opt. 27*, 4216.

Landreth. C. C., R. J. Adrian, and C. S. Yao (1988). Electrooptical image shifting for particle image velocimetry. *Exp. Fluids 6*, 119.

Løland. T., L. R. Sætran, R. Olsen, I. R. Gran, and R. Sakariassen (1998). Cavity flow correction for the ultrasonic flowmeter. In *Proceedings from FLOMEKO'98, Lund, Sweden*. Presented at FLOMEKO'98, June 15-17.

Løland. T., L. R. Sætran, and R. Sakariassen (1998). Experimental investigation using piv and laser sheet visualisation in cavity flows. In *Proceedings from 8th International Symposium on Flow Visualisation, Sorrento, Italy*. Presented at 8isfv, September 1-4.

Lourenco. L. (1993). Velocity bias technique for particle image velocimetry measurements of high-speed flows. *APPLIED OPTICS 32*, 2159.

Lourenco, L. (1996). Particle image velocimetry. In *Von Karman Lecture Ser. 1996-03.*

Lourenco, L. and A. Krotapalli (1987). The role of photographical parameters in laser speckle or particle image displacement velocimetry. *Exp. Fluids 5*, 29.

Melaaen, M. C. (1990). *Analysis of Curvilinear Non-orthogonal Coordinates for Numerical Calculation of Fluid Flow in Complex Geometries.* Dr. Ing. thesis, University in Trondheim.

Melaaen, M. C. (1992a). Calculation of Fluid Flows with Staggered and Nonstaggered Curvilinear Nonorthogonal Grids–The Theory. *Numerical Heat Transfer, Part B 21*, 1–19.

Melaaen, M. C. (1992b). Calculation of Fluid Flows with Staggered and Nonstaggered Curvilinear Nonorthogonal Grids–A Comparison. *Numerical Heat Transfer, Part B 21*, 21–39.

Musker, A. J. (1979). Explicit experssion for the smooth wall velocity distribution in a turbulent boundary layer. *AIAA Journ. 215*, 639.

O-Hern, T. J., J. R. Torczynski, T. K. Blanchat, T. Y. Chu, and A. L. Tassin (1994). Shear-driven flow in a square cavity: A comparative study using piv, ldv and computational simulations. In *Procedings of the 1994 ASME Engineering Division Summer meeting, Part 13(18), Lake Tahoe, NV, USA.*

Rockwell, D. and C. Knisely (1979). The organized nature of flow impingment on a corner. *J. of Fluid Mechanics 93*, 413.

Rockwell, D. and E. Naudascher (1978). Review - self-sustaining oscillations of flow past cavities. *J. of Fluid Engineering 100*, 152.

Roshko, A. (1955, August). Some measurements of flow in a rectangular cutout. Technical report, National Advisory Committee for Aeronautics, n.3488.

Sætran, L. R. (1984). *Experimental investigation and mathematical modelling of momentum, heat and mass transport in some turbulent flows.* Dr. Ing. thesis, Norwegian Institute of Technology.

Sakariassen, R. (1996). Real life experience with multipath ultrasonic gas flow meters. In *Inrenational pipeline conference - Vol. 2*, pp. 1077.

Sarohia, V. (1977, July). Experimental investigation of oscillations in flow over shallow cavities. *AIAA Jour. 15*, 984.

Schlichting, H. (1968). *Boundary Layer Theory.* McGraw Hill.

Skåre, P. E. (1994). *Experimental investigation of an equlibrium boundary layer in adverce pressure gradient.* Dr. Ing. thesis, The Norwegian Institute of Technology.

Takai, N. and T. Asakura (1983). Displacement measurement of speckles using a 2d level crossing technique. *Appl. Optics 22*, 3514.

Tenekes, H. and J. Lumley (1972). *A first course in turbulence.* The MIT Press.

Townsend. A. A. (1956). *The Structure of Turbulent Shear Flow.* Cambridge University Press.

TSI (1993. Mach). *Find Information Display (FIND) Software, Version 4.0, revision C.* TSI Corp. part nr.1990585.

van Bloemendaal. K. and P. M. A. van der Kam (1995). Installation effects on multi-path Ultrasonic flow meters: The "Ultraflow" project. In *3rd Int. Symp. of Flow Measurement, San Antonio.*

van Driest, E. R. (1956). On turbulent flow near a wall. *J. Aeronautical Sciences 23.* 1007.

Vogt. A.. F. Reichel. and J. Kompenhans (1994). A compact and simple all optical evaluation metode for piv recordings. In *7. Int. Symp. on App. of laser tech. to fluid Mech..* Lisboan.

Westerweel. J. (1993). *Digital Particle Image Velocimetry - Theory and Application.* Ph. D. thesis. Delft University.

White. F. M. (1991). *Viscous Fluid Flow.* McGraw-Hill.

Wolley. J. P. and K. Karamcheti (1973, February). A study of narrow band noise generation by flow over ventilated walls in transonic wind tunnels. Technical report, Nielsen Engineering and Research, Inc.(NEAR) TR 50.

Wormell. D. C. and J. Sopchak (1993). Particle image velocity system using a high resolution ccd-camera. In *Opt.Diag.in Fluid and Thermal flow ed. SS cha, J.D.Trollinger Proc. SPIE.* pp. 648.